2014

The identification and characterization of electronic defect bands in organic photovoltaic devices

John A. Carr
Iowa State University

The identification and characterization of electronic defect bands in organic photovoltaic devices

by

John Anthony Carr

A dissertation submitted to the graduate faculty in

partial fulfillment of the requirements for the degree of

DOCTOR OF PHILOSOPHY

Major: Electrical Engineering

Program of Study Committee
Sumit Chaudhary, Major professor
Vikram Dalal
Jaeyoun Kim
Malika Jefferies-El
Santosh Pandey

Iowa State University

Ames, Iowa

2014

To my lovely wife: thank you for your unconditional support.

TABLE OF CONTENTS

Acknowledgements

First and foremost, I would like to extend great thanks to my major professor – Dr. Sumit Chaudhary. Your guidance, encouragement and patience have been greatly appreciated and will not be forgotten. I would also like to thank the other members of my committee, Dr. Vikram Dalal, Dr. Jaeyoun Kim, Dr. Malika Jeffries-El and Dr. Santosh Pandey, for their continued guidance through this research. In addition, a special thanks goes to my friends and lab-mates – your help has made all this possible. Lastly, I would like to say thank you to my family. You have always encouraged me and I would not be here today if it were not for you.

ABSTRACT

In any microelectronic device, fundamental physical parameters must be well understood if electronic properties are to be successfully optimized. One such prominent parameter is energetic trap states, which are well-known to plague amorphous or otherwise impure semiconducting materials. Organic semiconductors are no strangers to such states and their electronic properties are evidently tied to these defects. This dissertation aims to elucidate these states in organic photovoltaic (OPV) devices. The literature to date is first reviewed and the author's contributions are subsequently detailed.

Within the community, several techniques have been leveraged to study these mid-gap states. Atop the list are optical, capacitance and current based measurements and each has provided important pieces to the overall defect profile. Piecing together the works to date, organic photovoltaic materials are depicted as disordered semiconductors with a seemingly continuous distribution of both energetically shallow and deep trap bands. Upon blending the pure materials to create the modern day bulk heterojunction – the currently preferred photovoltaic architecture – energetic disorder increases and new trap bands appear. These states have been shown to stem from both intrinsic (e.g. structural disorder) and extrinsic (e.g. oxygen and synthesis contaminates) sources and it is quite clear that such states can have profound effects on, if not completely control, the electronic properties and long term stability of OPV devices. Most prominently, these states are known to enhance trap-assisted recombination, induce Fermi-level pinning and generate space-charge effects. Though these

mid-gap traps have a large negative impact, they also can give an advantageous inherent doping, improving conductivity and interfacial electric fields. Evidently, continued progress in understanding the nature, sources, affects and possible mitigation of these defects in both current and future materials will be crucial to the optimization of this promising technology.

The primary work of this study is to build upon these reports and to further the current body of knowledge on the identification and characterization of defect states in OPV devices. Capacitance techniques are heavily employed herein. As such, the accurate capacitance characterization of OPV devices was first visited. It was found that, owing to thinner films and larger series resistance, the series based parasitics could not be neglected in the typical frequency range of interest or significant errors and misinterpretations were introduced. Armed with this more accurate model, deeper, previously unknown trap states were then identified using low frequency capacitance measurements coupled with a point by point differential of high frequency capacitance-voltage measurements. The discovered defects remain important as it is those states closer to the midgap which more efficiently contribute to recombination and can be detrimental to device performance. More generally, the presented technique gives a generic overview of the capacitance response of OPV devices – resolving anomalies and enabling others to better study the defect profile in their devices. Lastly, the pre-exponential factor of trap emission, also known as the attempt-to-escape frequency, was characterized. This parameter is essential if trap occupancy kinetics are to be accurately described – important for any measurement or model dependent on the detrapping dynamics. It was found that the polymer based devices studied herein have a prefactor within a similar range, yielding similar

trap capture cross sections. Not only does this give guidance as to the proper value to be used in the detrapping measurements/models, but also indicates that the trapping mechanisms in these devices are likely similar.

1 CHAPTER I: INTRODUCTION

The last decades have witnessed a shift in the world views of the energy sources which sustain our industries, homes and transportation. To date, the fossil fuels have been staple power generators; however, many have begun to question the impact of burning resources such as coal and oil on both human and environmental health. This, coupled with pushes to achieve energy independence with long-term sustainable sources, has spurred extensive research into alternative energies. The most promising, low-carbon sources include nuclear, wind, geothermal and solar – each with distinct advantages. Though a likely solution to the energy needs consists of a diverse combination of the above, this review focuses on specifics of the latter: solar power. Photovoltaic devices have become popular for many applications owing to their relative small scale (e.g. can be incorporated into many products), independence from large infrastructure (e.g. suitable for off-grid locations) and decentralization (e.g. the energy source does not need to be transported).

Today, the terms 'solar cell' and 'solar panel' typically refer to commercially available arrays based on inorganic materials such as silicon or cadmium telluride. However, within the research community, organic materials have emerged as strong candidates for the next generation of devices. These materials offer numerous advantages, including thin film thickness, lights weights, mechanical flexibilities, a relative ease of processing and a lower environmental impact (e.g. low energy payback time and low levels of anthropogenic emissions)[1]. Most notable are the latter two. Low-temperature, solution based fabrication opens the door for large scale roll-to-roll production. This has the potential to greatly reduce commercial

manufacturing costs, enabling a wider scale of affordability and distribution with less environmental impact than the more traditional photovoltaic technologies. Of course, in order to become more commercially feasible, organic photovoltaic (OPV) cells must first be efficient, stable and reproducible solar converters.

OPV research has been ongoing for many years. Numerous important breakthroughs have gated today's progress and the last decade in particular has seen a rapid improvement in OPV performance. The first OPV devices consisted of a single-layer organic semiconductor sandwiched between two electrodes. Photons incident on the organic material were absorbed, which, owing to a low dielectric constant and small Bohr radius of carriers, generate a bound electron-hole pair.[2] Within the bulk, the electric field was insufficient for exciton dissociation, thus the power conversion efficiency (PCE) was severely limited as most photogenerated charges were lost to recombination. In response, Tang demonstrated a bilayer structure comprising a planar stack between an organic donor and acceptor.[3] This p-n heterojunction-like device produced a large dissociation field at the material junction and gave a PCE of nearly 1%.[3] However, with the typical exciton diffusion length (*ca.* 10 nm) an order of magnitude smaller than the thickness required for high optical absorption (*ca.* 100+ nm), many excitons were unable to reach the separation interface and were still lost. Thus, Halls *et al.* and Yu *et al.* then introduced the bulk heterjunction (BHJ) concept; a blended film comprised of a bulk mixture between donor and acceptor materials.[4,5] This bulk blend generates dissociation interfaces at a phase segregation nearing the exciton diffusion length, while still allowing for sufficient optical

thickness. The structure pushed single junction PCEs to several percent, a number which in recent days is approaching 10%.[6]

Though the field has impressively progressed over the last several years, the Schockley-Queisser PCE limit of a single junction BHJ OPV has been calculated at *ca.* 23%.[7] This highlights that extensive bottlenecks still exist. Energy level misalignment, inadequate light trapping, poor exciton diffusion, recombination and low carrier mobilities have been cited as the top deficiencies limiting device perforamce.[7] Through the efforts to alleviate these bottlenecks, many of the latest breakthroughs have come from the development of new materials. Each with improved bandgaps and tuned energy level offsets to improve absorption, open circuit voltage, charge dissociation and the like. However, no matter the material, fundamental physical parameters will remain important, and understanding their role in OPV performance is crucial in further optimizing this promising technology. One such underlying physical aspect is the presence of defects and the mid-gap energy states they create.

2 CHAPTER II: BACKGROUND AND LITERATURE SURVEY

In this chapter, a discussion on the background of defect states in organic photovoltaic devices is presented. Works to date centered on such defects are detailed and the basic concepts of commonplace defect measurements are described. The literature review below was published in *Energy and Environmental Science* in 2013.[8]

2.1 Defects: Background, definition of terms, etc.

When speaking of organic semiconductors, the highest occupied molecular orbital (HOMO) and lowest unoccupied molecular orbital (LUMO) are commonly referenced. These orbitals are often likened to the valence and conduction bands of inorganic materials and, similarly, are separated by a bandgap. Within this energy gap, it is well known that both shallow- and deep-level states can be present (**Figure 1**), painting a picture of energetic disorder in OPV materials. Generally speaking, the origins of these trap states are described by two broad categories: extrinsic and intrinsic.[9] Extrinsic traps stem from extrinsic defects, such as chemical impurities introduced during material synthesis, device fabrication or exposure to oxygen or moisture.[9-17] External bias-stress and an electrochemical process involving oxygen and electrical biasing have also been shown to generate metastable mid-gap states – which are extrinsic by nature.[18,19] Extrinsic, chemical defects can be further described as either bound or unbound, differentiating impurities that are chemically appended from those that are not.[20] Intrinsic traps stem from intrinsic defects. These defects arise from the morphological disorder inherent in the amorphous nature of a typical organic film.[2,21-24] Morphological defects can be described as

either noncovalent or covalent.[2] The former refers to energetic entities which slightly perturb surrounding energy levels, generating states [typically] shallower in the bandgap.[25] Owing to their weak effects, no covalent bonds are altered. This type of disorder is common in molecular organic semiconductors.[2] In contrast, the latter refers to defects which cause higher energy perturbations, affecting covalent bonds and generating levels [typically] deeper in the gap.[26] This type of disorder is common in π-conjugated organic semiconductors.[2,26] Of course, not all defects will lead to electroactive mid-gap states. Some may yield energy states within the carrier bands themselves,[23] and are of less interest to the review at hand. Yet, it is those imperfections which produce bandgap residing states, both shallow and deep, that are of great importance to OPV device physics and performance.

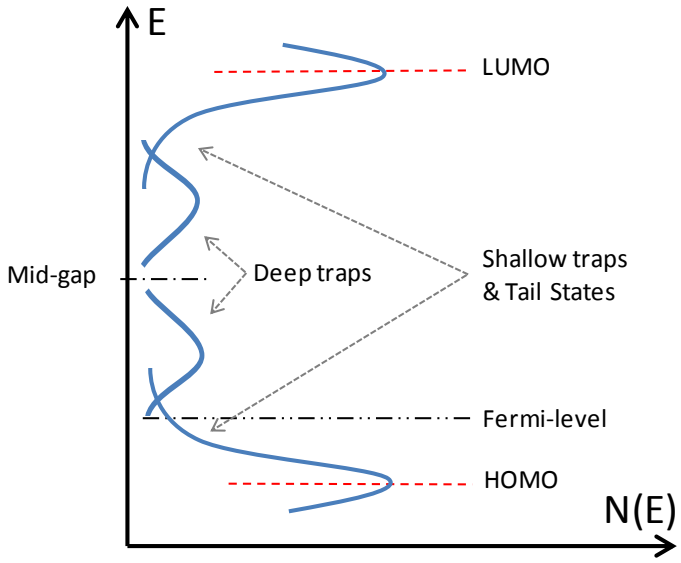

Figure 1: simplified model conceptually illustrating the density of states in an organic material.

It is well known that such defects can have profound effects on physical operation in inorganic devices.[27-29] Thus, it comes with no surprise that similar effects on OPV performance should be expected, significantly contributing to the abovementioned deficiencies. It has even been said that defects completely control the electronic properties of amorphous and polycrystalline organic materials,[26] truly highlighting the need for an in-depth understanding of these states. Defects are known to introduce recombination centers, charged point sites or both. If present in appreciable concentrations, recombination centers can contribute to free carrier loss through trap-assisted recombination, especially if the trap is spatially located at or near a donor-acceptor interface.[30-32] Charged defects are known to greatly affect the electrostatic potential throughout the device,[9] which can be detrimental to carrier mobility and inhibit transport,[20,26] as well as retard the probability of charge separation and promote the likelihood bimolecular recombination.[33] Further, bulk charges have been linked to the quenching of photogenerated excitons, indicating the presence of charged defects may strongly limit the diffusion length of this important quasiparticle.[20,26] Energetic trap sites can also pin the Fermi-level deep within the bandgap, greatly suppressing the built-in field.[34] In a solar cell device, each of these can yield losses in short circuit current density (J_{sc}), open circuit voltage (V_{oc}) and/or fill factor (FF); hindering the overall PCE. Further, the enhancement of inherent traps or the creation of new bands during device operation (e.g. through light or oxygen exposure), largely affects OPV stability and may greatly contribute to the long-term degradation of these devices.[35,36] On the other hand, some aspects of these unintentional defects states may be beneficial to OPV performance.

As such, this has inspired Wang *et al.* to ask "Do the defects make it work?".[25] The typical organic semiconductor employed in OPV devices has a bandgap nearing 2 eV. This strongly limits the intrinsic carrier concentration to $1x10^3$ – $1x10^7$ cm^{-3}.[2,26] However, the actual carrier density can be substantially higher. For example, common π-conjugated polymers have a concentration reaching $1x10^{15}$ – $1x10^{19}$ cm^{-3}, some 8 to 16 orders of magnitude higher than the estimated intrinsic density.[25,37-40] These extra carriers originate from both structural and extrinsic defects which produce electronic states near a band edge.[2] Oxygen and moisture, in particular, have been identified as sources of *p*-type doping, especially if the exposure is in the presence of light.[10,11,14,41-47] Controlled doping has proven to be an important parameter for inorganic devices and, albeit typically unintentional, these defects may be just as advantageous for OPVs. Most notably, these excess concentrations may vastly alter carrier conductivity as well as the electric field at the donor-acceptor interface,[2,10,25,26,48-50] improving charge transport and exciton dissociation while lowering recombination probability at the interface. Of course, as the dopant carrier moves into the more delocalized states, it leaves behind a localized site of opposite charge, unavoidably generating a coulomb trap. As stated above, such charged states can have profound effects on electrical properties, and thereby, a tradeoff is formed.[10,49]

Nonetheless, good or bad, defect states in plastic solar cells must be well understood. Thus, their identification, characterization and potential mitigation or enhancement remain important areas of research. The first, *identification*, represents the need to profile the complete trap density of states (tDOS) throughout the bandgap of OPV materials. As is typical in amorphous thin-films, multiple trap bands may exist – highlighting the importance of rigorous

profiling techniques to ensure all prominent bands are well known. The second, *characterization*, is the determination of the physical characteristics of these trap bands and their affect(s), whether it be positive or negative, on solar cell performance. Among many characteristics, one might be interested in the energetic location, concentration, disorder spreading, spatial location, type of carrier (majority or minority) trapped and capture/emission coefficients. The last, *mitigation* or *enhancement*, refers to an end goal of reducing defects states that negatively influence OPV performance while augmenting states that have a positive effect. Though it will be impossible to completely rid OPV materials of detrimental defects, reducing trap states by even an order of magnitude[31] and gaining better control of the impurity based doping will be highly beneficial to performance.

As a step towards realizing this goal, this chapter presents a review of select studies centered on defects in OPV devices. Our intention is to highlight the progression of trap band identification, characterization and mitigation to date and give a general view of its current state. Trap profiling in neat materials will first be examined, followed by that in blended systems. Trap effects on OPV performance as well as thoughts on trap origins can found throughout. In an effort to give a general understanding as to the employed measurements, their introductory concepts, equations and relevant citations are also provided.

A note on nomenclature: relatively shallow impurities are routinely introduced into inorganic materials to manipulate free-carrier concentrations. In such a case, these states are referred to as donors (i.e. readily donate an electron to the conduction band to dope *n*-type) or

acceptors (i.e. readily accept an electron from the valence band to dope *p*-type).[51] Herein, this nomenclature is adopted to describe the extrinsic behavior of OPV materials. N_A will refer to those relatively shallow levels, which give an apparent *p*-doping. Similarly, relatively deep impurities can be considered either donor-like (trap-neutral when electron filled and positively charged when empty) or acceptor-like (trap-neutral when hole filled and negatively charged when empty).[51] Herein, this nomenclature is adopted and such deep trap levels are marked N_T.

2.2 Identification and characterization: neat material systems

2.2.1 General Depiction

As a starting point, let us look at photothermal deflection spectra (PDS) from Goris *et al.* to understand wavelength dependent absorption, and thereby, the general depiction of the midgap tDOS in common OPV materials.[52] The spectra of neat poly(3-hexylthiophene) (P3HT), neat poly(p-phenylene vinylene (PPV), neat [6,6]-phenyl-C61-butyric acid methyl ester ($PC_{60}BM$) and blends thereof are shown in **Figure 2**. For the time being, I will concentrate on the neat materials, but later revisit the blend spectra. The three materials listed are extensively studied *model* OPV systems and will be heavily concentrated on in this article. The PDS spectra shown in Figure 2 establish the generally accepted picture of the molecular orbitals and energetic DOS. Weak absorption at lower energies, a rapid increase at moderate energies and relatively strong absorption at higher energies is seen. This is in accordance with molecular orbitals that are Gaussian in nature, broadening of which introduces a distribution of shallow defects that trail into more localized states deeper in the gap. Turning to other works, some substantiation of this picture can be found.

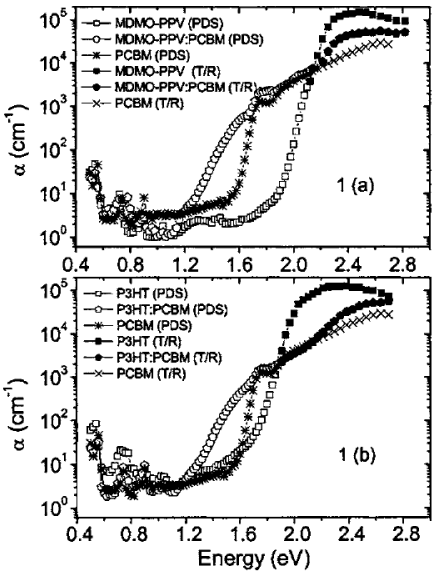

Figure 2: (a) PDS-spectrum of dropcast layers of MDMO-PPV (square), PCBM (star) and MDMO-PPV:PCBM (80 wt%) (pentagon). (b) PDS-spectra of dropcast layers of P3HT (square), PCBM (star) and P3HT:PCBM (66.66 wt%) (pentagon). The full symbols (PCBM=star) correspond to data obtained with transmittance and reflectance measurements. Reprinted with permission from [52]. Copyright [2006], American Institute of Physics.

In acceptor materials, this general depiction is readily substantiated by earlier optical experiments on C_{60} and C_{70} fullerites.[53,54] Again, distinct absorption in the sub-gap regime was observed and identified as an Urbach tail (shallow states) leading into localized electronic levels (deeper states). In donor materials, a more thorough substantiating view can be offered through thermally stimulated current (TSC) measurements (refer to section 2.5.1 for details).[55] In the cited work, an indium tin oxide (ITO)/P3HT/Aluminum (Al) structure was studied.[55] As shown in **Figure 3**, the resulting TSC profile identifies two prominent peaks in the energetic

tDOS. The first, low temperature peak (93 K) represents relatively shallow levels, likely tail states extending from the Gaussian orbital. The second, high temperature peak (200 K) represents deeper states, likely more localized trap levels. This illustrates a tDOS much like that of Figure 1 and is in support of the PDS data.

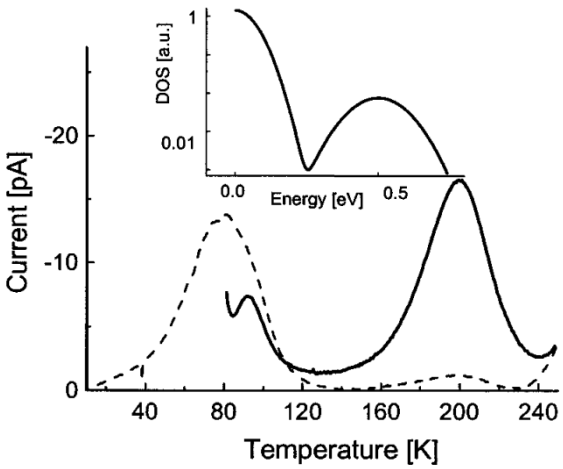

Figure 3: TSC signal from a thin film of P3HT sandwiched between an ITO and aluminum electrode for the case of temperature of trap filling 77 K (solid line) and 4 K (dashed line). Inset shows the energy dependencies of the DOS. Reprinted with permission from [55]. Copyright [2003], American Institute of Physics.

Clearly, the general depiction shows a distribution of bangap residing states in both pure donor and pure acceptor materials. In the subsequent subsections, I will further detail and quantify these shallow and deep trap states and highlight their origins.

2.2.2 Levels in donor materials

2.2.2.1 Relatively shallow activation energies

To begin the more detailed discussion, I focus first on shallow traps in neat donor materials. The low temperature TSC peak above was confirmed and further resolved in 2008.[56] Here, ITO / poly(3,4-ethylenedioxythiophene) poly(styrenesulfonate) (PEDOT:PSS) / P3HT / Al devices were studied.[56] A low temperature peak around 85 K (105 meV) with a shoulder around 50 K (50 meV) was found (**Figure 4a**, black line). The 85 K peak is in good agreement with the prior TSC work (93 K), however, the aforementioned 200 K peak was not reproduced.[56] A similar finding was also noted through drive-level transient spectroscopy (DLTS; refer to section 2.5.6 for details), where a single trap level with an activation energy of *ca.* 87 meV was revealed but, again, no deeper band was seen.[57] Interestingly, Schafferhan's shallower 'shoulder band' was also not noted in the DLTS work. In any case, Schafferhans *et al.* estimate the total trap density in the studied energy regime to be *ca.* 1.0×10^{16} cm^{-3}.[56] To further quantify and construct a resolved profile of the tDOS (**Figure 4b**), the authors then applied the so-called fractional T_{start}-T_{stop} TSC technique (Figure 4a, colored lines; refer to section 2.5.2 for details). Clearly seen in the resolved factional data is the overlap of two Gaussian-like distributions, indicating two prominent bands in a continuous distribution of relatively shallow trap states.

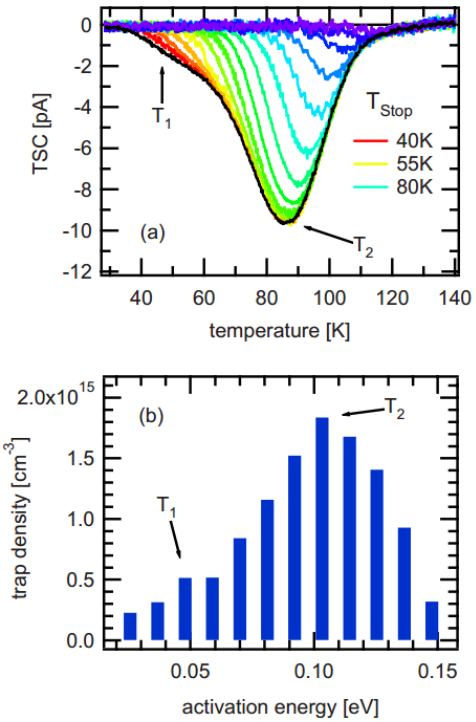

Figure 4: (a) main runs of the different Tstart - Tstop cycles, as well as the conventional TSC spectrum (black curve), revealing two trap states T1 and T2 and (b) the resulting DOOS distribution. Reprinted with full permission from [56]. Copyright [2008], American Institute of Physics.

Shallow activation levels in unblended donors have also been directly observed through capacitance versus voltage (CV) measurements (refer to section 2.5.4 for details).[14] It should be noted that the CV measurement is sensitive only to mobile charges. Herein, complete ionization is not assumed and this CV measured quantity is referred to as the 'ionized acceptor density' (N_A^-). This value should be considered, at the least, a lower limit of the total shallow impurity concentration. As mentioned above, defects tend to give OPV materials an apparent *p*-type doping. With moderate dopings, Fermi-levels are in the range of a few hundred meV above the

HOMO. This, coupled with cathode work functions that are several hundred meV lower, promotes the formation of a Schottky barrier at the organic-cathode junction.[58] The existence of such an interface in neat P3HT diodes was evidently shown by Dennler *et al.*, and thereby, the authors demonstrated the ability to leverage depletion capacitance techniques on these systems to study bandgap residing states. In Dennler's work, the charge carrier density as per air exposure was monitored through CV measurements (**Figure 5**).[14] The group found the ionized acceptor density evolved from 5.0×10^{16} to 1.0×10^{17} cm^{-3} throughout the exposure experiment.[14] The as-cast density is in the same range as that predicted by the TSC measurements,[56] again showing a strong presence of shallow levels. The evolution of the concentration through air exposure supports the claim that oxygen and moisture give rise to a *p*-type doping and will be revisited later.

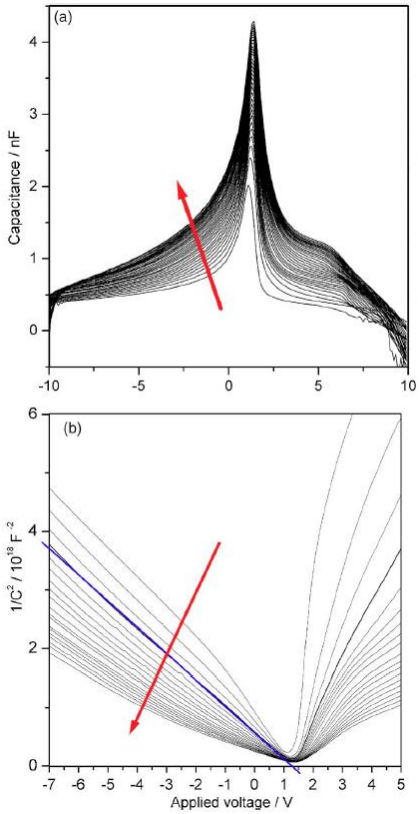

Figure 5: (a) capacitance C and (b) $1/C^2$ of an ITO/P3HT/Al diode recorded at 1 kHz every 2 min in air versus the applied voltage V. The arrows indicate increasing time. The solid line in (b) is a linear fit of one intermediate curve. Reprinted with full permission from [14]. Copyright [2005], American Institute Physics.

Other CV works can be explored for comparison. One such work was recently provided by Li. *et al.*[59] The group studied CV characteristics at various frequencies on a ITO/PEDOT:PSS/P3HT/Al structure. An ionized impurity concentrations in the range of 6 to $10x10^{14}$ cm^{-3} was found,[59] significantly lower than that of Dennler *et al.*[14] Though the exact reason for this large difference is unknown, I suspect several likely contributors. Simply, variations in air exposure could cause this noted difference. However, one must also remember

structural imperfections as well as other chemical impurities can contribute to the shallow level concencetration.[2] When comparing the fabrication of each group's devices, a film thickness of *ca.* 1 µm for Dennler and *ca.* 5 µm for Li is found.[14,59] Thicker films dry more slowly and slower drying is known to reduce structural disorder.[60] Thereby the apparent *p*-type doping may be reduced. This gives a good introduction to the effects that simple processing parameters can have on energetic defect states.

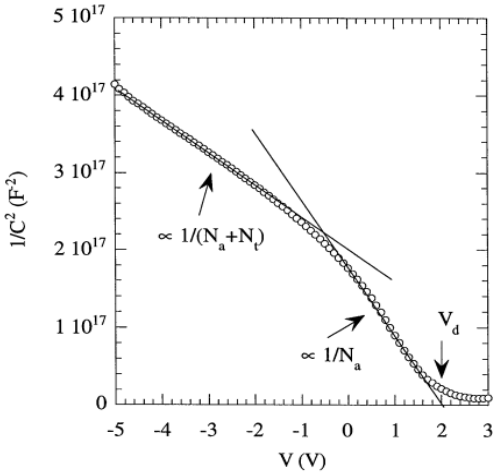

Figure 6: inverse capacitance squared, $1/C^2$, against applied bias, V_{appl}, of an ITO/PPV/Al device. Reprinted from publication [61], Copyright [2000], with permission from Elsevier.

CV measurements have also been used to identify shallow states in PPV based diodes (**Figure 6**) – an ITO/PPV/Al structure was studied.[61] The measurements were taken between -5 and 3 V_{DC}; the employed frequency is not known.[61] A quantification for N_A^- was not given, but can be estimated in the range of $5x10^{16}$ cm^{-3} if a nominal device area is assumed. This is in line with typically reported values.

Clearly, shallow states in neat donors are present. Fractional TSC measurements show these states to be distributed in energy, while CV indicates these states [at least partially] ionized to give rise to an appreciable amount of mobile charges. Moving forward, I wish to elucidate the states deeper in energy. Such states are subtly seen in Figure 6.

Upon further examination of Figure 6, one notes a break in the Mott-Schottky (MS) slope at *ca.* -0.75 V_{DC}. In fact, Dennler *et al.* as well as Li *et al.* also observed this dual slope. In the former (Figure 5), the authors imputed the break to an inhomogeneous doping profile induced by the fabrication process.[14] This is a reasonable attitude considering a spatial change (increase) in N_A^- would induce such a slope change. Li *et al.*, however, have indicated this may be the result of a non-uniform spatial doping *or* may represent the presence of energetically deep trap band(s).[59] The latter highlights a second, important interpretation, which has a basis in deep-trap-rich materials.[62] The formalization of such an interpretation was given by Kimerling and is summarized in section 2.5.4.[63] Campbell *et al.* have taken this interpretation and asserted the break stems from deep trap contributions. This gives the indication that levels with a relatively deeper activation energy are present, which, because of the prominent decrease in the MS slope, are acceptor-like such that $N_T > N_A^-$.[61] This interpretation is in line with the general 'shallow + deep trap' depiction of section 2.2.1, giving some corroboration to the authors' theory. The next section aims to focus on these deep states in donor materials.

2.2.2.2 Relatively deep activation energies

The presence of these deeper trap levels was further substantiated and quantified by DLTS measurements in the same work.[61] Campbell *et al.*'s measurement showed the presence of deep, *p*-type majority bulk-traps that are distributed in energy.[61] Through temperature dependent measurements and extensive model fitting, the authors deduced a discrete trap level with an activation energy of *ca.* 750 meV above the HOMO and a concentration of *ca.* $5x10^{17}$ cm^{-3}. This readily supports the notion from the CV data that a large concentration of states is present deeper in the mid-gap of pure PPV films.

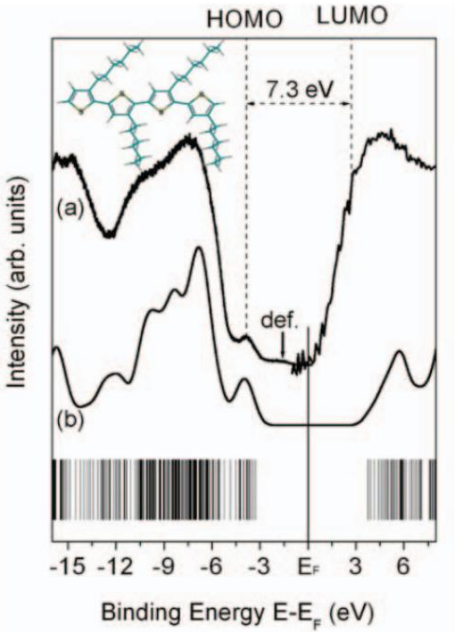

Figure 7: occupied (left) and unoccupied (right) molecular orbital contributions of regioregular P3HT to the (a) photoemission and inverse photoemission spectra, respectively, are compared with (b) theory. The experimental HOMO-LUMO gap of P3HT (7.3 eV) is indicated as is a defect state (def.) not directly attributable to the molecular orbitals indicated (see text). The inset

shows a schematic of a single chain of regioregular P3HT. Reprinted with full permission from [64]. Copyright [2007], John Wiley and Sons.

Indeed, a similar deep defect band in pure P3HT was predicted, not only by the TSC measurements above (Figure 3), but also by ultraviolet and inverse photoemission spectroscopy.[64] The photoemission spectra of **Figure 7** show a weak feature (labeled 'def') that cannot be associated with either molecular orbital.[64] This distribution occurs within the polymer bandgap and likely represents deep states. To gain further insights and quantification of the suspected band, I turn to capacitance versus frequency (CF) measurements (refer to section 2.5.5 for details).[38] Such measurements have directly revealed a Gaussian shaped deep trap band in neat P3HT diodes with E_T=390 meV above the HOMO, σ_T=56 meV and N_T=2.1x10^{16} cm^{-3}.[38] One notes these parameters are somewhat different than those derived for PPV diodes but, nonetheless, illustrate a similar qualitative depiction. CV measurements included with the cited CF experiment yield an ionized acceptor density of 3.2x10^{16} cm^{-3},[38] in line with that of Dennler's CV measured 5x10^{16} cm^{-3} for neat P3HT diodes.[14] Interestingly, if one considers the lower measurement frequency employed in Dennler's CV work (1 kHz) as well as the CF theory outlined in section 2.5.5, the known deep trap may be fully responding throughout the CV measurement. If the deep-band concentration (2.1x10^{16} cm^{-3})[38] is subtracted from the measured N_A^- (5x10^{16} cm^{-3}),[14] a *real* ionized acceptor concentration of 2.9x10^{16} cm^{-3} is revealed. This is in excellent agreement with the aforementioned 3.2x10^{16} cm^{-3} and gives nice substantiation of the applied theory. Moreover, this highlights that $N_T \approx N_A^-$, indicating a

substantial impact of N_T on the electronic properties, and thereby, photovoltaic performance should be expected.

As such, modeling techniques employing similar trap distributions should properly describe the current characteristics of these OPV systems. In general, charge transport in a typical organic material is described by a hopping behavior. These current characteristics are usually explained with space-charge limited (SCL) and trap limited (TL) models. From this modeling, features of the dominate trap sites and their effects on charge transport can be readily studied (refer to section 2.5.3 for details). Nikitenko *et al.* have done just that with neat P3HT diodes.[55] In accordance with their TSC data (Figure 3), a multiple trap formalism was employed with the assumption that a superposition of two Gaussian distributions makes up the energetic DOS.[55]

$$g(E) = \sqrt{\frac{2}{\pi}}\frac{(N - N_T)}{\sigma}\exp\left(-\frac{E^2}{2\sigma^2}\right) + \frac{N_T}{\sqrt{2\pi}\sigma_T}\exp\left(-\frac{(E - E_T)^2}{2\sigma_T^2}\right) \quad \textbf{(1)}$$

Numerical calculations coupled with this dual Gaussian were presented to study the model's general behavior. As expected, the simulations showed high voltages or a zero trap concentration induced currents close to the trap-free law (Equation (13) with θ=1), while variations of the N_T, E_T and σ_T parameters showed slope changes and voltages shifts in the

current characteristics at intermittent biases.[55] Confident in its validity, the model was then applied to P3HT diode currents.[55] The experimental data was well explained by the defined model and the parameters summarized in **Table 1**.[55] As seen, this data supports the depicted shallow-deep tDOS and further quantifies their deep-trap band concentration at $1.5x10^{16}$ cm^{-3}. The trap density (N_T) as well as spreading parameter (σ_T) are in good agreement with the CF based work – though, the activation energy is somewhat higher. Nonetheless, this highlights these trap states have a controlling effect on charge transport.

	E (meV)	N (cm^{-3})	σ (meV)
Shallow band	-	$1.0x10^{18}$	55
Deep band	500	$1.5x10^{16}$	80

Table 1: summary of important fitting parameters in Nikitenko *et al.*'s dual Gaussian SCL current work.

Evidently, deeper distributions are present in neat donor materials. In both P3HT and PPV these deep traps have been identified and characterized. In P3HT a Gaussian distribution has been indicated, while in PPV a dominant discrete level. In both, a relatively high density of traps has been reported – $\geq 1x10^{16}$ cm^{-3} – which is of the same order and, in some cases, even greater than the density of relatively shallow states. Of course, thus far I have focused only on trap levels between the HOMO and mid-gap of these neat materials, however, traps in the upper half of the gap must also be considered.

2.2.3 Electron traps

The discussion on electron traps in donor materials is relatively straight forward as a recent work by Nicolai *et al.* unifies the presence of these deep states in popular OPV materials.[65] The authors leveraged a numerical drift-diffusion model coupled with a Gaussian distribution of states to study the current characteristics of electron-only organic diodes. Remarkably, the electron trap band was found to be fairly consistent with $E_T \approx -3.6$ eV below the vacuum level, $N_T \approx 3x10^{17}$ cm^{-3} and $\sigma_T \approx 100$ meV for all tested materials.[65] In P3HT, for example, this corresponds to a trap depth of *ca.* 600 meV below the LUMO. One also notes the relatively high density of defects states. Thereby, piecing together the works discussed insofar to depict the complete trap profile between donor HOMO and LUMO, the cartoon of Figure 1 is readily obtained – that is, Gaussian shaped molecular orbitals that decay into distributions of energetically shallow and deep trap states.

Interestingly, Nicolai *et al.'s* work implies that materials with an electron affinity approaching or larger than *ca.* -3.6 eV should exhibit trap-free electronic properties. Indeed, this was found true for both $PC_{60}BM$ (LUMO ≈ -3.9 eV) and poly[{*N*,*N'*-bis(2-octyldodecyl)-naphthalene-1,4,5,8-bis(dicarboximide)-2,6-diyl}-*alt*-5,5'-(2,2'-bithiophene)] (P(NDI2OD-T2); LUMO ≈ -4.0 eV), both of which gave trap-free SCL electron transport.[65] Of particular interest is the former, which is a commonly used acceptor in today's OPV cells. Having established a more detailed view of the electronic traps in neat donor materials, I now turn my attention to the other half of the BHJ blend: acceptor materials.

2.2.4 Levels in acceptor materials

As discussed above, most modern day OPV devices comprise both donor and acceptor materials. Neat donors have been discussed thus far; let us now visit the latter. Methanofullerenes are commonly employed acceptors and may contain bandgap residing trap states. Though $PC_{60}BM$ was shown to exhibit trap-free electron transport,[65] others have indicated electron trapping in acceptor materials, especially the higher adduct fullerenes.[66] As an example of directly identifying such states, I highlight a work in which the conventional and T_{start}-T_{stop} TSC measurements were again applied.[67] Bis[6,6]-phenyl-C61-butyric acid methyl ester ($bisPC_{61}BM$), [6,6]-phenyl-C71-butyric acid methyl ester ($PC_{71}BM$), and $PC_{61}BM$ based devices (ITO/PEDOT:PSS/PCBM/ Lithium Fluoride (LiF) /Al) were studied. **Figure 8** shows the resulting [conventional TSC] spectra, whose quantification is summarized by **Table 2**.[67]

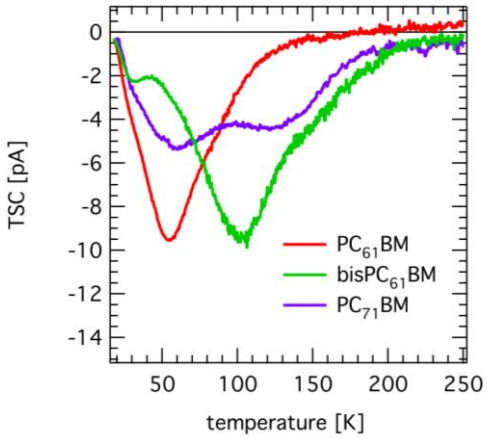

Figure 8: TSC spectra of $PC_{61}BM$, $bisPC_{61}BM$ and $PC_{71}BM$. Reprinted with full permission from [67]. Copyright [2011], John Wiley and Sons.

Sample	Trap Density (m^{-3})	T_{max} (K)	E_t (meV)
$PC_{61}BM$	≥ $1.7x10^{22}$	54.9	86
$bisPC_{61}BM$	≥ $2.3x10^{22}$	32.4	45
		103	184
$PC_{71}BM$	≥ $2.0x10^{22}$	60.1	96
		121.4	223

Table 2: lower limit of the trap densities of $PC_{61}BM$, $bisPC_{61}BM$ and $PC_{71}BM$, as well as the temperatures of the TSC maxima and the corresponding activation energies estimated by the T_{max} method according to Equation (4). For $bisPC_{61}BM$ and $PC_{71}BM$ E_t and T_{max} values of both peaks are shown. Reprinted with full permission from [67]. Copyright [2011], John Wiley and Sons.

Interestingly, all three materials showed at least one distinct trap distribution, with $bisPC_{61}BM$ and $PC_{71}BM$ showing the presence of a second, deeper level. Each methanofullerene exhibited a markedly different TSC spectrum. A common feature was noted between $PC_{61}BM$ and $bisPC_{61}BM$, where a low temperature peak in $bisPC_{61}BM$ (*ca.* 32 K or 45 meV) closely matched a slight $PC_{61}BM$ TSC shoulder (Figure 8) – signifying a common defect level.[67] To give some substantiation, DLTS measurements on neat $PC_{61}BM$ films (ITO/PEDOT:PSS/$PC_{61}BM$/LiF/Al) also showed a single shallow trap band in this range, however, with a somewhat lower activation energy (21 meV).[57] At first sight this shallow $PC_{61}BM$ level seems to be in contrast to the trap-free electron transport discussed earlier.[65] However, this can be reconciled by considering the trap band magnitude. It is well know that for a Gaussian distribution of *shallow* traps, the space charge limited current is approximated by a modified

Mott-Gurney law (see Equation (13)). A quadratic current-voltage relationship coupled with a reduced [effective] mobility is then exhibited. The effective mobility is given by $\mu_p\theta$ and,

$$\theta = \frac{\langle n_c \rangle}{\langle n_c \rangle + \langle n_t \rangle} \quad \textbf{(2)}$$

where $\langle n_c \rangle$ is the average free carrier concentration throughout the thickness and $\langle n_t \rangle$ the average trapped charge. As previously stated, the trap-free case has θ=1. The free carrier concentration in $PC_{61}BM$ is in the range of $1x10^{18}$ cm^{-3} and, for a conservative estimate, consider the trapped charge to be in the range $1\text{-}2x10^{16}$ cm^{-3}. This gives a θ approaching 1 and indicates trap-free electron transport should be expected. Nonetheless, the TSC of all three materials indicated a continuous distribution of trap states throughout the measured energy regime. This point is confirmed by fractional TSC measurements on $PC_{61}BM$, which further quantified the tDOS.[67] When comparing these three commonly employed materials, both $bisPC_{61}BM$ and $PC_{71}BM$ showed further broadening in the TSC signal and slightly higher trap concentrations with significantly deeper energies.[67] This indicates a higher amount of energetic disorder and electron trapping in these two derivatives and explains lowered dark currents through these materials.[67]

This TSC work supports the general depiction of the neat acceptor tDOS (section 2.2.1) and further quantifies the states present in common acceptors. Clearly, the pure acceptor materials of OPV devices are subject to energetic disorder and bandgap residing trap levels. The impact of

these states on photovoltaic performance will be discussed later. Next, trap origins in these neat materials are visited.

2.2.5 Trap origins: Oxygen, structural and synthesis residuals

To give some idea as to the sources of the trap levels discussed above, this section explores studies centered on defect level origins in neat OPV materials. Both extrinsic and intrinsic sources are considered, namely: oxygen/moisture, structural disorder and synthesis residuals.

As mentioned throughout the chapter and hinted at by the aforementioned CV work,[14] oxygen and moisture have been identified as key sources of *p*-type doping in donor materials. This indicates these extrinsic impurities generate or alter bandgap residing levels of interest. To begin this discussion, I return to the P3HT TSC work presented by Schafferhans *et al*. (Figure 4).[56] In the report, the conventional TSC measurement was repeated as a function of both air and pure oxygen exposure. After 96 hrs of O_2 treatment, the magnitude of the 105 meV band nearly tripled, while the 50 meV remained unchanged.[56] Similar effects were noted for air exposure. This shows that the shallower, 50 meV band is likely intrinsic (structural) in nature. Though, other chemical impurities cannot yet be ruled out. More notably, this shows the dominate 105 meV band is likely extrinsic in nature and heavily related to oxygen. Interestingly, photo-charge extraction by linearly increasing voltage (photo-CELIV) measurements show that after 100 hrs of air exposure, the mobility dropped by nearly 50x. Clearly, oxygen plays a role in generating

or, at the least, altering some portion of the shallow trap distribution in neat P3HT, and thereby, the electronic properties.

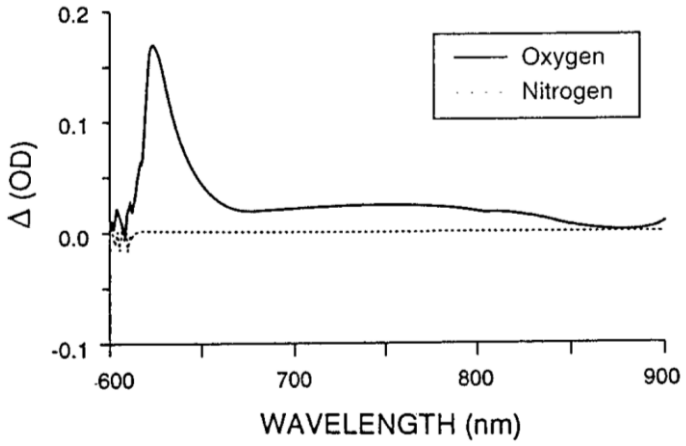

Figure 9: UV-vis absorption spectra of a P3HT thin film (20 µm) in contact with oxygen (10 atm) and under oxygen-free N2. Reference, O2-free film. Reprinted with permission from [10]. Copyright [1997], American Chemical Society.

An earlier work on the interaction of oxygen with poly(3-alkylthiophenes) helps to further explain this oxygen related defect and the noted effects on carrier mobility.[10] Abdou *et al.* theorized a charge transfer complex (CTC) would form between oxygen and the polymer, with a lowest binding energy on the order of *ca.* 1.9 eV.[10] Further, it was thought that this CTC state might facilitate charge transfer and the formation of excess charge carriers, thereby affecting electronic properties. To detect this possible band, the group studied UV-vis absorption of P3HT films in the presence of oxygen and nitrogen (**Figure 9**). As can be seen, nitrogen had essentially no effect on the measured optical density. In contrast, oxygen induced

significant changes, especially near *ca.* 630 nm or 1.97 eV – strongly implicating the predicted CTC.[10] This complex formation is supported by the later work of Aguirre *et al.*, who have also extended this concept to another polymer.[47] Though the most substantial change in optical density occurred near 630 nm, it is clearly seen that oxygen induces changes throughout the sub-gap energies (Figure 9). This introduces the idea that oxygen in itself affects and/or generates a continuous distribution of levels throughout the bandgap. Such a thought is also supported by a recent UV-vis study on P3HT in solution form (**Figure 10**).[68] Here, a broad sub-gap absorption band about *ca.* 810 nm was induced by oxidant treatments of molecular oxygen (O_2) as well as Nitrosonium tetrafluoroborate ($NOBF_4$). Interestingly, the absorbance for wavelengths between *ca.* 300 and 550nm was noticeably reduced. A similar decrease at moderate wavelengths coupled with an increase at longer wavelengths was also noted for treated polymer films, though not nearly as pronouced.[68] Intuitively, one might expect the noted changes to have effects on the electronic properties of these films.

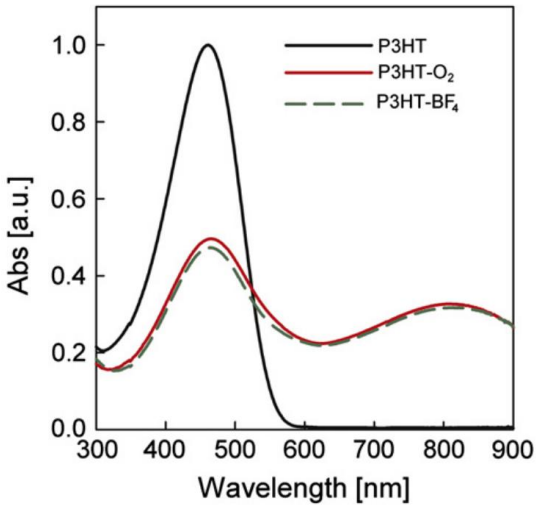

Figure 10: comparison of UV-vis spectra of P3HT in o-dichlorobenzene solution with the spectra of the P3HT solution after exposure to molecular oxygen ($P3HT^{+}$-O_2^{-}) and $NOBF_4$ ($P3HT$-BF_4^{-}). Reprinted from publication [68], Copyright [2012], with permission from Elsevier.

To detect such changes, Abdou *et al.* measured the effects of oxygen pressure on both the conductivity and mobility of P3HT based field-effect transistors. In the presence of increasing oxygen pressure, conductivity was found to increase, while mobility was found to decrease.[10] An analogous case is well known for inorganic semiconductors with increasing doping concentrations.[51] This strongly indicates oxygen facilitates the presence of extra carriers and helps explain the degraded mobility noted by Schafferhans *et al.* during the exposure experiments.[56] The presence of these oxygen induce charge carriers has been more directly observed in the afore-discussed work of Dennler *et al.* (Figure 5).[14] As mentioned, through successive CV measurements in open air, the group found the ionized acceptor density increased by a half order of magnitude ($5.0x10^{16}$ to $1.0x10^{17}$ cm^{-3}).[14] This gives a quantification

to Abdou *et al.*'s carrier concentration increase and further highlights the strong effect of oxygen/moisture on the shallow impurity states.

In like fashion, the electron traps noted by Nicolai *et al.* were also imputed [at least in part] to oxygen. As discussed, the electron-trap parameters between numerous materials were found to be similar. This indicates a common origin and rules out structural disorder. Through quantum-chemical calculations, the authors track down this origin and suspect hydrated oxygen complexes as the likely culprit.[65] Evidently, oxygen and moisture play a dominate role in the complete bandgap tDOS of acceptor materials.

Like donor materials, air and oxygen exposure have also been shown to have significant effects on the energetic tDOS of C_{60} and C_{70} films. In the case of C_{60}, exposure was found to greatly enhance the PDS spectrum of the deeper, localized states, while leaving the shallow-tail largely unaltered.[53] TSC experiments on C_{60} based transistors adds to this, pin-pointing a trap band center on *ca.* 230 meV that was greatly affected by exposure and an even deeper band centered on *ca.* 370 to 420 meV which remained unchanged.[16] This again depicts a defect distribution in which some bands are dominated by structural disorder, while others are heavily influenced by oxygen and/or moisture. Of course, other extrinsic chemical impurities from material synthesis or device fabrication may contribute to the overall tDOS and are incidentally lumped in with the structural disorder here. As is the case with the donor materials, these oxygen induced modifications in C_{60} are also accompanied by a significant decrease in carrier mobility.[16,69,70] Contrarily, in the case of C_{70}, the sub-gap absorption coefficient was actually

found to decrease with oxygen exposure, hinting that O_2 may be beneficial in terminating some inherent defects.[54] Interestingly, oxidant treatments (O_2 and $NOBF_4$) of PCBM in solution form did not produce any changes in the optical density.[68]

Defect origins from residuals left during material synthesis must also be considered. Though reports linking the contaminant impurities to specific trap-band energies could not be found, it is well-known that these synthesis residuals produce electronic-property altering states. Mentions to contaminates from starting reagents, nickel, copper and rhodium catalysts, etc. can be found.[71,72] However, maybe most prominent in the literature is residual palladium. A majority of conjugated polymers are synthesized *via* Stille or Suzuki coupling reactions – which are catalyzed by palladium complexes.[72,73] Residuals of this transition metal have been reported and linked to a degradation of electronic properties and photovoltaic performance.[71-74] In the case of PPV, residual palladium nanoparticles were found to induce shorts, greatly lowering the resistance of the film.[71] Even very small, hard to detect amounts (e.g. <0.1% by weight) of contaminate can have an effect on material properties and OPV performance.[71-73] The effects of residual catalysts on OPV performance will be subsequently discussed.

Nonetheless, it is evident that commonly used, pure donor and acceptor OPV materials are trap-rich semiconductors with electronic properties closely tied to their intrinsic and extrinsic induced defects. A depiction of energetic disorder with multiple defect levels both shallow and deep has been given and elucidations as to the origins of these traps has been presented. I now move to a discussion on how this defect profile changes in the popular BHJ OPV structure;

comprising bulk blends of the donor and acceptor materials discussed above. The sources of these defects will be revisited and the effects of these defects of BHJ photovoltaic conversion will be examined.

2.3 Identification and characterization: blended material systems

2.3.1 General depiction

Having examined neat films, it is a logical step to now look at the tDOS of the blended systems which make up modern day OPVs. First, the PDS data of Goris *et al.* should be revisted.[52] As seen in Figure 2, when compared to neat materials, the spectra of blended devices showed a more intricate distribution which extended deeper into the gap.[52] This strongly indicates a higher degree of disorder in both PPV:PCBM and P3HT:PCBM BHJ devices. This story of stronger disorder was recently corroborated and further resolved by Neugebauer *et al.*, who have leveraged DLTS measurements to compare the trap bands of neat P3HT and PCBM to that of blended films.[57] The activation energies and relative trap concentrations are shown in **Figure 11**. As can be seen, a comparison to TSC measurements on neat P3HT,[56] neat PCBM[67] and a blend thereof[36] has also been included. One recalls that the neat-film DLTS data has been already mentioned and both materials showed a single, dominate trap level with an activation energy of 21 meV for PCBM and 87 meV for P3HT.[57] The DLTS of blended films, however, presented with numerous emission spectra, indicating multiple trap-levels throughout the tDOS. At the low end of the energy spectrum, a trap 'A' with an activation near 28 meV was found. This corresponds reasonably well to the DLTS measured trap in neat $PC_{60}BM$ (21 meV), indicating its contribution to blend tDOS.[57] The most concentrated band 'E' has an

activation energy of *ca.* 100 meV and correlates well the TSC (105 meV) measured neat P3HT trap,[56,57] potentially indicating the polymer's contribution. The other bands, 'B-D' and 'F', are unique to the blended system. This readily supports the general depiction of greater energetic disorder upon mixing the neat materials and highlights the presence of more charge traps in these BHJ devices. Let us now further detail and quantify this added disorder.

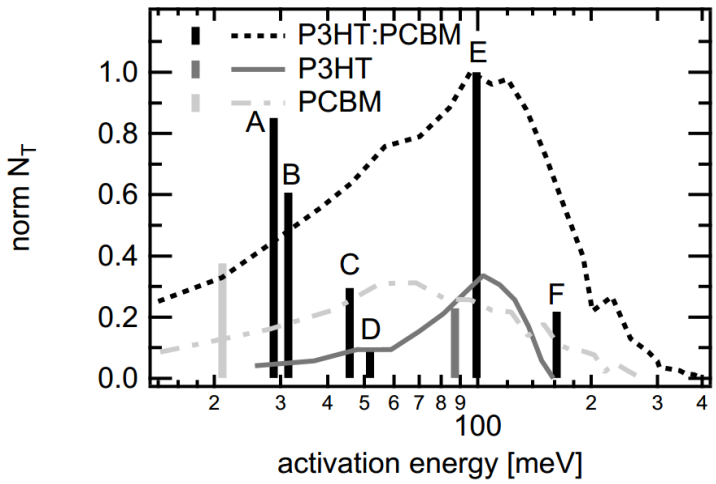

Figure 11: bars: overview of the obtained activation energies in PCBM (light grey), P3HT (dark grey) and P3HT:PCBM blend (black) and relative maximum N_T in the spectrum found by I-DLTS. Lines: normalize activation energy spectra of earlier TSC measurements [36,56,67] (colors are as above). Reprinted with permission from [57]. Copyright [2012], American Institute of Physics.

2.3.2 Levels in the donor and acceptor portions and blend unique bands

As referenced in Figure 11, trap bands in blended devices have also been examined through TSC measurements.[36] An ITO/PEDOT:PSS/P3HT:PCBM/Ca/Al structure was studied. Three TSC bands were found. Two (50 and 105 meV) precisely matched the bands of their

earlier neat P3HT TSC work,[56] while the third, which was centered deeper in the gap at 250 meV, was unique to the blend.[36] When comparing the TSC spectrum in blended devices to that of the neat films, a substantial broadening and increase in concentration was also seen.[36,56] This, coupled with the existence of the unique, deeper band in the BHJ devices, again shows higher energetic disorder in blended systems. It is immediately clear that the dominate band centered at *ca.* 100 meV is common between the DLTS and TSC blended film work.[36,57] Interestingly, the TSC 50 meV band, which the authors attributed to a polymer contribution, correlates well with DLTS bands 'C' and 'D', which were considered unique to the blend in the DLTS experiment.[36,57] Neglecting the disagreement in origin, DLTS bands 'C-D' seem to give more resolution to the TSC 50 meV, indicating two, closely spaced and overlapping trap sites make up this energy regime. The TSC 250 meV is in qualitative agreement with the DLTS 'F' band (i.e. both unique and somewhat deeper levels), albeit with a *ca.* 90 meV larger activation energy. The total trap density in the measured regime was estimated at $8x10^{16}$ cm^{-3} – 8x higher than that measured for neat P3HT, 4x higher than that of neat $PC_{60}BM$ and nearly 3x higher than their simple addition (P3HT+$PC_{60}BM$).[36,56,67]

In 2012, Yu *et al.* also weighed in on the trap distribution of P3HT:PCBM blended films.[75] The authors studied both conventional and T_{start}-T_{stop} TSC measurements on ITO/P3HT:PCBM/Al structured cells.[75] Conventional TSC revealed two trap bands, centered on 140 and 220 meV, not unlike the DLTS (160 meV) and TSC (250 meV) bands, respectively.[36,57,75] The group hypothesized more bands existed in this energy range, but were unresolved by the conventional TSC measurement. Thus, they turned to fractional TSC along with an extensive

numerical fitting to further resolve a complete picture of the tDOS. In all, five levels were cited (**Table 3**). As noted, both exponential and Gaussian distributions were seen with concentrations ranging between $8.0x10^{16}$ and $1.5x10^{19}$ cm^{-3}, significantly larger than that found in Schafferhans's bands. Again, two bands (N_3 and N_4) are in qualitative agreement with the DLTS 'F' (160 meV) trap and TSC 250 meV levels, respectively. Interestingly, the newly resolved N_2 is somewhat similar to the dominate 'E' band of Figure 11, while N_1 can be likened to the 'C-D' distribution. The authors theorized that traps N_1-N_3 stemmed from properties of the neat P3HT, while N_4 might have resulted from the addition of PCBM – somewhat different than the previous TSC and DLTS interpretations. Maybe most interesting is the deeper N_5 trap state. This band is only vaguely seen in other TSC data, but showed a strong presence here. According to the authors, this type of level is often observed at the high-temperature edge and may be due to a weakening of the stimulated current.[75] However, a similar band has also been noted through other techniques, potentially substantiating its existence. Further, one recalls the existence of a similar deep band in neat donor materials. Let us now turn attention to this band.

	E_a (eV)	Distribution				
		Type	Gaussian		Exponential	
			N_{g0} (cm^{-3})	σ (meV)	N_{t0} (cm^{-3})	E_t (eV)
N_1	0.06	Exp.	-	-	$1.8x10^{17}$	0.03
N_2	0.12	Exp.	-	-	$2.5x10^{18}$	0.03
N_3	0.14	Gauss.	$8.2x10^{16}$	52	-	-
N_4	0.20	Exp.	-	-	$1.5x10^{19}$	0.03
N_5	0.35	Gauss.	$2.7x10^{18}$	48	-	-

Table 3: parameters of electrically active trap distributions used in the curve-fitting procedure. Reprinted from publication [75], Copyright [2012], with permission from Elsevier.

Prior to Yu's work, this deep band had been studied using both CF and current modeling methods.[38,76] The first such work came in 2009 and centered on an ITO/POEDOT:PSS/P3HT:PCBM/Ca/Ag structure. The CV work of Dennler *et al.* had shown the existence of a Schottky junction between the organic and metal cathode.[14] Similar behavior was then suggested for blended films, allowing capacitance techniques to be leveraged on a BHJ system.[77,78] Employing the CF measurement (Refer to section 2.5.5 for details), Boix *et al.* revealed a prominent, Gaussian shaped deep defect band centered at *ca.* 380 meV above the HOMO, with N_T=1.2x10^{16} cm^{-3} and σ_T=66 meV (**Figure 12**), very similar to that mentioned in neat donor films.[38] For reference, an attempt-to-escape frequency ($\omega_0=2\pi\nu_0$) of 1x10^{12} s^{-1} was used (see equation (19)). One notes the immediate proximity of this band to the FTSC N_5 trap (albeit two orders of magnitude lower in density),[75] giving support to the presence of this deep trap in blended systems. Further, by comparing the energetic profile for active layers

comprising different P3HT:PCBM loadings – namely, 1:0.0, 1:0.4, 1:0.6, 1:0.8, 1:1.2 and 0:1.0 – Boix *et al.* showed the measured deep-defect distribution is not significantly affected by the presence of PCBM. This indicates that the band is inherent to the polymer donor. Interestingly, CV measurements show the ionized acceptor density in the blended films (*ca.* 4.3×10^{16} cm^{-3}) is only slightly larger than that of neat P3HT devices ($3.2 10^{16}$ cm^{-3}).[38] This indicates that the higher energetic disorder in blended films may not have a large effect on carrier concentration in these already moderately doped films.

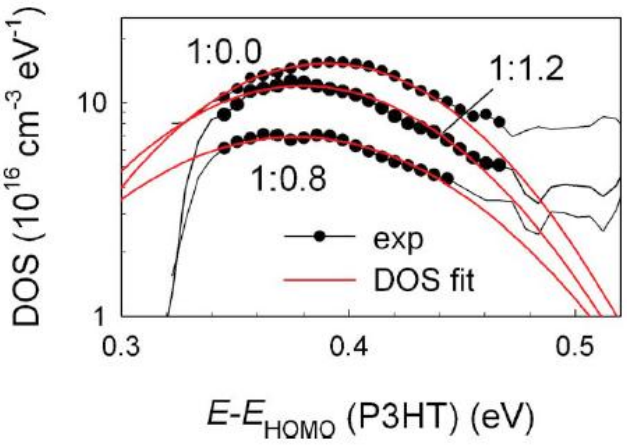

Figure 12: density of defect states as a function of the energy with respect to the P3HT HOMO level (demarcation energy), $E - E_{HOMO}$, calculated using Equation (3) [of the original article] and the capacitance spectra in Figure 1(a) [see original article]. Gaussian DOS fits (Equation (5) [see original article]) are also displayed. Composition of the blend is marked in each distribution. Reprinted with permission from [38]. Copyright [2009], American Institute of Physics.

It is worth noting, Boix *et al.* later revised the mean energy of this defect band, citing a newly revealed attempt-to-escape frequency of 33.42 s^{-1} *via* temperature dependent CF measurements.[79] This gives a revised mean energy of *ca.* 35 meV – an order of magnitude lower than the previously reported value and more like the DLTS 'A-B' bands than the TSC N_5 band.[79] For some comparison, similar temperature dependent CF measurements have also been conducted on ITO/MDMO-PPV:PCBM/Al[80] and ITO/PEDOT:PSS/MDMO-PPV:PCBM/Al[81] based devices. The former finds a shallower trap centered on 24 to 34 meV with a ν_0 in the range of $1x10^7$ s^{-1} (estimated from presented data).[80] The latter report finds two trap bands centered on 9 meV and 177 meV with characteristic escape frequencies of $1.3x10^7$ s^{-1} and $7.6x10^9$ s^{-1} respectively.[81] Campbell *et al.* also found an attempt-to-escape frequency in this range ($1x10^8$ s^{-1}) for PPV based devices, further corroborating the characteristic prefactor.[61] One notes the sharp difference in ν_0 between the P3HT and PPV materials and, of course, this highlights the necessity of obtaining an accurate value if one is to properly interpret measurements relying on emission data. It is also worth highlighting that Dyakonov *et al.*'s temperature dependent CF data shows similar trap behavior in PPV:$PC_{60}BM$ blended films to that in P3HT:$PC_{60}BM$ devices. From shallowest to deepest, bands with activation energies at 9, 22-34 and 177 meV have been identified and, of course, one might expect the presence of a the deeper, 750 meV level revealed by Campbell[61] in neat PPV – showing the qualitative resemblance to Figure 11.

Nonetheless, the N_5 trap band in P3HT:$PC_{60}BM$ BHJ devices was also shown by Nam *et al.* through current modeling measurements.[76] The authors used SCL and Poole-Frenkel current models to study trap band concentrations in air-processed ITO/PEDOT:PSS/P3HT:PCBM/gold

(Au) OPVs.[76] The selective Au cathode allowed hole transport (in the donor) to be isolated in reverse bias, which was subsequently subtracted from forward bias characteristics to yield information on the electron transport (in the acceptor). Hole current through P3HT was described by three main regions: (i) trap-filled SCL current in lower voltages, (ii) Poole conduction in intermediate voltages and (iii) Fowler-Nordheim tunneling at higher voltages. From region (ii), the total concentration of mid-gap states in the donor was calculated to be *ca.* $6x10^{20}$ cm^{-3}.[76] This value is two to four orders of magnitude higher than what is typically reported for neat or blended cells. However, these devices were processed in open air, which is known to increase the impurity concentrations. The effects of oxygen on trap states in blended systems will be more directly addressed later on. In any case, at the intersection of regions (i) and (ii), the average trap activation energy was calculated in the range of 300 to 500 meV – in agreement with the TSC measurements and unrevised CF work deep defect band.[38,75,76] As an interesting note, as expected from the neat film discussion, hole mobility in these air-processed devices was substantially lower than the typical values for devices processed in more inert atmospheres.

Continuing with Nam's work, electron transport in the $PC_{60}BM$ was also described by three main regions: (i) Schottky limited at lower bias, (ii) power-law SCL current at moderate bias and (iii) trap-free SCL current with a field-dependent mobility at higher biases. Using region (ii), with the assumption of an exponential DOS and the Equation (11) simplification (refer to section 2.5.3 for details), the authors found a relatively high electron trap density of *ca.* $1x10^{18}$ cm^{-3}.[76] As with the case of hole traps, they suspect this heightened density to be oxygen-related

stemming from the open air fabrication – a thought which is supported by the afore-discussed optical works centered on C_{60}, oxygen exposure and sub-gap states.[53,54] Interestingly, a blend-annealing process greatly increased the degraded electron mobility and pushed the power-law electron conduction towards trap-free transport.[76] This aligns their PCBM electron transport with that reported by Nicolai *et al.* for inert atmosphere processed diodes and indicates that significant traps in $PC_{60}BM$ (and other acceptors) may be present if oxygen exposure is appreciable.[65] Further, this highlights the well-known fact that thermal annealing is effective at removing structural defects and introduces the idea that oxygen induced states may be revisable by thermal treatments.

In blends comprising of higher adduct fullerenes (e.g. bis$PC_{61}BM$), enhanced disorder and electron trapping [when compared to $PC_{60}BM$ based blends] has been reported.[66] Lenes *et al.* investigated such solar cells and found a sharp reduction in the current-voltage characteristics of electron single-carrier devices. Coupled with a Gaussian disorder model, enhanced energetic trapping in the higher adducts was found – in-line with that expected from the TSC measurements on neat fullerene films.[66,67] Interestingly, the authors found that this additional disorder did not have any detrimental effects on the photovoltaic performance of the blends – indicating these traps are rapidly filled under illumination.[66] This leads nicely into a discussion on how defects affect OPV performance. Clearly, trap states should only be considered if they have a substantial impact on electronic properties and photovoltaic conversion. The subsequent section discusses some important works highlighting such impacts.

2.3.3 Traps and OPV performance

Continuing the dialog on the impact of disorder in the acceptor portion, others have indicated these states may indeed have adverse effects on the achievable performance, even in $PC_{60}BM$ based BHJ devices. Garcia-Belmonte *et al.* have investigated the effects of fullerene electronic states in blended devices through open-circuit impedance spectroscopy (IS) (refer to section 2.5.7 for details).[34] In the cited work, BHJ cells derived from blends of P3HT and $PC_{60}BM$ were compared to that of blends of P3HT and 4,4'-dihexyloxydiphenylmethano[60]fullerene (DPM_6).[34] A significant positive shift in the V_{oc} of the DPM_6 device was noted.[34] To study its origins, the open-circuit impedance was measured at Illumination intensities corresponding to a V_{oc} between *ca.* 200 and 800 mV. An energetic DOS was then generated, where $g(E_{Fn})$ was taken to be a single Gaussian distribution (**Figure 13**).[34] The displayed states were termed *intermediate* to signify they lay below the fullerenes' upper lying LUMO,[34] indicating the measured DOS may be a part of the LUMO tail or a separate band altogether. Clearly seen in Figure 13 is a slight shift in central energy and a significant increase in the concentration of the $PC_{60}BM$ intermediate states. As a result, it is concluded that E_{Fn} in PCBM based devices is *pinned* at deeper energies within the intermediate-DOS distribution. This induced a reduction of the difference between the polymer E_{Fp} and fullerene E_{Fn}, thereby, reducing the achievable V_{oc}.

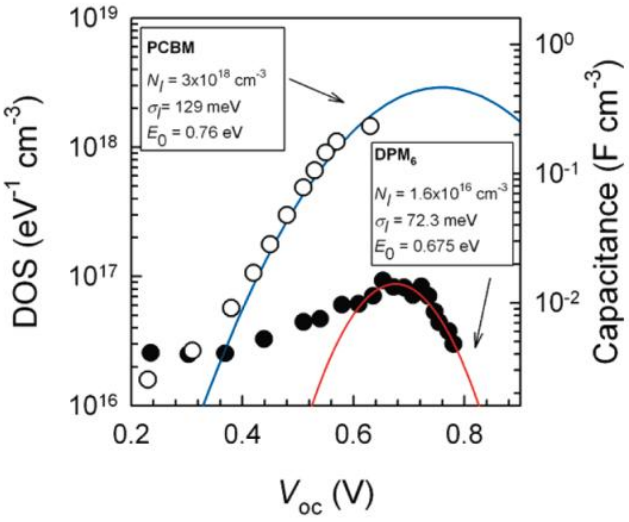

Figure 13: capacitance values extracted from fits of the low-frequency arc of the impedance spectra as a function of V_{oc} reached under varying illumination levels. White dots correspond to PCBM-based solar cells and black dots to DPM_6-based solar cells. Gaussian DOS (solid lines) and distribution parameters resulting from fits. Reprinted with permission from [34]. Copyright [2010], American Chemical Society.

Further, such bandgap residing states in both donor and acceptor portions of OPV devices may be detrimental to photovoltaic performance through recombination enhancement, especially if they are spatially located at or near a donor-acceptor domain interface. A recent work by Street *et al.* highlighted this by systematically exploring the recombination kinetics in BHJ organic solar cells, carefully examining the possibility of Auger, geminate and non-geminate exciton and interface state recombination. Though a series light-intensity and temperature dependent experiments coupled with theoretical modeling, the authors suggested mono-molecular recombination through defects occurring at or near the domain interface(s) as a dominant loss mechanism plaguing photovoltaic performance.[31] It should be stated that these

experiments were conducted on PCDTBT (poly[[9-(1-octylnonyl)-9H-carbazole-2,7-diyl]-2,5-thiophenediyl-2,1,3-benzothiadiazole-4,7-diyl-2,5-thiophenediyl]) $PC_{70}BM$ BHJ devices, however, the authors feel the conclusions may be general to other blended systems (such as P3HT:PCBM).[31] Street *et al.* have also given some guidance as to improving OPV conversion efficiency – intuitively, by reducing the density of states at or near the domain interfaces. Interestingly, given a thicker device (200nm), the model employed by Street *et al.* suggested that even an order of magnitude reduction of the interface states could as much as double the device's photovoltaic conversion efficiency.[31] It is worth noting that some disagreement on this topic can be found throughout the literature.[82,83]

Other works have investigated trap-assisted recombination more emperically.[30,32] Cowan *et al.* studied such a case for PCDTBT:$PC_{60}BM$ devices.[32] The introduction of $PC_{84}BM$ impurities to the blend induced dramatic losses in the photovoltaic performance of the devices. Impurity concentrations as low as one part in one thousand were found to reduce conversion efficiency.[32] The losses were directly linked to the intentional addition of theses electronic states, which augmented trap-assisted recombination, hampered charge transport and reduced carrier mobility.[32] By monitoring the open circuit voltage as a function of light intensity and trap density, the authors also gave some indication as to the impurity-level threshold where trap-assisted losses become significant. This threshold will be contingent on several factors – with the trap density and generation rate (light intensity) being the most notable.[32] Qualitatively speaking, Cowan *et al.* propose trap-assisted recombination effects become dominant at high trap densities and/or low light intensities. The works of Mandoc *et al.* give some

substantiation.[30,84] In the first, the authors investigated the deliberate introduction of electron traps to devices derived from blends of PPV and $PC_{60}BM$.[30] A degradation of open circuit voltage, short circuit current and fill factor was clearly seen. Again, the losses were attributed to an enhancement in trap-assisted recombination,[30] highlighting in the limit of high trap densities, trap-assisted losses can dominate. In a second work, Mandoc *et al.* studied all polymer solar cells based on a blend of PPV and PCNEPV (poly-[oxa-1,4-phenylene-(1-cyano-1,2-vinylene)-(2-methoxy-5-(3', 7'-dimethyloctyloxy)-1,4-phenylene)-1,2-(2-cyanovinylene)-1,4-phenylene]).[84] No extra traps were added, however, inherent electron traps in the acceptor portion gave rise to a dominant trap-assisted recombination loss, but only at low light intensity.[84] This gives substantiation to the second portion of Cowan *et al.'s* proposal. This also shows that in current and new material systems variations in structural disorder (inherent to the material or by varying fabrication parameters), variations in oxygen exposure, variations in synthesis impurities, etc. may induce varying amounts of trap-assisted losses – indicating trap states should be carefully monitored. Further, even if the trap states are kept at a reasonable level, they should not be forgotten as these solar cells under normal operating conditions will see lower light intensities, and thereby, trap-assisted loses.

Aside from trap-assisted recombination, charge trapping is also thought to facilitate space charge effects.[33,85] In a 2009 report, Mcneill *et al.* studied photocurrent transients in all polymer BHJ cells to reveal the trapping and detrapping of electrons.[33] The transients were induced by the application of a square light wave at a given frequency, of which the pulse width, intensity and presence of background illumination (also of varying intensity) were

varried.[33] A sharp transient peak just after *turn on* of the pulse coupled with long transient tail after *turn off* was revealed and attributed to the trapping/detrapping of electrons. The authors proposed such trapping may facilitate space charge effects, where charges trapped near the anode would perturb the internal electric field to: (i) decrease the probability of charge separation and (ii) promote bimolecular recombination.[33] Both of which yield loses in conversion efficiency.

Before continuing on to a discussion on trap origins, it is worth segwaying to the identification and characterization of electronic defects at the edges of the blend; that is, at the blend-electrode interfaces.

2.3.4 Electrode interface states

Electronic states at the interfaces between the BHJ blend and charge collection layers have also been identified. Towards the anode, Ecker *et al.* have profiled trap bands using the CF measurement in ITO\hole transport layer (HTL)\P3HT:PCBM\Ca\Al structured cells.[86] Devices comprising different HTLs, namely PEDOT:PSS and polyaniline:poly(styrene sulfonate) (PANI:PSS) based in water and alcohol solvents, were examined.[86] The CF experiments were conducted under 16 mW/cm^2 and 100 mW/cm^2 illuminations at open circuit conditions. Two Gaussian distributions in the energetic tDOS were revealed. The first, lower energy distribution was attributed to bulk states. A ν_0 was not measured or assumed, thus, a comparison with the other CF experiments cannot be made. Though, it is likely that these states are the same deep states as those previously mentioned.[21,38] The second, higher energy Gaussian was attributed to

electronic states at the HTL interface. The concentration of the interface states was found to be significantly higher than that of the bulk states, highlighting their strong presence in this system. Interestingly, non-encapsulated devices with HTLs based in water solvents presented with additional trap states at the blend-HTL interface,[86] showing the importance of defect considerations when choosing such interlayers. It is interesting to speculate how these traps may affect OPV performance. Most conducive may be the space charge effects discussed by McNeill *et al.*, where charges trapped near the anode may retard charge separation and promote bimolecular recombination.[33]

Near the cathode, Bisquert *et al.* have also identified interface trap states.[87] Similar to Ecker *et al.*, the interface states were identified through capacitance measurements under illumination – here, CV measurements on an ITO/PEDOT:PSS/P3HT:PCBM/Al structure were studied.[87] The extracted ionized acceptor density was similar in both dark and illuminated conditions (*ca.* 4-5.0x10^{16} cm^{-3}); however, the built-in potential was found negatively shifted by 0.6 V in the illuminated case. This shift is explained through a photovoltaic model which incorporated a concentration of kinetically slow surface states at the organic-metal junction.[87] Under illumination an accumulation of minority charges, and thereby a charging of surface states, induces band unpinning and the noted V_{bi} shift.[87] This change in energetics may significantly alter photovoltaic performance,[87] again highlighting the importance of defect considerations at layer interfaces. Further quantification of these states has not yet been given.

2.3.5 Trap origins: Oxygen, structural and synthesis residuals

Having discussed the identification of trap states throughout the BHJ structure, let us now find some indication as to the origins of the blend-film trap states. I first return to the 2010 TSC work on BHJ ITO/PEDOT:PSS/P3HT:PCBM/Ca/Al structures.[36] Coupled with the thermal experiments, CELIV and IV measurements as a function of synthetic air (80% N_2, 20% O_2, < 1 ppm H_2O) exposure were examined. Upon exposure, in contrast to the case of neat P3HT, the magnitude of the 105 meV trap appears to decrease.[36,56] However, a new band at *ca.* 142 meV emerged, with a concentration linked to exposure time.[36] As a result, the total trap density in the measured energy spectrum remained constant through 100 hr of exposure.[36] Though, it must be noted that the measurement only gives a lower limit for the total trap density (refer to section 2.5.1 for details). The recombination of charge carriers could be masking an increase in trap density and/or causing the apparent decrease of the 105 meV band. Nonetheless, it is clear that oxygen is inducing or augmenting states somewhat deeper in energy. This data is supplemented with CELIV mobility and carrier density measurements. A decrease in carrier mobility along with an increases in charge density was found.[36] This is in line with that expected from the discussion on unblended systems. This data, coupled with macroscopic simulations, is correlated to degradations in the solar cell IV. The authors assert increased carrier densities dominate the degradation of J_{sc}, while the increased deep(er) trap concentration may be at the origin of V_{oc} and FF degradation,[36] perhaps through enhanced trap-assisted recombination losses and space charge effects. The link between excess charge carriers and J_{sc} degradation is supported by Seemann *et al.*, who noted a large portion of oxygen-induced degradation stems from excess mobile holes and immobile superoxide anions.[46] Interestingly, an experimental

correlation between photocurrent and the concentration of charge carriers in blended P3HT:PCBM was noted by Guerrero *et al.*, who found $J_{sc} \propto n^{-0.14}$.[68] Clearly, the oxygen generation or enhancement of bandgap residing states has a significant effect on the long term stability of these devices. Please note, the topic of degradation is vast and, though heavily related, beyond of the scope of this chapter. Many excellent reports can be found in the literature, I have chosen only to comment on a select few which indicate some effects of degradation on the trap states. A full review on OPV degradation can be found elsewhere.[88]

Turning to the yet deeper (*ca.* 380 meV) band discussed above, details as to its formation have been provided by Nalwa *et al.*, who applied the CF method to ITO/PEDOT:PSS/P3HT:PCBM/Al cells with active layers spun at different rates.[21] Each spin rate produces a different film thickness, which greatly alters the drying time, and thereby, morphological ordering.[60] Many prior reports had shown the promotion of self-assembly improves OPV performance through enhanced morphology, carrier mobility, etc.[60] Thus, the authors set out to study the dependence of the deep-trap energetic profile on the film growth-rate.[21] The group found that films spun at lower speeds (thicker and slower drying) are more ordered and contained nearly a magnitude less deep traps than those spun at higher speeds (thinner and faster drying). Defect densities of 3.3×10^{15} and 2.1×10^{16} cm^{-3} and mean energies of 360 and 380 eV ($\nu_0 = 1 \times 10^{12}$ s^{-1}) were found for devices with active layers spun at 400 and 1,000 rpm respectively.[21] If the assumed attempt-to-escape frequency is accepted, this band closely matches the above reports and the data indicates the defect has origins in intrinsic structural impurities. A similar case was also shown by Sharma *et al.* for CuPc based devices.[89]

Of course, impurities from synthesis residuals cannot be forgotten. As discussed in section 2.2.5, contamination during material synthesis can have detrimental effects on device parameters. In the case of a palladium catalyst, this has been evidently highlighted for P3HT:PCBM based BHJ devices.[72,74] In their work on the development of a quality control measurement tool, Troshin *et al.* investigated the effects of an intentional addition of tetrakis(triphenylphosphine)palladium(0) ($Pd(PPh_3)_4$) to P3HT:PCBM cells.[72] 0% to 10.5% by weight addition of palladium was investigated. As can be seen in **Figure 14,** the transition metal has a dramatic effect on the solar performance parameters. With an increasing impurity concentration open circuit voltage, short circuit current and fill factor were rapidly reduced. Even at palladium concentrations as low as 0.07% a reduction in performance was noted.[72] A similar case has also been found for palladium additions in higher efficiency organic solar cells (based on PTB7 (poly[[4,8-bis[(2-ethylhexyl)oxy]benzo[1,2-b:4,5-b']dithiophene-2,6-diyl][3-fluoro-2-[(2-ethylhexyl)carbonyl]thieno[3,4-b]thiophenediyl]])), where the degradation in performance parameters in devices containing 5% ($Pd(PPh_3)_4$) was directly linked to greater trap-assisted recombination.[73] This, of course, is in nice agreement with the works discussed above – that is, higher trap densities leads to a dominance of trap-assisted recombination losses. Extending to contaminants other than palladium, such a thought is further supported. In a work by Leong *et al.*, trace concentrations of (MePT)DTS($PTTh_2$) in the molecular material *p*-DTS($PTTh_2$)$_2$ were found to originate from the synthesis process.[17] Through generation and recombination studies, the authors found evidence of more energetic trap states in the impure films, even at very low contamination levels. As a result, this extrinsic impurity limited the PCE

of BHJ structured cells (ITO/molybdenum oxide/*p*-DTS(PTTh$_2$)$_2$:PC$_{70}$BM.Al) to *ca.* 3.0%.[17] Indeed, OPV devices based on more purified *p*-DTS(PTTh$_2$)$_2$ material exhibited a substantially higher PCE at *ca.* 6.5%, again highlighting the importance of purifying these types of extrinsic impurities.

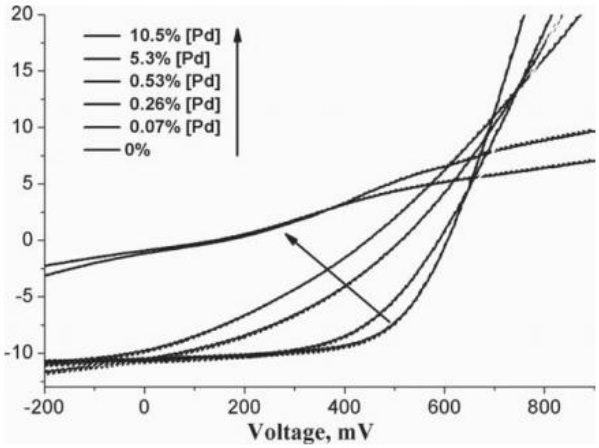

Figure 14: effect of [Palladium] impurities on the *I-V* characteristics of P3HT/PCBM organic solar cells. Reprinted with full permission from [72]. Copyright [2010], John Wiley and Sons.

Evidently, the same primary sources inducing defects in neat films have similar effects on blended systems. Defect bands have been shown to be heavily influenced by the degree of structural ordering as well as by exposure to oxygen/moisture. Impurities introduced during material synthesis also clearly play a role; though it is unclear at this point which of the above-discussed mid-gap levels can be attributed to residuals such as palladium. Nonetheless, this highlights the path towards lowering electronic defects in OPV devices likely includes structural ordering, the removal and minimization of oxygen exposure and the purification of raw materials.

2.4 Identification and characterization: miscellaneous loose ends

Before moving forward, this section is used to tie up loose ends pertaining to the important and ubiquitous capacitance measurements. Much work has gone into interpreting the capacitive response of inorganic cells and I suspect the same will prove true for organics. The goal of this section is to provide some contrast to the works above and direct the reader toward alternate interpretations as well as known issues.

First, the dual MS slope commonly seen in CV measurements must be revisited. The works above interpreted this change in slope as either spatial contributions from an inhomogenous doping profile or energetic contributions from a deep defect band. However, other interpretations have been applied to organic CV profiles and should be considered. One such explanation was provided by Nolasco *et al.* in 2010 as well as Ecker *et al.* in 2011.[86,90] In the latter, the BHJ CV data clearly contains two regimes with differing slopes. The first, at low forward/reverse bias, was attributed to the 'donor phase', while the second, at moderate reverse bias, was attributed to the 'acceptor phase'. Meaning, in region (i), the authors assume $N_{D\ PCBM} >> N_{A\ P3HT}$ – creating a one-sided junction where the MS slope is governed by $N_{A\ P3HT}$. In region (ii), as the P3HT depletes, $N_{D\ PCBM}$ begins to dominate and a new slope emerges. The authors find $N_{A^-\ P3HT}$ = 1.0 to 3.0x10^{16} cm^{-3} and $N_{D^+\ PCBM}$ = 0.5 to 2.5x10^{18} cm^{-3}, both in line with the expected values. Aside from highlighting an alternative interpretation of the dual slope, this also brings about an interesting discussion on which junction in the BHJ structure is being probed by the capacitance experiments. It is clear that Ecker *et al.* have assumed the donor-

acceptor junction, much like a classical p-n treatment. However, others have indicated that the Schottky junction between the polymer and cathode is being measured.[38,78] Of course one might also consider contributions from a Schottky junction between the fullerene and anode, which is expected to form with proper energy alignment and moderate doping.[58,91] Though, more heavily doped fullerenes may show essentially ohmic behavior.[58] Some combination thereof might also be considered. More work is required to pinpoint the exact nature.

Similarly, alternative interpretations of CF have surfaced. The formalism used in the above reports was presented by Walter *et al.* in 1996.[92] However, Cohen and Lang have also discussed the dynamic response of Schottky barriers and interpretations of their model have been applied in organic works.[93-95] Most interesting is that by Reis *et al.* in which capacitance measurements as a function of both frequency and temperature were analyzed using a derivation[96] of the model described by Cohen and Lang as well as that described by Walter *et al.* (Au/doped-polyaniline/Al structure).[94] Interestingly, a comparison of the density of defects derived from each model showed they were in good agreement.[94] Being that both yield a similar concentration, it is my interpretation that the Mencaraglia *et al.* application of the Cohen formalism is advantageous as the Fermi-level and Debye length [among other parameters] are easily found; while the Walter formalism is advantageous as an energetic profile of the tDOS is obtained. The latter is typically preferred, though a best case scenario may be represented by an analysis and comparison of both models. Of course, one must also ensure the assumptions of each model are suitable for the material system at hand.

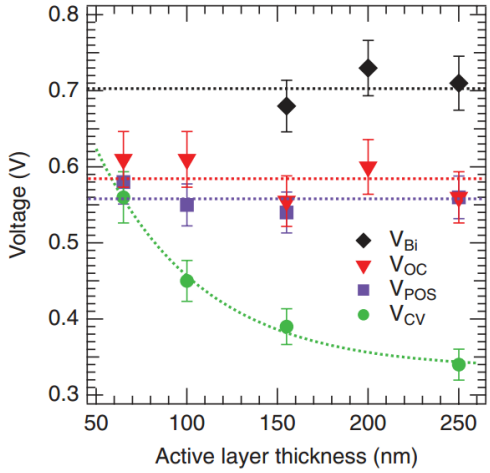

Figure 15: V_{bi} (black diamonds, determined as shown in Fig. 5 [of the original article]), V_{oc} (red triangles), V_{pos} (purple squares), and V_{cv} (green circles) for P3HT:PC_{61}BM bulk heterojunction solar cells with varying active layer thickness. In contrast to V_{oc}, V_{pos}, and V_{bi}, V_{cv} shows a clear dependency on the active layer thickness (increases with decreasing thickness) and approaches V_{pos}. The dotted lines are guides to the eyes and mark the mean values of the corresponding potentials resp. an exponential fit to V_{cv}. Reprinted with permission from [97]. Copyright [2011] by the American Physical Society.

Lastly, potential issues in the MS CV analysis must be mentioned. In 2011, Mingebach *et al.* reviewed the validity of determining the built in voltage of OPV devices via the MS method.[97] Though this paper itself does not directly discuss defects, its conclusions are important to examine as the Walter *et al.* CF method relies on an accurate value of V_{bi}, which is typically determined by MS analysis. Citing differences in the MS measured and theoretically expected V_{bi}, the interpretation of the MS intercept as the built in voltage was questioned. Further, a thickness dependence in the MS measured V_{bi} was found (**Figure 15**); another indication the

measurement may not be accurate.[97] These points, coupled with temperature-dependent measurements, caused Mingebach *et al.* to conclude that the classical idea of the MS intercept may not be applicable to BHJ based OPVs. Kirchartz *et al.* further studied this concept in 2012.[98] The group started with the question of how OPV devices can have a V_{bi} significantly lower than V_{oc} (as measured from CV MS), but still produce efficient cells with practical FFs.[98] Through simulations and experimental work, the authors showed that MS analysis on OPV devices is highly sensitive to both film thickness and the inherent doping level.[98] In too thin or lowly doped films, charge carriers injected near the electrodes cannot be neglected. This breakdown in the depletion approximation greatly affects the accuracy of the capacitance data, and thereby, may cause errors in the analysis. Most notable is an apparent decrease in N_A^- with increasing film thickness. In the case of a film doped to $5x10^{15}$ cm^{-3}, it is only at thicknesses greater than *ca.* 150 nm that the measured density of acceptor states saturates to the appropriate level and the method is considered generally applicable. Similar to Mingebach *et al.*,[97] this thickness dependence was also seen in V_{bi} – a result directly connected to the apparent decrease in doping. As a result of the work, the authors assert that CV analysis for the accurate determination of N_A^- may only be appropriate when films are thick and/or more heavily doped, while the accurate determination of V_{bi} may be difficult, no matter the material parameters.[98] Of course, with the assumption that these capacitance measurements target only the polymer-cathode Schottky interface, one might consider that the obtained V_{bi} relates only to that particular junction and does not set an upper limit on the photovoltaic voltage.[99]

2.5 Measurement techniques

To conclude this introductory chapter, the basic concepts of commonplace defect measurement techniques are presented. A summary, quantification and relevant references are presented for each.

2.5.1 Thermally stimulated current (TSC)

In a basic sense, the conventional TSC method can be understood as follows. The sample is first cooled to cryogenic (or near cryogenic) temperatures and excess charge carriers are generated (e.g. optically or through a pulsed voltage bias) to induce a long-lived filling of the trap states. Subsequently, the sample is slowly heated at a linear rate, stored charges are thermally emitted and the stimulated current is monitored. Thereby, a current versus temperature (e.g. Figure 3) spectrum is generated. Both the concentration and mean energy of the dominate trap can then be calculated. The former is quantified by,

$$\int_{total} I_{TSC} dt \leq qN_T \qquad \textbf{(3)}$$

where I_{TSC} is the thermally stimulated current and q the elementary charge.[100,101] As can be seen, this technique only gives a lower limit of the total trap density. Recombination between thermally released electrons and holes can cause some stimulated current to be 'lost', lowering

the measured trap states. Further, incomplete trap filling and/or limited detrapping can also lower the measured results. The mean trap energy is quantified by,

$$E_T = k_B T_{max} \ln\left(\frac{T_{max}^4}{\beta}\right) \quad \textbf{(4)}$$

where k_B is the Boltmann constant, T_{max} the temperature at the current peak and β the heating rate.[102]

2.5.2 Fractional thermally stimulated current (FTSC)

An extension of the conventional method in which fractional heating cycles are used to further resolve the temperature/energy spectrum is known as T_{start}-T_{stop} or fractional TSC (**Figure 16**).[103] As usual, the sample is first cooled to a minimum temperature (T_{start}) and then trap filled. However, the sample is next scanned (heated) to an intermediate end temperature (T_{stop}), which is less than the final temperature of interest – 'prerelease'. Subsequently, the sample is again cooled to T_{start} and then, without a second trap filling, scanned to said final temperature – 'main run'. This fractional cycle is then repeated for increasing T_{stop} temperatures. Assuming the initial rise of the fractional TSC interval (**Figure 16**) is described by a Boltzmann activated process, the activation energy for each T_{stop} can be found via the 'initial rise method', which is quantified by,

$$I_{iTSC} \propto \exp\left(\frac{-E_T}{k_B T}\right) \quad \textbf{(5)}$$

where I_{iTSC} is the current of the initial rise and T the temperature.[103,104] The activation energy can then be coupled with a concentration, calculated from Equation (3), to build an energetic tDOS.

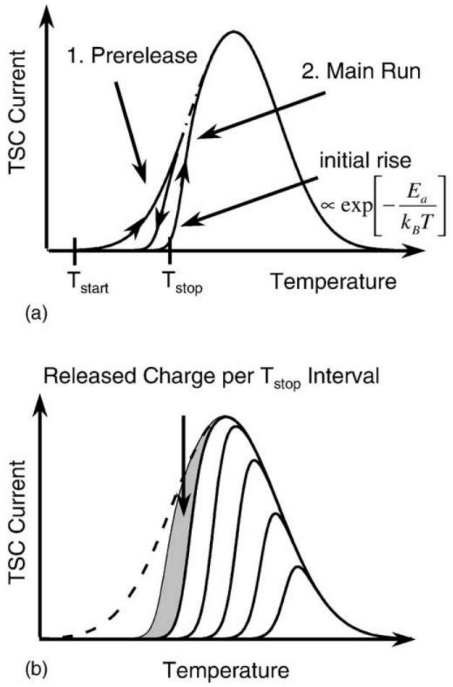

Figure 16: schematics of the T_{start}-T_{stop} method: (a) the basic cycle consists of two individual TSC scans and (b) the whole measurement is a replication of basic cycles with different T_{stop} temperatures. The activation energy of the initial rise describes the energetic trap depth, while the shaded area resembles the released charge. Reprinted from publication [102], Copyright [1990], with permission from Elsevier.

2.5.3 Space charge limited (SCL) current modeling

Dark current-voltage characteristics can also be examined to determine trapping parameters. Neglecting diffusion and assuming a constant mobility, the current density in a single carrier, *p*-type material is described by,

$$J = q\mu_p F(x) p_f(x) \quad \textbf{(6)}$$

where μ_p is the hole mobility, F(x) the spatial distribution of the electric field and $p_f(x)$ the spatial density of free holes.[55,105,106] The spatial distribution of the electric field is given by the Poisson equation,

$$\frac{dF(x)}{dx} = \frac{q}{\varepsilon_s}[p_f(x) + p_T(x)] \quad \textbf{(7)}$$

where ε_s is the semiconductor permittivity and $p_T(x)$ the spatial density of trapped holes, which is defined by,

$$p_T(x) = \int_0^\infty g(E) f(E, E_F, T) dE \quad \textbf{(8)}$$

where g(E) is the DOS and $f(E,E_F,T)$ the Fermi function for occupation.[55,105,106] Thus, with the definition of $E_F(x)$,[105] numerical integration yields a current density, which can be coupled to a voltage via,

$$V = \int_0^d F(x)dx \quad \textbf{(9)}$$

where d is the sample thickness.[55] Extensive modeling as such yields information on the energetic distribution. If an exponential or Gaussian distribution of traps is assumed such that $p_f < p_T$, some further simplifications can be made. In the case of an exponential distribution,

$$g(E) = \frac{N_T}{k_B T_T} \exp\left(\frac{-E}{k_B T_T}\right) \quad \textbf{(10)}$$

where T_T is the characteristic temperature, the drift-only current density is readily approximated by,

$$J = q^{1-l} \mu_p N_V \left(\frac{2l+1}{l+1}\right)^{l+1} \left(\frac{l}{l+1}\frac{\epsilon_s}{N_T}\right)^l \frac{V^{l+1}}{d^{2l+1}} \quad \textbf{(11)}$$

where V is the voltage and $l = T_T/T$.[107] When a Gaussian distribution is assumed,

$$g(E) = \frac{N_T}{\sqrt{2\pi}\sigma_T} \exp\left(-\frac{(E-E_T)^2}{2\sigma_T^2}\right) \quad \textbf{(12)}$$

two considerations must be made. For shallow trap centers, the current density is approximated by a modified Mott-Gurney law,

$$J = \frac{9}{8}\varepsilon_s \mu_p \vartheta \frac{V^2}{d^3} \quad \textbf{(13)}$$

where ϑ is a scaling factor[108] and $\mu_p\vartheta$ represents the effective mobility dependent on the ratio of free to trapped charges. For deep trap centers, the current density is again approximated by Equation (11), but with a modified exponent (l') and concentration of trap states (N_T').[108] In contrast to these simplifications, others have gone the opposite direction to employ more complex modeling which accounts for diffusion current as well as electric-field and carrier concentration dependencies of the mobility.[109] It should also be pointed out that the use of SCL and modified SCL models is seemingly ubiquitous in the device literature, however, its application to π-conjugated polymers has been called into question.[39]

2.5.4 Capacitance versus voltage (CV)

Capacitance measurements have long been employed to study mid-gap states in semiconductor devices. CV measurements exploit the existence of a depletion region, formed at a semiconductor junction. Consider, for example, an ideal *p*-semiconductor/metal Schottky junction. In such a case the depletion capacitance is defined by,

$$C_d = {}^{\epsilon_s A}/_{W}, \quad \textbf{(14)}$$

which can be linearized to reveal the well-known Mott-Schottky (MS) relation,

$$1/C^2 = \frac{2}{A^2 q \epsilon_s N_A}(V_{bi} - V_{app}) \quad \textbf{(15)}$$

where W is the depletion width, N_A is the acceptor impurity density, V_{bi} the built in voltage and V_{app} the applied bias.[62] Strictly speaking, a better approximation replaces V_{bi} with V_D, where V_D is the diffusion potential and related to V_{bi} by $qV_{bi} = E_F + qV_D$.[110] Nonetheless, a plot of $1/C^2$ versus the applied DC voltage produces a straight line with the slope related to N_A and the intercept to V_{bi}. In an inhomogeneously doped material, the spatial distribution of acceptor states can be determined through the related profiler equation,

$$N_A(x) = \frac{C^3}{q \epsilon_s A^2} \frac{dV}{dC} \quad \textbf{(16)}$$

where x is the spatial distance from the junction. These equations, however, represent an idealization of a *perfect*, pure material. When deep defects are present, especially if they are in large numbers, several considerations must be made to properly interpret capacitance data. Most notably, defect contributions to the capacitance as a function of DC bias as well as AC frequency must be accounted for. The former is briefly summarized here and the latter is addressed in section 2.5.5.

The influence of deep traps on CV measurements was discussed by Kimerling in 1973.[63] Though many considerations must be made to accurately employ the interpretation, the

formalism can be summarized as follows. In the popular case when trap emission ($e_{n,p}$) is slower than the AC measurement frequency (v_{AC}) the trap is considered frozen and does not contribute to the capacitance as a function of the small-signal oscillation. However, if trap emission is faster than the change in DC voltage (ΔV_{DC}), the trap can alter its occupancy over the course of the voltage sweep, and thereby, contribute to the capacitance as function of DC bias.[63] In such a case, $v_{AC} > e_{p,n} > \Delta V_{DC}$ and the 'N_A' measured by Equation (15) or (16) actually represents,

$$N(x) = N_T(x_T)\left[1 - \frac{W - x_T}{W}\right] + N_A(W) \qquad \textbf{(17)}$$

where x_T is the spatial demarcation where E_T is within k_BT of E_F and W-x_T is assumed constant.[62,63] Thus, when x_T is small, $N_A(x)$ indeed represents N_A. However, for larger values of x_T (note, x_T is always less than W), $N_A(x)$ more closely represents N_A+N_T.

2.5.5 Capacitance versus frequency (CF)

Deep defects states can also contribute to the capacitance measurement through a dynamic response to the AC small-signal. This forms the basis for capacitance versus frequency (CF) measurements, which were discussed by Walter *et al.* in 1996.[92] CF, also termed admittance spectroscopy, is a frequency differential in which the junction is maintained at a steady state DC voltage and the modulation speed of the small-signal AC measurement is swept to include (or exclude) trap states. The thermal emission rate of a trap state in a *p*-type semiconductor is quantified by,

$$\frac{1}{\tau_p} = e_p = N_V v_{th} \sigma_p \exp\left(\frac{-E_A}{k_B T}\right) \quad \textbf{(18)}$$

where N_V is the valence band density of states, v_{th} the thermal velocity, σ_p the capture cross-section, E_a the trap activation energy.[62,81] In inorganic device physics, with an assumption that $v_{th} \propto T^{1/2}$, $N_V \propto T^{3/2}$ and σ_p independent of T, the prefactor in Equation (18) is commonly written in terms of T^2 – e.g. 'ζT^2' or '$\Upsilon \sigma_p T^2$' where $\zeta = N_V v_{th} T^{-2} \sigma_p$ and $\Upsilon = N_V v_{th} T^{-2}$ respectively.[62,81] Alternatively, the prefactor is often written as a single, temperature independent parameter, v_0, termed the attempt-to-escape frequency.[84, 111] Taking the latter, the switching speed of the small-signal measurement inherently defines an energy demarcation which divides those defects that can emit charge and contribute to the capacitance from those that cannot,[62,92,111]

$$E_\omega = k_B T ln\left(\frac{\omega_0}{\omega}\right) \quad \textbf{(19)}$$

where ω is the applied angular frequency. As ω is swept from high to low frequencies, the demarcation energy is moved from below the Fermi-level, where no states can respond, to above the trap level(s), where all states respond (**Figure 17**).[62,92] Note that only those states at the Fermi-level efficiently contribute and, in the low frequency limit, only those states between the mid-gap and Fermi-level will be probed.[92] An energetic profile of the tDOS can be found via,[92]

$$N_T(E_\omega) = -\frac{V_{bi}}{qW}\frac{dC}{d\omega}\frac{\omega}{k_B T}. \quad \textbf{(20)}$$

This profile is then fit with a Guassian or exponential model and the characteristic trap parameters are extracted.

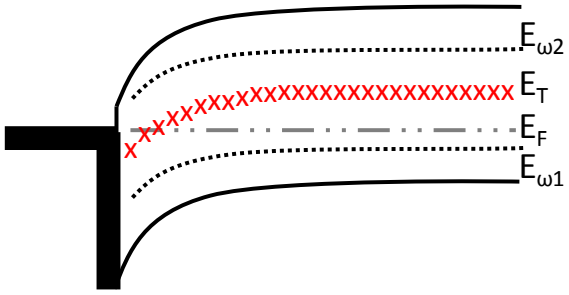

Figure 17: simplified *p*-type Schottky band diagram showing the CF experiment. E_F shows the Fermi-level energy, E_T the trap level, $E_{\omega 1}$ a high frequency demarcation where no states can respond and $E_{\omega 2}$ a low frequency demarcation where all states can respond.

2.5.6 Drive-level transient spectroscopy (DLTS)

Also exploiting the depletion capacitance is DLTS. This powerful capacitance technique monitors transient changes in the capacitance signal induced by a voltage or optical pulse to study trap characteristics.[62] The technique was pioneered for crystalline semiconductors and later extended for amorphous materials.[112,113] Though the approach is slightly more in depth, the advantages lay in the extracted parameters. Along with trap band magnitudes, capture cross-section and activation energies, emission rates and trap types (i.e. majority or minority trap) can be easily examined.[62] It is worth noting, Sharma *et al.* have cautioned that, owing to

the high resistivity and low hole mobility of some organic layers, DLTS may not be a suitable defect characterization technique for all organic applications.[89 and ref [12] therein]

2.5.7 Open-circuit impedance spectroscopy (IS)

Though the strict definition of impedance spectroscopy (IS) might include the previously discussed CF and CV measurements, I have kept their nomenclature separated in order to highlight a segregation in their use and analysis. Nonetheless, the IS method considered here is simply an application of the CF measurement at different, typical forward, voltage potentials. The results are typified by a Cole-Cole plot and can be used to study the density of photogenerated carriers, carrier mobility, carrier lifetime and the electron density of state.[34,78,99] In the latter, which is of particular interest here, the impedance characteristics are measured at open circuit conditions, where recombination precisely balances generation (**Figure 18**).[99] To accomplish this, the photovoltaic device is illuminated at different intensities and a bias is applied to compensate the photovoltage. As such, the steady-state complex impedance examined is that of a chemical capacitance,[34,78,refs therein] which is dominated by changes in the electron quasiFermi-level (E_{Fn}) and defined by,

$$\frac{C_{\mu}}{A} = Lq^2 \frac{dn}{dE_{Fn}} \qquad \textbf{(21)}$$

where L is the active layer thickness. [99] Assuming a zero-temperature Fermi distribution,[99]

$$\frac{C_\mu}{A} = Lq^2 g(E_{Fn}). \quad \textbf{(22)}$$

Thereby, with small-scale movement of the polymer E_{Fp}, the fullerene DOS in the BHJ blend is readily obtained as E_{Fn} moves through the distribution at different illumination intensities (Figure 18).

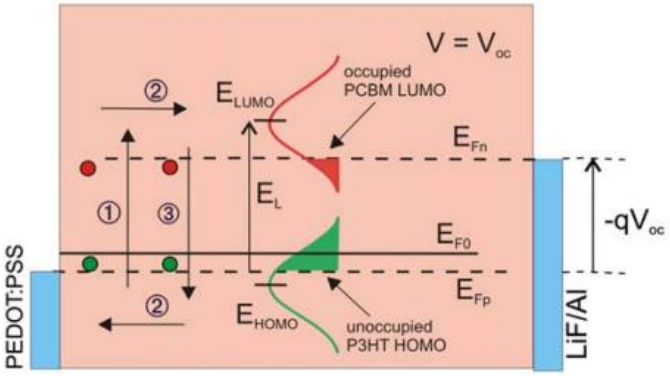

Figure 18: band structure of the P3HT:PCBM heterojunction in steady-state illumination under open-circuit conditions ($V=V_{oc}$). Main dynamic processes occurring in the blend layer: excess holes and electrons are photogenerated (1) into the P3HT HOMO and PCBM LUMO manifolds, respectively. Charge carriers diffuse along the diode bulk (2), and eventually recombine (3). Molecular orbitals spread in energy (DOS) following Gaussian shapes. The occupancy level of LUMO (HOMO) states is determined by competing photogeneration and recombination rates. This in turn governs the achievable V_{oc} which depends on the splitting of the quasiFermi-levels, $-qV_{oc}=E_{Fn}-E_{Fp}$. The DOS centers are located at E_{LUMO} and E_{HOMO}, respectively. The relative position of the Fermi-level in the dark E_{F0} is also indicated. Reprinted from publication [99], Copyright [2010], with permission from Elsevier.

3 CHAPTER III: ON ACCURATE CAPACITANCE OF OPV DEVICES

It is the goal of this dissertation to add to the works described above and push the identification and characterization of defect bands in OPV devices forward. As will become apparent in the subsequent chapters, impedance spectroscopy – namely, capacitance versus frequency and capacitance versus voltage – is the author's measurement of choice as it gives detailed information on the deep defect states in the system. Thus, as an initial study, work detailing the accurate capacitance characterization of OPV devices is presented. This work was published in *Applied Physics Letters* in 2011.[114]

3.1.1 Project introduction and motivation

Capacitance spectroscopy has been employed to study semiconductor properties for many years. As mentioned in Chapter II, these techniques have been recently adopted by the organic photovoltaic (PV) community to probe device aspects such as doping density,[14,59,115] deep trap states,[21,38,89] carrier mobility,[59] active layer thickness[116] and the like. It is well understood that these measurements can be very sensitive, and are plagued by issues such as high impedances, leaky capacitances and noisy cabling. Of upmost importance in maintaining reliable measurements is the selection of the proper model (e.g. parallel, series or multiple parameters) during the measurement process. A conventional measurement employs the equivalent circuit shown in **Figure 19(a)**, where R_s represents the series resistance, R_p the parallel resistance and C the capacitance. With three unknowns, measurements must be taken at two frequencies and complex equations must be solved to find the capacitance and its associated parasitics; see reference [117] for example.[117] For simplicity, this equivalent circuit can be accurately modeled

by either the series (highlighted by blue, solid box) or parallel (highlighted by red, dashed box) segment, depending on which portion dominates as per the capacitance, resistances, frequency, etc. In a typical solar cell, the series resistance is expected to be quite small and the parallel resistance quite large. Therefore, for large capacitive impedances, the parallel portion overshadows that of the series and dominates the measurements. In this case, the parallel model gives an accurate approximation of the equivalent circuit. In contrast, as the magnitude of capacitive impedance approaches that of the series resistance, the series model gives the most accurate approximation. Within the inorganic community, parallel parameters are typically employed. Owing to smaller series resistances and larger capacitive impedances, this parallel model remains accurate over the usual frequencies employed (e.g. 10 Hz – 2 MHz). In this report, it is shown that this detail is not directly transferrable to organic PV cells – the parallel parameters cannot be indiscriminately used. When comparing organic and inorganic cells with similar contact area, our data shows series resistances are typically two or more times higher and capacitive impedances three or more times lower in the organic devices. This moves the transition from the parallel model to the series model to lower frequencies – which can be within the range of interest. Thus, a hybrid of the two models must be employed to accurately measure the capacitance over the frequency range of interest. It is shown that, if the improper parameters are used, geometric capacitances are underestimated, deep trap states are overestimated and general conclusions are greatly misinterpreted. Although model choice may be a known concept, several evidences of improper model usage within the organic PV literature can be found.

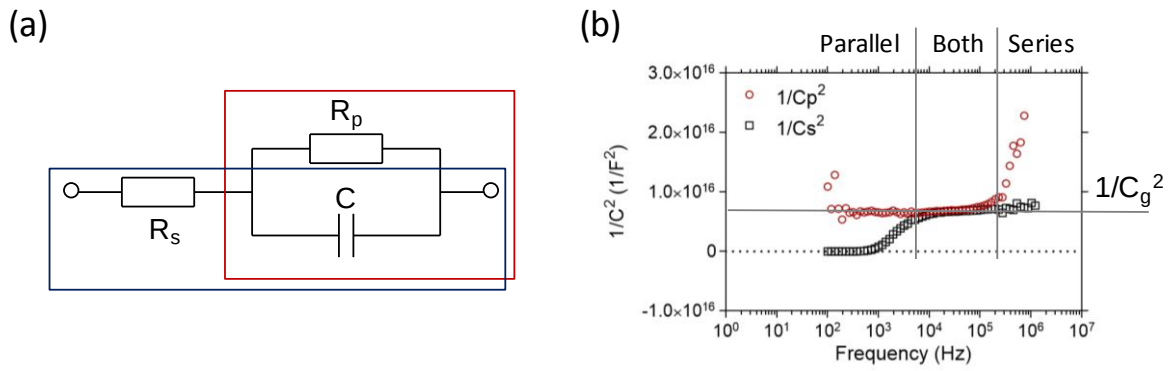

Figure 19: (a) simple equivalent circuit for small signal measurements. Any lead inductance is neglected here. The series approximation is highlighted by a solid blue box and the parallel by a dashed red box. (b) Capacitance ($1/C^2$) versus frequency for a PCBM only device. Both C_s and C_p parameters are shown. The calculated geometric capacitance is highlighted by a gray line.

3.1.2 Experimental and photovoltaic performance

BHJ based cells were fabricated from P3HT (NANO C, Inc.) and PCBM (NANO C, Inc.). Solutions of 1:0, 1:1, and 0:1 by weight P3HT:PCBM were mixed with ortho-Dichlorobenze (ca. 10 or 20mg/ml; Sigma-Alrich) and magnetically stirred at 45ºC for at least 12 hours in an argon atmosphere. Indium-doped tin oxide (ITO; Delta Technologies) substrates were then treated by consecutive 5 minute sonications in four solutions: (i) isopropyl and acetone (50:50 v/v), (ii) detergent mixed with deionized water, (iii) ethanol and methanol (50:50 v/v), and (iv) pure deionized water. The ITO substrates were then blown dry with nitrogen and treated with air plasma (Harrick Scientifc) for 5 minutes. A ca. 28 nm (characterized by optical, as well as, surface profile techniques) poly(ethylenedioxythiophene): poly(styrenesulfonic acid) (PEDOT:PSS; H C Stark) film was spin-coated (4,000 rpm for 60 s in open air) onto the treated

substrates, and the casted films were annealed on a digital hot plate at 120 ºC for 10 min in open air. The blend solutions were then filtered via glass syringe and a 0.20 µm PTFE filter (Sigma-Aldrich). The active layer was then spun at 500 rpm for 60 s onto the PEDOT covered substrates in an argon atmosphere. The films were slow dried in individual Petri dishes to allow for solvent annealing. Lastly, a ca. 1500 Å thick Al cathode was thermally evaporated onto all devices at a rate < 5 Å/s under a 10^{-5} to 10^{-6} mBar vacuum. The completed organic solar cells were then allowed to cool to room temperature before beginning characterization.

To ensure photovoltaic behavior, current density versus voltage characteristics (**Figure 20**) were taken by illuminating the devices at room temperature using an ELH quartzline lamp at 1 sun (calibrated using a KG-5 filtered crystalline silicon reference photodiode). **Table 4** summarizes the device performance.

V_{oc} (V)	J_{sc} (mA/cm^2)	FF (%)	PCE (%)
0.60	9.30	58.20	3.25

Table 4: summary of photovoltaic performance parameters for a sample P3HT:PCBM device.

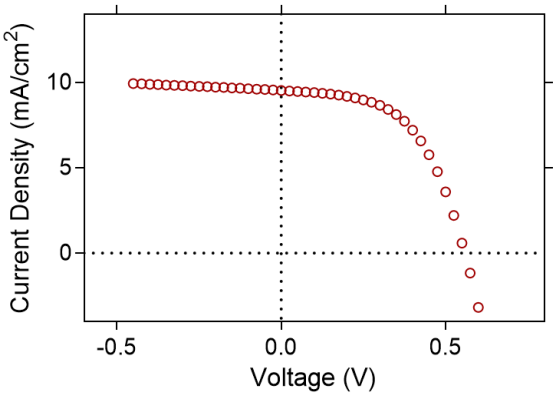

Figure 20: photovoltaic performance of the studied P3HT:$PC_{60}BM$ BHJ cells.

Capacitance data was taken on two different setups to ensure accuracy: the first being a PARSTAT 2273 (defined working range of ±10 VDC and 10 μ - 1 MHz), and the second being a Quadtech 1920 LCR (defined working range of ±2 VDC and 20 – 1 MHz). Both setups were calibrated using a low loss 715p orange drop capacitor (Vishay). Measurements were conducted at room temperature and in dark conditions to ensure optical, as well as, thermal equilibrium. Both impedance and admittance parameters were recorded for comparison in post processing calculations. The dissipation factor (d) was carefully monitored and all data associated with d >10 was neglected. Thickness measurements were conducted on an atomic force microscope (AFM) by scratching the film with a sharp needle and measuring the step height.

3.1.3 Capacitance profiling of OPV devices

PCBM only: as an initial example, I first turn to the capacitance versus frequency (CF) measurement of a PCBM only device. PCBM is a fullerene derivative of the C_{60} (or C_{70}) buckyball

that does not show deep state characteristics in its CF profile. Thus, a flat capacitive response with respect to frequency is expected.[38] This response represents a geometric capacitance, C_g = $\epsilon A/t$ ($\epsilon \equiv$ the permittivity, A ≡ contact area, and t ≡ thickness), in which only the dielectric is contributing. **Figure 19(b)** displays the CF spectra of one such device. One immediately notes the geometric capacitance (horizontal gray line at ca. $6.5x10^{15}$ $1/F^2$ according to the measured thickness of ca. 35 nm, A =.1256 cm^2 and ϵ = 3.9) requires both models to be accurately represented between 100 Hz and 1 MHz – a typical frequency range of interest as it reaches from near the Fermi-level[118] to above the deep trap profile.[21,38] For those frequencies below 7.5 kHz, the parallel parameters gave the best measurement as high impedances of the parallel portion of the circuit overshadow that of the series component and dominate the voltage divider. Between 7.5 kHz and 100 kHz both models gave a good approximation, differing by less than 1%. At frequencies above 100 kHz the series model gave the best approximation. At these frequencies, the parallel impedance-combination of R_p and C falls rapidly owing to the lowering of the capacitive impedance. As this impedance becomes comparable with R_s, the series resistance becomes significant and can no longer be ignored. The large parallel resistance, however, acts as a current divider and, with sufficiently small capacitive impedances, can be neglected. Note that the typically thin active layer of organic films (ca. 100-200 nm) gives a larger capacitance, which causes this transition from the parallel to series to emerge at much lower frequencies than their inorganic counterparts. Frequencies below 100 Hz gave dissipation factors as high as ca. 50, indicating a very leaky capacitor whose measurement is most likely overwhelmed by noise. Above 2 MHz it is expected that the series model will continue to

dominate. The PCBM device data illustrates the notion that indiscriminately using a parallel approximation across the spectrum does not transfer to organics.

P3HT:PCBM BHJ devices: the above directly translates to bulk heterojunction (BHJ) devices comprising a 1:1 weight ratio of P3HT:PCBM. **Figure 21(a)** plots C versus F for one such device. A pattern similar to the PCBM only device emerges, where lower frequencies favor the parallel approximation, higher frequencies favor the series and those in-between can be estimated by either. One notes the parallel model still gives relatively reasonable values at higher frequencies. However, these values differ from the series model by anywhere between 1 and nearly 200% for this particular device. The choice of which of these models is most accurate is convoluted by the fact that, unlike PCBM only devices, the polymer adds a deep-trap profile.[10,14,21,38] Thus, the expected capacitance is somewhat unknown. However, at sufficiently high frequencies, the demarcation energy at which neither mobile charges nor trap states respond can be surpassed and only the dielectric contributes to the capacitance. Thus, the geometric capacitance should be expected. This frequency was found experimentally to be ca. 1.5 to 2 MHz depending on the particular device. Qualitatively, the energy corresponding to this frequency range makes sense as it is nearing or slightly less than the equilibrium Fermi-level of P3HT (ca. 0.33 eV with doping ca. $1x10^{16}$ – $1x10^{17}$ cm^{-3} as determined by 1 MHz capacitance versus voltage (CV) analysis[63]). This geometric capacitance is further confirmed by applying a large (-2 VDC) reverse bias along with the entire small-signal frequency spectra in order to fully deplete the active layer – the same C_g was obtained for all frequencies at -2 VDC. Keeping this geometric capacitance in mind, the series model gave the most accurate approximation above

1.5 MHz. Further, note that only the series capacitance reaches a plateau at these frequencies, while the parallel capacitance continues to drop. Extrapolating back, this indicates that the series model should be used for all frequencies greater than 11 kHz in these particular devices. This has two main implications for common applications of capacitance measurements: (i) C_g and thickness measurements and (ii) determination of deep trap profiles. Both will be discussed in detail later in this chapter.

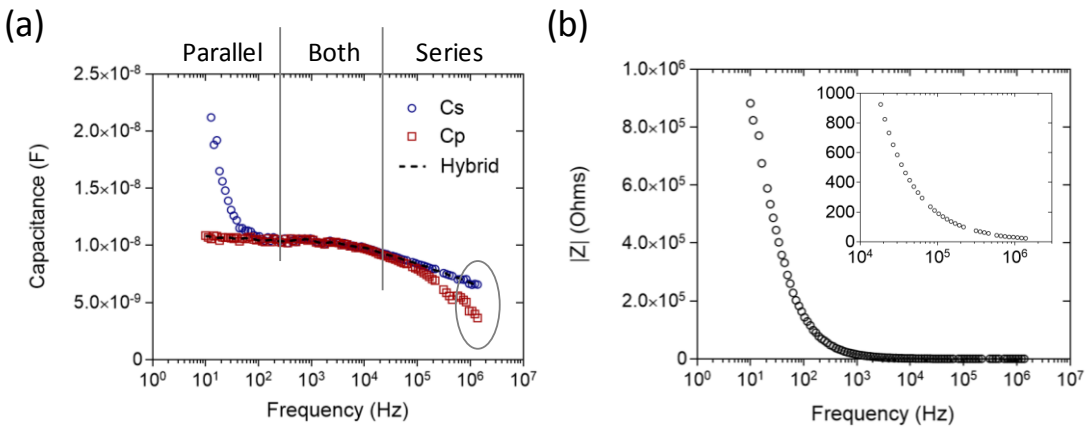

Figure 21: (a) capacitance versus frequency for a typical P3HT:PCBM 1:1 BHJ PV device. The ellipse highlights differences in the geometric capacitance obtained by each model. (b) Impedance versus frequency plots showing an exponential decrease in the impedance magnitude. The inset magnifies the 10 kHz to 1.5 MHz regime where |Z| drops below 1 kΩ

Of course, the boundaries at which the model must change are highly dependent on the device. Smaller capacitances, as well as series resistances, can push the parallel to series transition into higher frequencies. With a sufficiently low capacitance and R_s combination, the change may not even be noticed within the define frequency range; as is typically the case with

silicon cells. A well-known technique for monitoring model choice is to track the magnitude of the impedance (**Figure 21(b)**).[119] The general guidelines which are typically used are: (i) the parallel approximation for $|Z| > 10$ kΩ, the series approximation for $|Z| < 1$ kΩ, and either for 1 kΩ < $|Z|$ < 10 kΩ. Figure 21(b) shows good agreement with these guidelines.

Model failure examples: I next turn to the literature and some of my own data to highlight inconsistencies generated by improper model usage. These inconsistencies seem to have led and, in the future, may lead to incorrect data, misinterpreted conclusions or both. In a recent report by J. V. Li et al., capacitance techniques were used to simultaneously measure carrier density and mobility in organic semiconductors.[59] Although I generally agree with their method, I find inconsistencies in the measured geometric capacitance and the conclusions directly drawn from it. In the report, P3HT only films were characterized by the CV method (-3.0 V to +0.5 V) at different frequencies (100 Hz – 1 MHz). The authors found that at frequencies of 10 kHz and above, the film did not exhibit a MS response. This indicates that 10 kHz is the boundary above which mobile charges as well as trap states cannot respond and only the geometric capacitance is measured. From this, one is left to draw the conclusion that CV and other capacitance measurements (CF, deep-level transient spectroscopy, etc.) should be conducted at frequencies lower than 10 kHz. Qualitatively, this conclusion seems implausible as the demarcation energy of 10 kHz is ca. 0.477 eV ($E_\omega = E - E_{homo} = kT\ln(\omega_0/\omega)$[120] with ω_0 estimated at 1×10^{12} s^{-1}), which is nearly 0.1 eV above the Gaussian center of the deep trap profile in P3HT films.[21,38] Thus, at 10 kHz, one would expect these lower lying trap states and mobile charges to respond.[63] Further, our data does not support this 10 kHz conclusion as MS

behavior for frequencies as high as 1 MHz on P3HT only devices. As a possible explanation for this discrepancy, the differences between the series and parallel approximations for CV data between 100 Hz and 1 MHz is explored. As shown in **Figure 22(a)**, the models give an indication of much different device behavior at 1 MHz on our cells, with the series approximation showing MS behavior and parallel showing only a dielectric response. Here, the impedance magnitude indicates that the series model is more accurate. Note that this particular P3HT device did not show low impedances (i.e. <1 kΩ) until ca. 300 kHz owing to a slightly smaller capacitance than that of the referenced work. As further evidence that the parallel parameters give an incorrect depiction of device behavior, I turn to the reverse bias region (-2 VDC). Here, the layer is fully depleted and it is clearly seen that the parallel model underestimates the geometric capacitance by ca. 250%. Thus, Figure 22 shows that, for a typical P3HT device, frequencies as high as 1 MHz may still be valid for capacitance spectroscopy, and the currently published 10 kHz data is most likely the result of model misinterpretation. The exact uppermost usable frequency will be dependent on the material's Fermi-level, and thus can change from device to device. P3HT doping has been reported in the range of 10^{15} – 10^{17} cm^{-3}, from which the Fermi-level can be estimated to sit at 0.36 eV above the valence band or lower. This corresponds to freeze out frequencies of ca. 900 kHz or higher. Even doping profiles as low as 10^{14} cm^{-3} still give a Fermi-level of ca. 0.42 eV or a ca. 100 kHz upper frequency. The above finding has further implications for the method of measuring capacitance to find active layer thickness. It has been noted that improper model employment can underestimate C_g by as much as 300%. As a result, thickness can be significantly overestimated if the model is not properly adjusted.

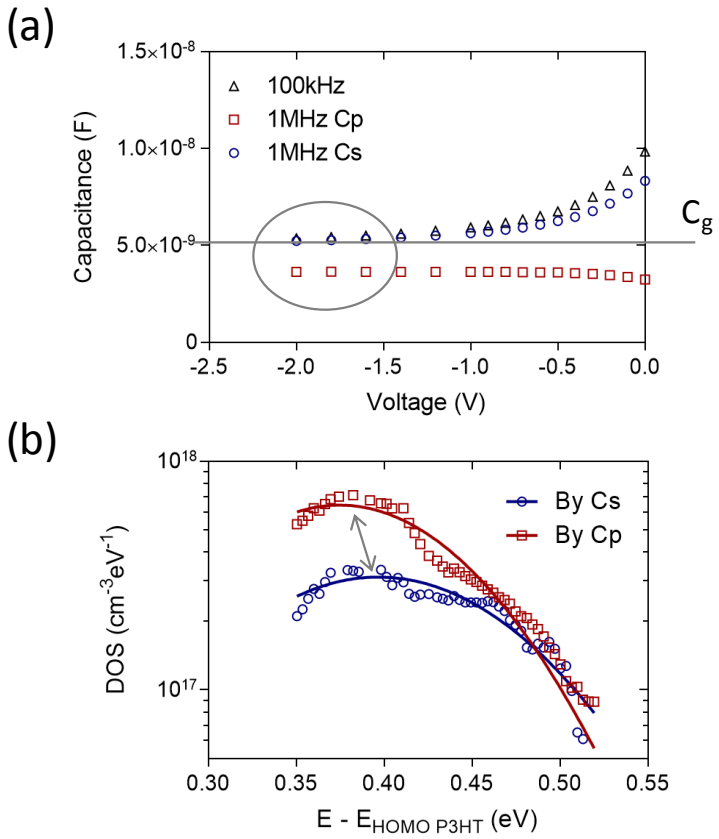

Figure 22: (a) capacitance versus voltage for P3HT only device at 100 kHz and 1 MHz. Calculated geometric capacitance is highlighted by the horizontal line. The differences in the geometric capacitance obtained by the models are shown within the circle. (b) Density of trap states versus demarcation energy for P3HT:PCBM 1:1 device. The arrow shows the shift in the Gaussian amplitude and central energy between the two models.

Next, the determination of deep-trap density of states (tDOS) in organic cells is explored. This method, which is detailed elsewhere,[38] combines CV with CF characterization to sweep through the bandgap and map defects states. As previously highlighted, the series model gives the best approximation for 1:1 BHJ based devices at higher frequencies (10 kHz to 2 MHz).

The demarcation energies of these higher frequencies range from 0.477 eV to 0.339 eV. One immediately notes that this is over the range of the reported Gaussian deep-defect profile.[21,38] By comparing these models in Figure 21(a), a large difference in slope is readily apparent. Thus, as highlighted in **Figure 22 (b)**, if the improper model is employed, the tDOS magnitude and distribution center can be over- and under-estimated, respectively. Using the parallel approximation, N_t is overestimated by ca. 110% and the central energy to be underestimated by about 20 meV.

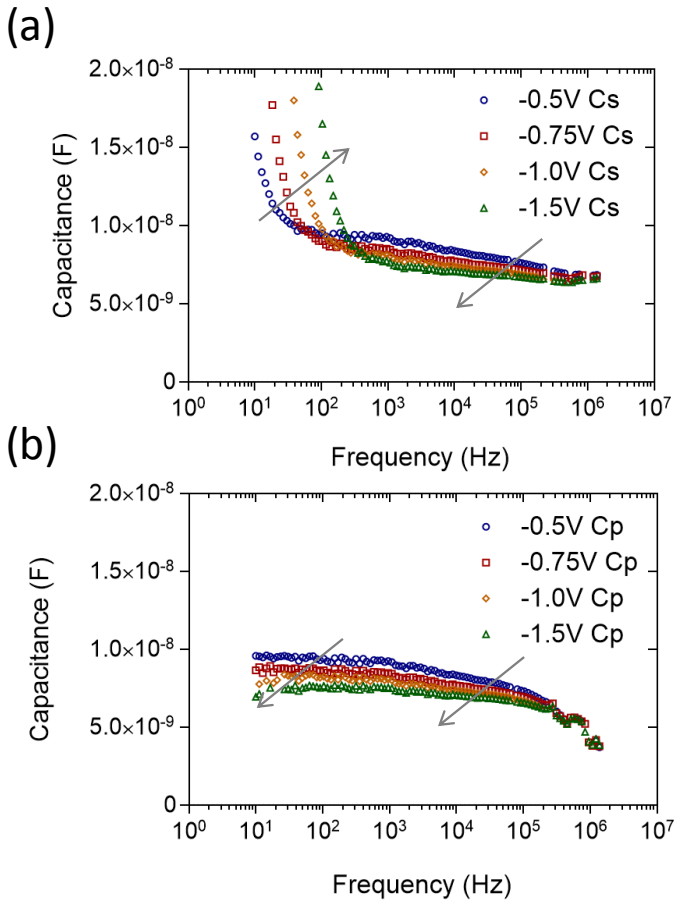

Figure 23: capacitance versus frequency as a function of reverse bias for (a) the series model and (b) the parallel model. The arrows indicate the direction of increasing reverse bias.

Lastly, a 2008 report by G. Jarosz is investigated.[121] In this report, the author casts doubts on MS analysis of organic planar heterojunction cells. Although the report in its entirety is not questioned, a single plot displaying C versus F as a function of reverse bias is reviewed. Here, the author correctly expects the measured frequency-dependent capacitance to decrease with an applied reverse bias. More generally stated, as the reverse bias is increased, the active-layer begins to deplete and the capacitance at all frequencies decreases to approach the geometric capacitance. The report, however, finds an increase in capacitance with reverse bias for frequencies less than ca. 400 Hz and draws doubts on MS analysis in their cells. Although I cannot state whether MS analysis is valid or not on Jarosz's planar cells, it can be highlighted how improper model employment could cause one to incorrectly reach the same conclusion – even on P3HT:PCBM BHJ cells. **Figure 23** shows 1:1 BHJ CF analysis as a function of applied DC reverse bias for both the series (**Figure 23(a)**) and parallel (**Figure 23(b)**) models. The series model closely represents the data of the aforementioned report. This artifact arises as a direct result of the series approximation. As frequency decreases, the capacitance impedance increases and the parallel portion of circuit Figure 19(a) dominates. By continuing to monitor the series portion, the true capacitance measurement is lost. The parallel model removes this artifact and gives the expected response. Hence, by monitoring only the series model, one might reach improper conclusions owing to inaccurate data.

3.1.4 Project conclusion

Herein, the capacitance model choice was reviewed in an effort to improve capacitance measurements on organic PV cells. Although series versus parallel model selection may be a known issue, evidences in the literature that it is being overlooked within the organic PV community are found. Owing to higher series resistances and lower capacitance impedances, the parallel approximation cannot be indiscriminately used over the frequency range of interest. Most importantly, improper model employment can cause discrepancies in the geometric capacitance by as much as 300%, discrepancies in the tDOS by as much as 110%, and, more in general, misinterpreted conclusions. This work shows that while performing capacitance characterization, it is critical to monitor the impedance magnitude and correspondingly employ the appropriate capacitive circuit model.

4 CHAPTER IV: ON THE IDENTIFICATION OF DEEPER DEFECT LEVELS IN OPV DEVICES

Now armed with a greater understanding of accurate capacitance measurements, such techniques can be leveraged to further study defect bands in OPV devices. This chapter presents a detailed application of the impedance spectroscopy characterization to reveal previously unknown deep defects in P3HT based devices. Further, this chapter gives general guidance as to how to apply to the broad impedance theory to organic solar cells. This work was published in the *Journal of Applied Physics* in 2013.[122]

4.1.1 Project introduction and motivation

As mentioned above, bandgap residing trap levels can significantly affect many of the parameters which have been identified as bottlenecks to OPV performance. Chapter II details the work to date on profiling such levels in P3HT films between the HOMO and *ca.* HOMO + 0.45 eV. However, no report has profiled *deeper* towards the mid-gap, an energy regime which is expected to house a distribution of trap levels.

In this chapter, using CF, CV and trap-free dark-current modeling, the presence of deeper defects in P3HT:PCBM OPVs are reported. The main band is revealed by low frequency (<1 Hz) CF, which is analyzed using the model of Cohen and Lang as well as that of Walter *et al.*[92,93] This band is then confirmed by a point-by-point differential of high frequency CV, which in turn indicates a uniform doping profile. The total traps discovered via capacitance are well correlated to the total traps measured by dark current modeling, substantiating the measurements and assumptions. Lastly, a comparison of P3HT:PCBM based devices to pure

P3HT diodes with two different cathode interfaces shows the traps measured here are likely inherent to the polymer bulk.

4.1.2 Theoretical background

In P3HT based cells, the polymer becomes *p*-doped with exposure to oxygen or moisture[10,11] and creates a Schottky-junction at the cathode,[14,78,123] allowing for capacitance measurements to be leveraged. **Figure 24a**, which depicts the MS relation of a model OPV device for different AC frequencies, shows an example of such a case. As discussed above for amorphous and/or impure materials, a strong dependence on both frequency and direct current (DC) bias is seen. In the low forward\reverse bias region, an increase in the MS slope with increasing frequency is clearly present. This highlights the capacitive response of defect states as a function of the small-signal oscillation. As described above, the thermal emission rate of a trap state in a *p*-type semiconductor is quantified by,

$$\frac{1}{\tau_p} = e_p = N_V v_{th} \sigma_p \exp\left(\frac{-E_A}{k_B T}\right) \qquad \textbf{(23)}$$

where N_V is the valence band density of states, v_{th} the thermal velocity, σ_p the capture cross-section, E_a the trap activation energy, T the temperature, k_B the Boltmann constant and where $N_V v_{th} \sigma_p$ defines the attempt-to-escape frequency.[62,81,93] Thus, the small-signal measurement inherently includes [or excludes] trap states as per the AC frequency.

This dynamic response is commonly explained in terms of a spatial abscissa, where a distance from the junction interface, x_ω, is defined as per the applied frequency where $\omega\tau_p=1$.[93,95] Traps crossing the quasiFermi-level further from the junction (with $\omega\tau_p \leq 1$) can change their state and contribute to the depletion capacitance, while those closer cannot. Assuming a constant trap density of states (tDOS), the formalism of Cohen and Lang and work of Mencaraglia *et al.* then shows the depletion capacitance to be defined by $C_d = \varepsilon A/(x_\omega + L_D)$, where L_D is the Debye length.[93 96] The Debye length is defined by

$$L_D = \left[\frac{\varepsilon_S}{q^2 N_T(E_{F0})}\right]^{\frac{1}{2}} \quad \textbf{(24)}$$

which is further related to the CF measurement through

$$\left[\frac{d(\varepsilon_S A/C)}{d(ln\omega)}\right]^{-1} = \frac{1}{L_D}(\ln \omega_{T0} - \ln \omega) \quad \textbf{(25)}$$

where ω is the applied angular frequency and ω_{T0} is the turn on angular frequency.[94,96] Thus, an estimation of the tDOS [among other parameters] is readily obtained.

Similarly, the AC response of trap states is commonly explained in terms of a demarcation energy, defined by,[92,94,111]

$$E_\omega = k_B T ln\left(\frac{\omega_0}{\omega}\right) \quad \textbf{(26)}$$

Traps below this demarcation (i.e. closer to the Fermi-level) can change their change state and contribute, while those above cannot. Through the formalism of Walter *et al.*, a tDOS profile can then be found through the differential,[38,62,92]

$$N_T(E_\omega) = -\frac{V_{bi}}{qW}\frac{dC}{d\omega}\frac{\omega}{k_B T} \quad \textbf{(27)}$$

Of course, this formalism has already been more thoroughly discussed above. The Walter formalism is highlighted in **Figure 24b**, where the known deep-trap in P3HT based cells is reproduced.[38] It is interesting to note that it is not until frequencies greater than 1 MHz that a significant portion of this deep-defect band is frozen or not responding. Thus, in the CV data of Figure 24a, as the frequency is swept higher, the measured N decreases from $p+N_T$ to approach p as the traps are progressively excluded – explaining the frequency dependence.

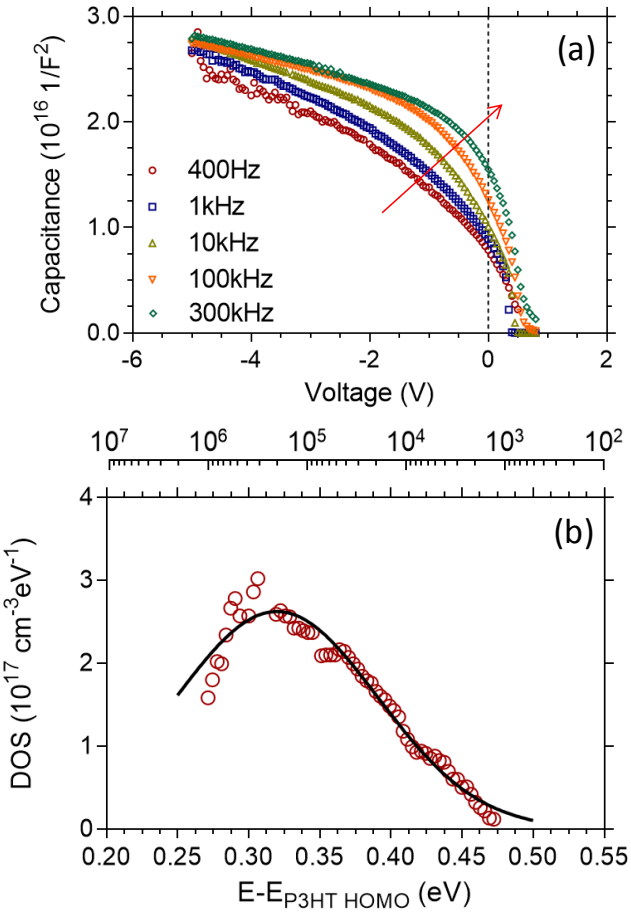

Figure 24: (a) Mott-Schottky form of CV measurements on P3HT:$PC_{60}BM$ BHJ cell. The arrow indicates increasing frequency. (b) Analysis of CF data *via* the Walter *et al.* interpretation showing the deep-defect Gaussian. E_v is shown on bottom x-axis and frequency (Hz) on top.

The second artifact seen in Figure 24a is a change in the MS slope as per increasing reverse bias. Namely, at a given frequency between -5 and +1 V_{DC} a straight line, as expected from the ideal MS treatment, is not noted. Instead, a rolling slope is clearly present. As mentioned above, this could be caused by a non-uniform doping profile, as interpreted by Dennler *et al.*[14] However, as stated by Li *et al.* and formalized by Kimerling, the change may also be due to the contribution of energetically deep(er) defect states.[59,63] Neglecting non-uniform doping [for the

time being] and taking the Kimerling interpretation, let's consider the reverse bias CV profile of Figure 24a to be representative of the inclusion of the deep-defect profile shown in Figure 24b. A simple quantification gives an interesting revelation. Figure 24b shows that at *ca.* E_v = 0.46 eV, or just below 1 kHz, the known deep-defect is fully responding. However, in the MS plot of Figure 24a, at frequencies <1 kHz the slope still gives some change in increasing reverse-bias. This seems to be representative of yet unknown, deeper defects ($e_p<v_{AC}$) being pulled to the quasiFermi-level to contribute. This thought is developed in the subsequent sections using a more targeted application of the above-summarized CF and CV measurements.

4.1.3 Experimental and photovoltaic performance

OPV cells were fabricated from P3HT (Reike Metals, 50k MW, 90-94% regioiregularity, <0.04% Ni / < 0.02% Zn / < 0.04% Br) and PCBM (NANO C, Inc.). Bulk heterjunction mixtures of 1:1 or 1:0 by weight (20-30 mg/ml) P3HT:PCBM were mixed with ortho-Dichlorobenze (Sigma-Alrich) and stirred at 45 ºC for at least 12 hours. Indium tin oxide (ITO; Delta Technologies) substrates were treated by consecutive sonications in: (i) isopropyl/acetone (50:50 v/v), (ii) detergent/deionized water, (iii) ethanol/methanol (50:50 v/v), and (iv) deionized water. The substrates were then blown dry and treated with air plasma. A ca. 30nm poly(ethylenedioxythiophene): poly(styrenesulfonic acid) (HC Stark) film was spin-coated onto the treated substrates and the casted films were annealed at 120 ºC for 10 min. The blend solutions were then filtered via plastic-syringe (note, this is known to affect the solution's wettability)[13] and a 0.22 µm PTFE filter (Sigma-Aldrich). The active layer was then spun at 400 to 600 rpm for 60 s onto the PEDOT covered substrates and slow-dried in a Petri dish. Lastly, a

ca. 1500 Å thick Al cathode was thermally evaporated at a rate < 5 Å/s under a 10^{-6} mBar vacuum.

Capacitance measurements were taken using a PARSTAT 2273 in the dark, at room temperature and in open air. Four averages per data-point and a three second delay between successive measurements were used to increase data-quality. A small-signal amplitude of 10 to 25 mV (rms) was used for linearity and the impedance magnitude (|Z|) was monitored to ensure proper model employment.[114] CF data was taken at a 0 V DC bias. To rule out oxygen induced artifacts during the longer low frequency measurements, a set of measurements was also conducted in nitrogen atmosphere – no differences were found. Further, the measurements were always conducted as CV, CF, and repeat CV in order to ensure no differences in the oxygen induced doping were seen during the data collection time.

Illuminated J-V data was generated at AM1.5 using an ELH quartzline lamp at 1 sun. The system was calibrated using a crystalline silicon photodiode coupled with a KG-5 filter. **Table 5** summarizes the photovoltaic performance plotted in **Figure 25**.

V_{oc} (V)	J_{sc} (mA/cm^2)	FF (%)	PCE (%)
0.54	10.90	55.80	3.30

Table 5: summary of photovoltaic performance parameters for a sample P3HT:PCBM device.

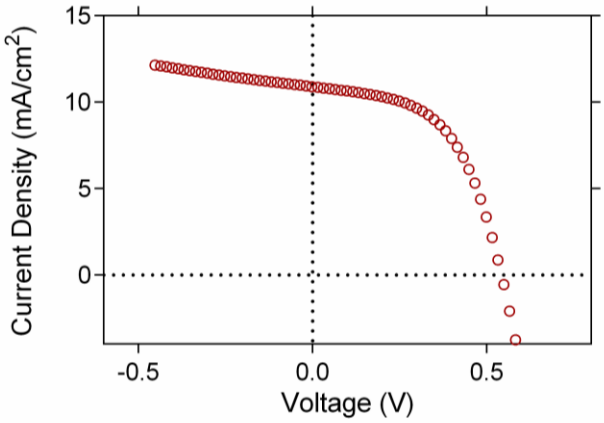

Figure 25: photovoltaic performance of the studied P3HT:PC_{60}BM BHJ cells.

4.1.4 Deeper defects: identification and characterization

Low frequency capacitance measurements: as an initial step towards identifying and characterizing this suspected distribution, I probe deeper into the energy-gap with low frequency capacitance measurements. The CF measurement is valid between the Fermi-level and mid-gap,[92,124] however, current CF data on P3HT:PCBM OPVs extends only to ca. 10 Hz (*ca.* 578 meV). Thus, I probe deeper towards the mid-gap with frequencies nearing 10 mHz (*ca.* 756 meV). Measurements at these frequencies proved difficult as the AC impedance becomes high and noise can dominate. To combat this, thicker devices (> 200 nm) were used. Thicker films seem counterintuitive as the geometric impedance is actually increased. However, the longer drying times of thicker films gives the phases more time to segregate across the vertical axis.[125] Thus, less shunt paths percolate, resulting in less leakage. Thicker devices have the added advantage of ensuring proper doping extraction from CV MS, which has recently been cautioned.[98] **Figure 26a** shows the resulting CF data normalized to geometric capacitance.

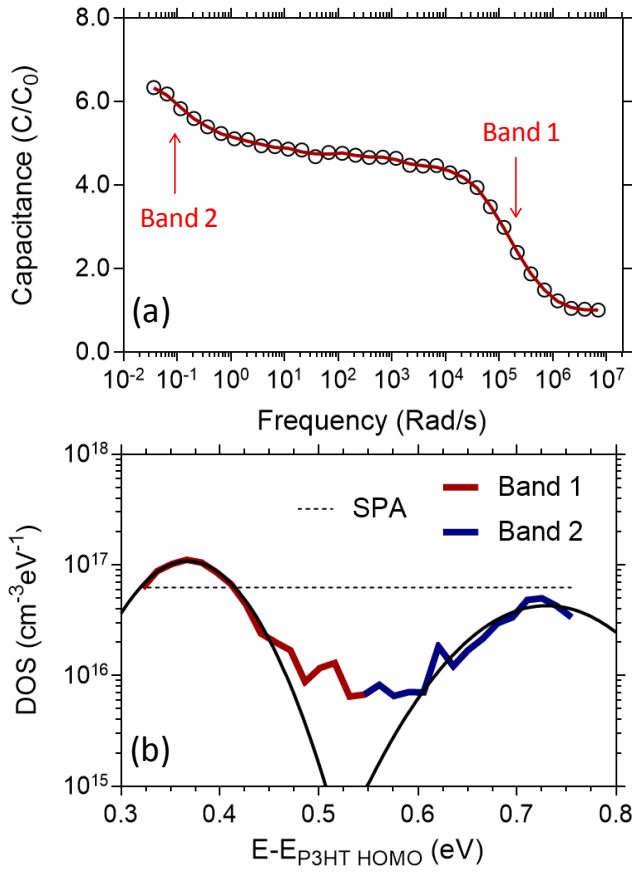

Figure 26: (a) CF spectra normalized to geometric capacitance (ca. 1.10 nF) showing two dominate regions of increasing capacitance. Red, solid line shows polynomial fit. (b) Resulting tDOS energy spectra showing two Gaussian defect bands as per the Walter *et al.* model. The dashed line shows the constant DOS calculated with the spatial abscissa (SPA) interpretation.

Initial information can be obtained through the derivation from the model of Cohen and Lang.[96] An estimation of the Debye length and concentration of measured trap states is given by Equations (24) and (25). In order to compare with the Walter *et al.* model, the constant trap profile obtained from Equation (23) was integrated between 300 and 800 meV (simply taken to be a rectangle). These results are summarized in **Table 6**; average ± standard error of the mean

(SEM) for four representative devices is shown. The distribution can be further resolved using the model of Walter *et al.* **Figure 26b** shows the energy spectra calculated by Equation (27). Before solving, data was cleaned using a polynomial averaging (solid, red line in Figure 26a). The resolved bands were then fit using a Gaussian form,

$$N_T(E_v) = \frac{N_T}{\sqrt{2\pi}\sigma} \exp\left[-\frac{(E_o - E_v)^2}{2\sigma^2}\right] \quad \textbf{(28)}$$

where N_T is the concentration of traps, E_0 the mean energy and σ the disorder parameter. Table 6 summarizes the parameter extraction; the average ± SEM for four representative devices is shown.

	Cohen and Lang model		**Walter *et al.* model**		
	L_D (nm)	N_T (cm^{-3})	N_T (cm^{-3})	E_0 (eV)	σ (meV)
Band 1	--	--	1.70 ± 0.40 x10^{16}	0.33 ± 0.01	42.3 ± 3.30
Band 2	--	--	0.60 ± 0.20 x10^{16}	0.69 ± 0.02	48.2 ± 8.50
Total	13.1 ± 2.30	3.12 ± 0.67 x10^{16}	2.30 ± 0.60 x10^{16}	--	--

Table 6: summary of calculated parameters from CF data; average ± SEM shown.

Two distinct bands are seen in the resulting spectrum: one in the high (>1 kHz) frequencies and one in the low (<1 Hz) frequencies. The shallower, high-frequency band correlates well to the data presented in Figure 24 and FTSC (E_{oFTSC} = 0.35 eV)[75], CF (E_{oAS} = 0.36 – 0.38 eV) [21,38] and Poole-Frenkel conduction modeling (PFCM) (E_{oPFCM} = 0.30 – 0.50 eV)[76] data

presented in the literature. Any deviation in the mean energy stems from the choice of v_o while deviations in concentration result from the growth-rate dependence.[21] v_o, the attempt-to-escape frequency, is a characteristic parameter which represents the prefactor of trap emission. It is especially important for finding the exact depth of the measured defect-bands in the Water *et al.* model. Previous admittance spectroscopy reports have used a v_o of 10^{12}-10^{13} s^{-1} as an estimation stemming from inorganic materials.[21,38] However, a more recent report has called this value into question, citing an attempt-to-escape frequency of 33.42 s^{-1}.[79] The first (10^{12} -10^{13} s^{-1}) is slightly higher than and the latter significantly lower than values of 10^{7}-10^{9} s^{-1}, which have been extracted from poly(*p*-phenylene vinylene (PPV) based organic cells.[61,79-81] To comment on this, I use information from the freeze out frequencies and doping levels of our devices.

First, high frequency CF data (Figure 26) is examined. It can be seen that, for this particular device, at *ca.* 800 kHz the freeze out condition is reached – which corresponds to the demarcation energy reaching the Fermi-level. Freeze out frequencies ranging from 800 kHz to 1.5 MHz were seen in our devices. Next, high frequency CV with Mott-Schottky analysis is used to find the density of mobile charges and solve for $E_F - E_{P3HT\ Valance}$ by:

$$E_F - E_{P3HT\ HOMO} = k_B T \ln\left(\frac{N_V}{p}\right). \quad \textbf{(29)}$$

Values for N_v ranging from 10^{19} to 10^{21} cm^{-3} have been used in the literature.[126-128] Thus, v_o is approximated to be between $1x10^{9}$ and $5x10^{10}$ s^{-1} depending on the choice of N_v. In this report,

ν_o = 5x10^{10} s^{-1} will be used. A more accurate treatment of the attempt-to-escape frequency is given by:

$$\nu_o = \beta_p N_V, \quad \textbf{(30)}$$

where β_p is the capture coefficient of the trap.[92] Note that the parameter is dependent on temperature as well as the characteristics of the trap being probed.[62] Thus, more in-depth work is needed to find the exact attempt-to-escape-frequency(ies). This will be revisited in the subsequent chapter. In the meantime, I expect the above to give a reasonable estimate for the work at hand.

The deeper, low-frequency band represents a previously unknown defect distribution – as predicted by the above-discussed CV interpretation. This band has a mean energy of 0.68 eV above the highest occupied molecular orbital (HOMO), *ca.* 0.34 eV deeper in the gap than known Band 1. Although this deeper band is smaller in amplitude, it is still on the order of 5x10^{16} cm^{-3} eV^{-1}, indicating it may play a significant role in altering OPV performance. This is especially true considering the deeper an energetic defect resides, the more strongly it can trap carriers. In a disordered material, trap states can contribute to current through thermally activated tunneling and hopping.[9] However, at sufficiently deep levels charge transfer is cut-off and the states are static.[9] The strongly trapped charge may then act as a monomolecular recombination center, a charged point site or both. Good agreement in the total concentration of measured traps between the two models is clearly seen. No significant statistical difference

(p-value>0.05) was found in the displayed averages. To highlight reproducibility and variation, **Figure 27** shows repetitions for the CF generated tDOS.

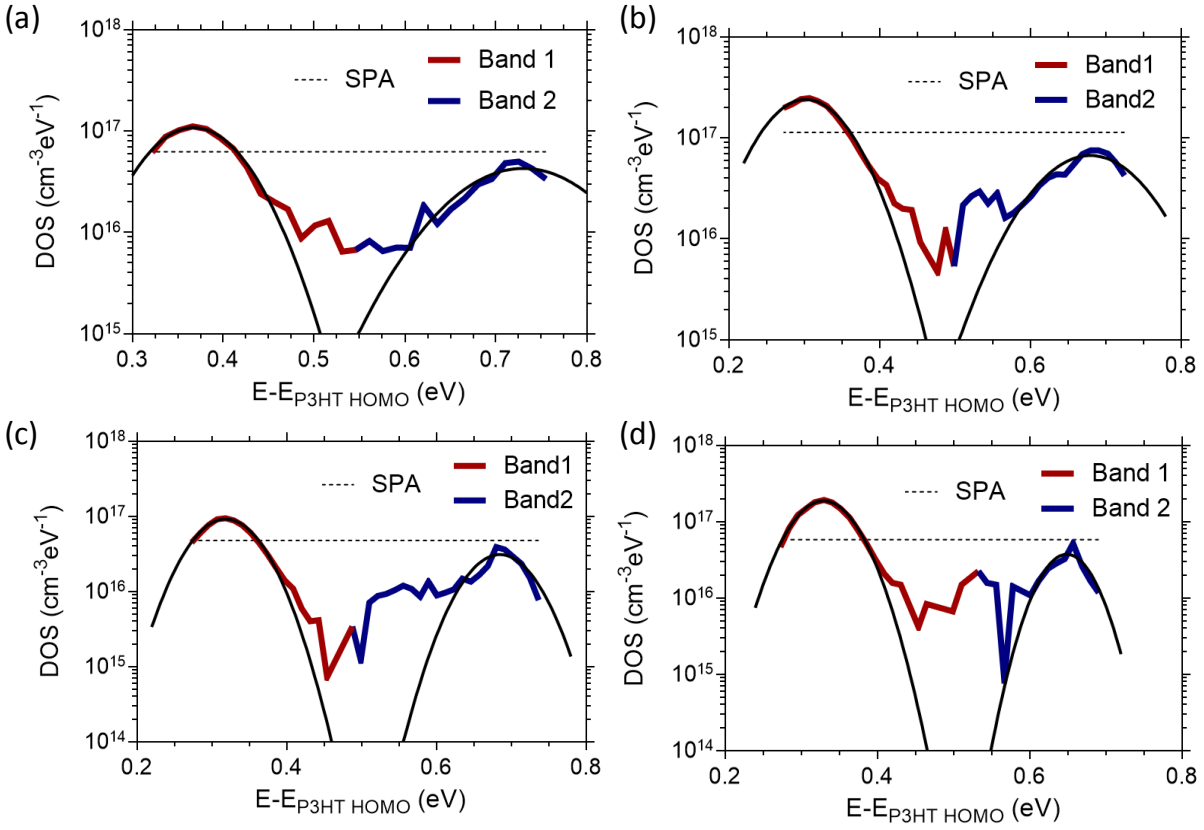

Figure 27: repetitions of low-frequency CF measurements. The DOS spectra are shown. The parameters of IDs (a)-(d) are summarized in Table 7.

Each device showed the distinct presence of two deep-defect bands, one in high frequencies and one in low frequencies. **Table 7** summarizes the Gaussian fit parameters for each band. Thickness values were obtained by geometric capacitance measurements – the devices were depleted by a large reverse DC bias (≥ -5 VDC) and a high frequency (≥ 500 kHz) was used to ensure only a dielectric response.

ID	Thick (nm)	Band	A (cm^{-3} eV^{-1})	E_0 (eV)	σ (meV)
(a)	300	1	10.8 x10^{16}	0.36	47.5
		2	2.99 x10^{16}	0.73	41.0
(b)	204	1	24.0 x10^{16}	0.30	48.2
		2	6.70 x10^{16}	0.68	60.0
(c)	266	1	9.20 x10^{16}	0.32	38.5
		2	3.00 x10^{16}	0.68	41.0
(d)	235	1	18.8 x10^{16}	0.33	35.2
		2	3.80 x10^{16}	0.65	27.6

Table 7: summary of Gaussian fit parameters for the tDOS plots of Figure 27.

High frequency point-by-point CV: in order to test if the newly discovered deep-defect distribution accounts for the slope change in the lower frequency CV data, one might intuitively measure the MS profile at 10 mHz in search of a straight plot. This experiment, however, was dominated by noise, making it difficult to ascertain meaningful results. Thus, I next turn to a point-by-point differential of high frequency CV measurements in an attempt to make correlations between Equation (28) and the tDOS profile of Figure 26b.

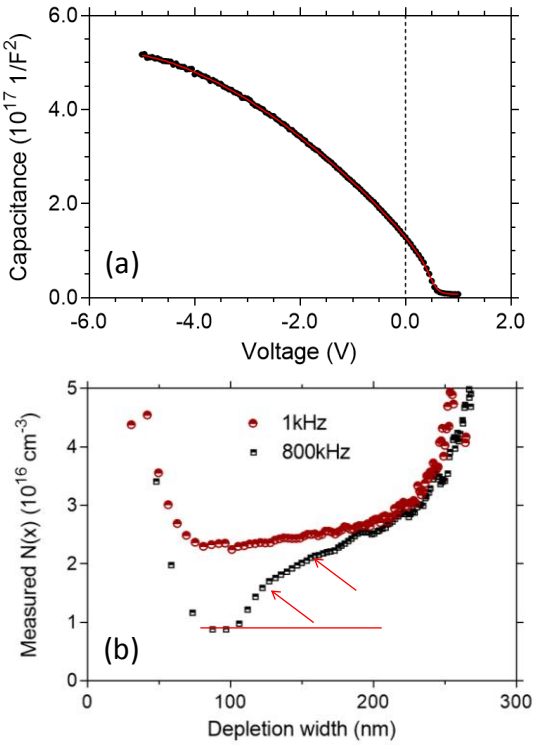

Figure 28: (a) high frequency CV data shown in Mott-Schottky form. Red, solid line shows polynomial fit. (b) Measured N(x) versus W for CV of (a) for a high and moderate frequency.

CV data taken at 800 kHz from -5 to +1 V_{DC} is displayed in Figure 28a. The MS form shows the expected rolling slope. **Figure 28b** shows the calculated *depth profile*, which I believe is best represented by the Kimerling model of Equation (28). To be thorough, Cohen and Lang have also described this dynamic DC response and their interpretation has already been employed within the organic community.[93,95] However, our data did not match that described in the cited work and better applicability of the Kimerling formalism was found. The highest possible frequency before complete freeze out was used to ensure case 2 of the Kimering theory was invoked and that $\langle x \rangle = W_d$.[62,63]

In Figure 28b, a decrease followed by a minimum and gradual increase in N(x) is seen. The minimum point corresponds to a voltage very near V_{bi}, where the bands are nearly flat and, because a high frequency was employed, only p responds. At higher forward-bias, the depletion width reduces, carriers are injected and a chemical capacitance begins to dominate.[89,98,129] At increasing reverse-bias, the depletion width is increased, bands are bent and the possible contributions of traps states are seen.

To begin, let us neglect the possibility of a non-uniform doping profile and consider the Gaussian defects of Figure 26b as they are pulled to the quasiFermi-level to contribute to the CV measurement. Starting from near the flat-band condition, a sharp increase in N(x) would first be seen with increasing reverse bias. As the Gaussian center is passed, defect states are still included, but at a slower rate, causing an inflection in N(x). As the next Gaussian is pulled, a second inflection would be found, and so on. In Figure 28b, red arrows highlight those inflections which I expect correspond to dominate Gaussian distributions. By subtracting the values of N(x) at the inflections to the left and right of a suspected distribution, the total defects of that band is found. Assuming homogeneous doping, these values should correlate to those found by CF, while deviations may be indicative of a non-uniform doping profile. Indeed, good agreement between the magnitude of the CV distributions (Figure 28b red arrows) and the CF (Figure 26b) defect bands is found. For this particular cell, CV gave the Band 1 concentration to be 8.81×10^{15} cm^{-3} and Band 2 to be 3.67×10^{15} cm^{-3}. This compares to CF values of 9.12×10^{15} cm^{-3} (high frequency band) and 3.07×10^{15} cm^{-3} (low frequency band) respectfully. Further, a lower frequency (1 kHz) analysis is also included in Fig. 3b. At 1 kHz the first defect distribution is

already responding and, in accordance with the above theory, the profile is pivoting upwards. The trend will limit towards a straight line (i.e. with a low enough measurement frequency) which represents the mobile charges plus total defect states.[62] The pivot and expected straight-line limit can be seen near $2.7x10^{16}$ cm^{-3} in this particular device. The difference between the 1kHz profile and straight limit is about $3\text{-}4x10^{15}$ cm^{-3}, the value of the low-frequency, deeper distribution not yet included in low-bias 1kHz measurement. This again supports the existence of a distribution deeper in the gap and, because the depth profile of inhomogeneous doping would be independent of frequency, further rules out the possibility of non-uniform doping. Repetitions for the high frequency CV measurement are displayed in **Figure 29**. For each ID (a)-(d) the raw CV data is displayed in the left column, while the *depth* profiles are shown on the right. **Table 8** summarizes the trap concentrations.

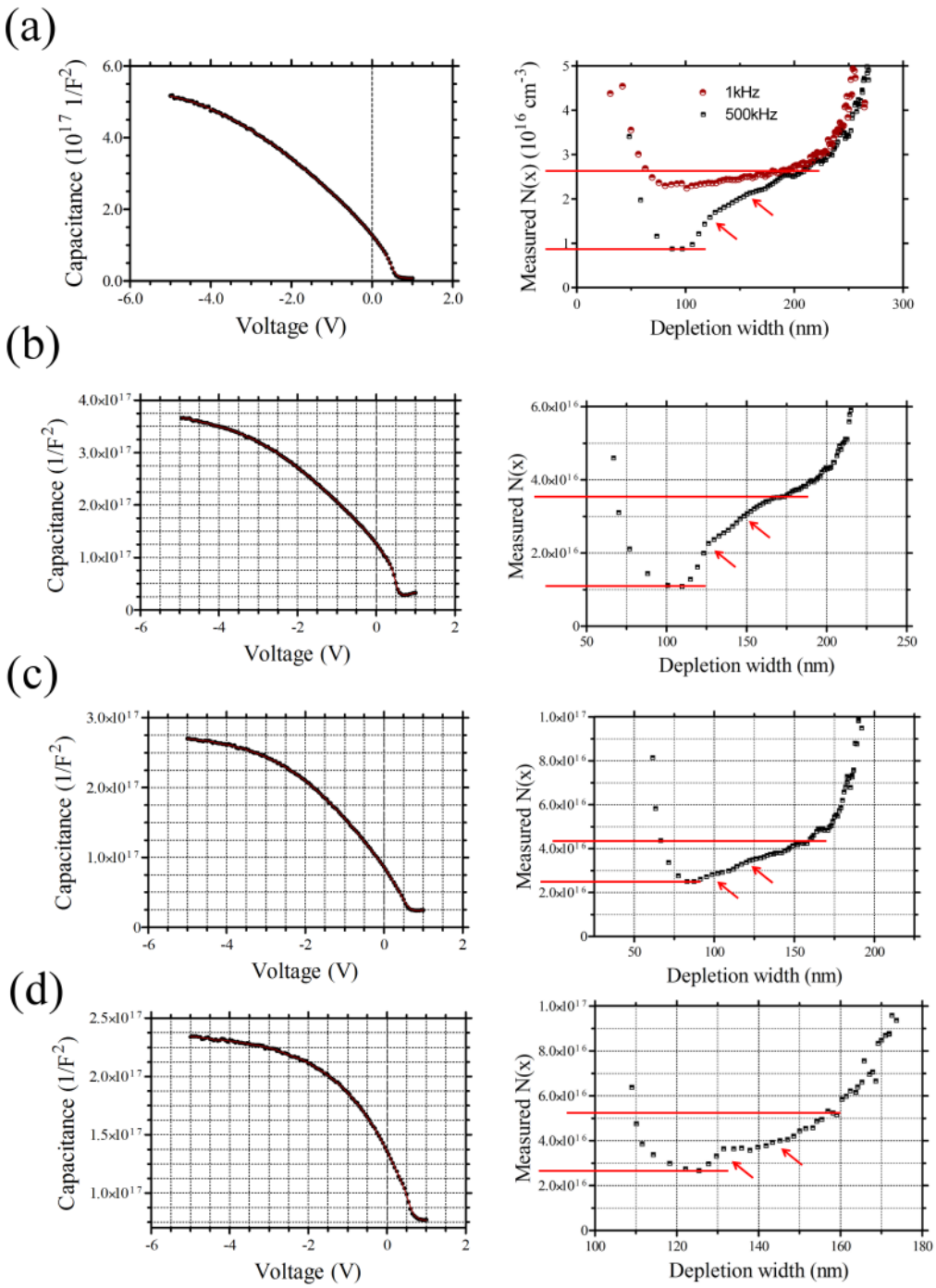

Figure 29: repetitions of high-frequency CV analysis from +1 to -5 V_{DC}. CV data (left column) was solved by Equation (16) to give the profile on the right.

ID	Frequency (kHz)	Band	N_T (cm^{-3})
(a)	800	1	$8.80x10^{15}$
		2	$3.10x10^{15}$
(b)	700	1	$1.50\ x10^{16}$
		2	$8.00\ x10^{15}$
(c)	700	1	$8.50\ x10^{15}$
		2	$5.90\ x10^{15}$
(d)	500	1	$1.40\ x10^{16}$
		2	$3.60\ x10^{15}$

Table 8: summary of band amplitudes for CV profiles of IDs (a)-(d) shown in Figure 29.

4.1.5 Polymer only diode and dark current modeling

To give indication as to the spatial location of these defects, a set of experiments was conducted to repeat the above measurements again on 1:1 P3HT:PCBM OPVs as well as 1:0 P3HT only diodes with both Al and Ca\Al cathodes. **Table 9** summarizes the results; average ± SEM is shown for three representative sets. Unpaired t-tests showed no significant statistical differences (p-value>0.05) in any 1:1 to 1:0 parameter comparison. This, coupled with data showing no difference in trap parameters between devices with an Al cathode and those with a Ca\Al cathode, strongly indicates the measured levels are belonging to the polymer bulk. Further, because of the prominent decrease in the MS slope with deeper reverse bias (i.e. increase in measured N), the traps are expected to be acceptor-like.[61]

	A (cm^{-3} ev^{-1})	E_o (eV)	σ (meV)
1:1 Band 1	18.0 ± 2.50 $x10^{16}$	0.31 ± 0.004	40.3 ± 3.50
1:0 Band 1	15.0 ± 2.80 $x10^{16}$	0.32 ± 0.005	33.3 ± 1.10
1:1 Band 2	3.10 ± 0.30 $x10^{16}$	0.66 ± 0.003	41.1 ± 7.40
1:0 Band 2	3.30 ± 0.40 $x10^{16}$	0.65 ± 0.007	44.7 ± 1.60
	p (cm^{-3})	**N_T Capacitance (cm^{-3})**	**N_T Dark IV (cm^{-3})**
1:1	3.30 ± 1.20 $x10^{16}$	4.90 ± 1.10 $x10^{16}$	n/a
1:0	2.30 ± 0.84 $x10^{16}$	4.00 ± 1.30 $x10^{16}$	4.70 ± 0.53 $x10^{16}$

Table 9: summary of tDOS characteristic parameters for 1:1 and 1:0 devices.

As seen in Table 9, dark-current modeling measurements were also conducted to generally verify the capacitance results. The dark current of a basic polymer diode is often described as space charge limited.[55,130,131] **Figure 30** shows the dark IV of a representative ITO\P3HT\Al diode. In the ln-ln plot, three main regions prevail: (i) ohmic in low voltages, (ii) trap controlled in intermediate voltages and (iii) trap free at high voltages.[55,130] The high voltage region is governed by $J_{TF} = 9/8\epsilon\mu V^2/L^3$ (solid line in Figure 30), where $J \alpha V^2$ (Figure 30 insert).[55] By examining the voltage at which current switches from trap controlled to trap free (V_{TF}), the total defect states can be estimated by $N_T=2\epsilon_s V_{TFL}/(qt^2)$.[132] The concentration estimated by dark IV agrees well with that determined via capacitance, substantiating the general capacitance measurement.

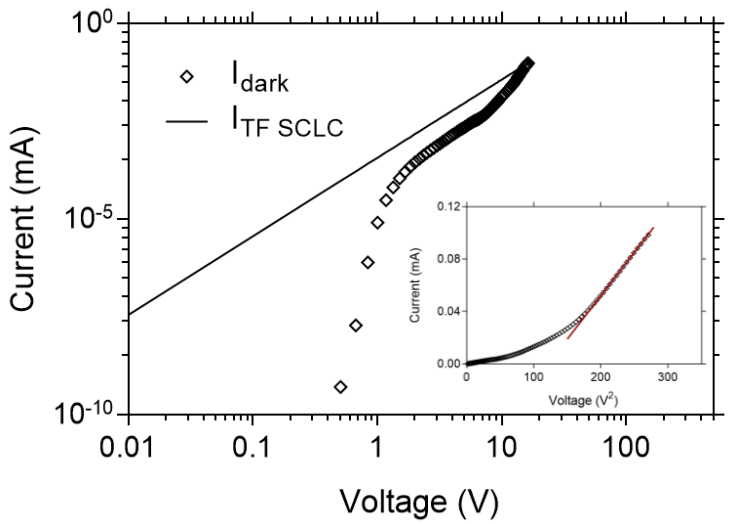

Figure 30: dark current versus voltage for P3HT diode. The solid line represent the trap-free model (μ=2x10^{-4} cm^2/V-s). The insert shows dark current versus voltage squared.

4.1.6 Project conclusion

Further elucidations into the capacitive behavior of P3HT:PCBM based photovoltaic cells were presented. A background of CV/CF analysis was given and evidence indicating the presence of a yet unknown deep-defect distribution was highlighted. Low frequency CF measurements were then undertaken to identify and characterize this deep band. The model of Cohen and Lang was used to determine the Debye length as well as the measured trap concentration. The formalism of Walter et al. gave good corroboration to the total concentration and further resolved the tDOS energy spectrum – directly revealing the presence of the predicted distribution. This new defect was then reproduced using the Kimerling interpretation of high-frequency CV measurements. Good correlation between CV and CF data confirms the presence of the deep defect and, especially when coupled with dark-current modeling data, shows no spatial variations in the doping profile. A comparison of PCBM

containing devices to that of polymer only diodes with different cathodes strongly indicates the measured defects to be acceptor-like traps belonging to the polymer bulk. The findings presented here are important for the understanding and optimization of organic solar cells and the presented methods are suspected to be generally applicable to other OPV material sets.

5 CHAPTER V: THE DYNAMICS OF TRAP EMISSION IN OPV DEVICES

In the previous chapter's work, it became clear that the prefactor of trap emission – also referred to as 'the attempt-to-escape frequency' – is a critical parameter needed if one is to accurately describe the dynamics of trap occupancy and bandgap tDOS. This chapter details temperature dependent capacitance versus frequency measurements which were undertaken to characterization this prefactor in OPV devices. Several polymer systems will be discussed. At the time of this dissertation submission, the following work is currently being prepared for publication.

5.1.1 Project introduction and motivation

The attempt-to-escape frequency is a characteristic semiconductor parameter which helps to define the kinetics of trap occupancy. This parameter is enumerated in inverse seconds (or rad/s) and gives the maximum rate of change for trap emission cycles. The parameter has been briefly discussed above and, in reference to capacitance based measurements, it is clear that it must be known if one is to accurately determine the exact energetic location(s) of the measured traps. Expanding further, one finds the attempt-to-escape frequency is also at the heart of any measurement or model which employs detrapping dynamics.

Of course, this prefactor is needed for capacitance based measurements – both admittance spectroscopy as well as deep-level transient spectroscopy.[61,92] The parameter also

finds employment in charge hoping models. For example, the Marcus theory of charge transfer is often applied to describe the transfer rate between two organic sites (*i* to *j*): [133]

$$\nu_{ij} = \frac{\mathrm{I_{ij}}^2}{\hbar}\sqrt{\frac{\pi}{\lambda \mathrm{kT}}}\exp\left[-\frac{(\Delta G_0 + \lambda)^2}{4\lambda kT}\right] \quad \textbf{(31)}$$

The Miller-Abraham rate equation is then used to determine the charge-carrier tunneling rate for phonon-assisted hopping: [134,135]

$$\nu_{ij} = \nu_0 \exp\left[-2\acute{\alpha} r_{ij} - \frac{|E_j - E_i| + (E_j - E_i)}{2kT}\right] \quad \textbf{(32)}$$

which is commonly simplified to a functional form $\nu=\nu_0\exp[-2\acute{\alpha}r]$.[136,137] It is quite obvious that ν_0 must be well known if this type of model is to be accurately applied. The attempt-to-escape frequency is also needed for the Braun model for the dissociation of charge transfer states (Equation (33)), which is commonly applied to OPV devices. [31,138,139]

$$K_1 = \frac{\omega_0 \exp\left(-\frac{E_B}{kT}\right) f(F)}{K_R + \omega_0 \exp\left(-\frac{E_B}{kT}\right) f(F)} \quad \textbf{(33)}$$

Several other derived equations employing this parameter can also be found. For example, the zero field, infinite temperature limit mobility, [136,140]

$$\mu_0 = \frac{qa^2\nu_0}{\sigma}\exp\left[\frac{-2a}{L}\right] \quad \textbf{(34)}$$

or the generation-recombination based reverse bias saturation current,[31]

$$J_0 = AeN_R kT\omega_0 \exp\left(-\frac{E}{kT}\right) \quad \textbf{(35)}$$

The attempt-to-escape frequency also finds itself in TSC based measuremtns.[24,75] Clearly, the parameter has a wide range of employment and its accurate characterization is essential if trapping dynamics are to be properly described.

Though the attempt-to-escape frequency is an important parameter, little work has been done to universally quantify it in OPV devices. To date, a majority of studies employing this parameter have borrowed values (10^{12}–10^{14} s^{-1}) from the inorganic literature,[13,21,35,38,136,140,141] or simply left the parameter as an unknown.[86] Few works have actually measured ν_0. As mentioned above, this parameter has been investigated in PPV based solar cells and Schottky diodes, both finding values between 10^7 and 10^8 s^{-1}.[61,80] A single report has found the attempt-to-escape frequency in Pentacene thin-films to be $5x10^{12}$ s^{-1} and another has found 10^5 s^{-1} for Sexithiophene based transistors.[142,143] As mentioned in Chapter I, a more recent report has studied the attempt-to-escape frequency in P3HT-fullerene photovoltaic devices, with a surprising result – 33.4 s^{-1}.[79] Clearly a huge range of values are currently being employed – 10^1 to 10^{14} Hz, indicating each organic material may have a unique value or there is some ambiguity

in the measurement. Thus, I aim to revisit the prefactor in P3HT based devices and extend to include the results for the newer, higher efficiency OPV polymers.

5.1.2 Theoretical background

A theoretical understanding of the attempt-to-escape frequency is readily obtained by considering the thermal release rate of charges trapped within a semiconductor bandgap. Neglecting degeneracy, hole emission is defined by Equation (18). Clearly, this is an Arrhenius equation in which the emission rate is heavily dependent on the trap depth (activation energy), the sample temperature and the pre-exponential factor - $N_c\langle V_{th}\rangle\sigma_n$. It is this prefactor that is commonly known as 'the attempt-to-escape frequency' (ν_0).[92,93,111] Linearizing Equation (18) yields,

$$\ln(e_p) = -\frac{E_A}{k_B T} + \ln(\nu_0) \qquad \textbf{(36)}$$

where a classic Arrhenius plot of the $\ln(e_n)$ versus 1/T gives a straight line with a slope that defines the trap activation energy and an intercept that defines the attempt-to-escape frequency.[92] Thus, by monitoring the change in trap emission with a change in sample temperature, the attempt-to-escape frequency can be obtained. This treatment assumes the pre-exponential factor itself to be independent of temperature. However, N_c is known to vary $\propto T^{3/2}$ while $\langle V_{th}\rangle$ varies $\propto T^{1/2}$ – giving an inherent temperature dependence to ν_0.[62] To account for this, the prefactor is sometimes written as 'ΥT^2' where $\Upsilon = N_c\langle V_{th}\rangle\sigma_n T^{-2}$ and then the $\ln(e_n/T^2)$ will be plotted versus 1/T to determine its value.[62,81] Of course, the T^2 term is dominated by T

term within the exponential and a large difference in the calculated attempt-to-escape frequency is typically not seen.[92] Thus, this temperature dependence is often neglected. Nonetheless, the results will be evaluated both ways herein.

The change in trap emission with a change in sample temperature can be readily tracked through capacitance measurements. Such measurements have been vastly discussed above. Simply put, as the frequency is swept from high (few or no bandgap states responding) to low (most or all bandgap states responding) 'steps' in the capacitance will be seen. Corresponding peaks in the differential –FdC/dF are then obtained and will display an Arrhenius behavior with changing temperature.[62,92] Because of the inherent demarcation of the applied AC signal, the frequency of these differential peaks represents the emission rate of the responding band. Thus, by plotting the frequency at which the peak occurs versus 1/T, the attempt-to-escape frequency can be readily found through Equation (36) and the capture cross section calculated *via* $\sigma_n = \nu_o/N_c\langle V_{th}\rangle$.[62,92] The subsequent sections detail the application of this theory to several polymer-based OPV devices.

5.1.3 Experimental and photovoltaic performance

Temperature dependent capacitance versus frequency (TCF) measurements were carried out on the custom built setup pictured in **Figure 31.** Three different LCRs were explored to ensure high data quality. (i) A QuadTech 7600 (10 HZ – 2 MHz; 0.05% basic accuracy), (ii) a HIOKI IM3533-01 (1 mHz – 200 kHZ; 0.05% basic accuracy) and (ii) a PARSTAT 2273 (10 µHz to 1 MHz; <0.75% basic accuracy). Though the LCRs have a rated measurement range as stated, the

usable range was often limited by device under test. Thus, data at the extremes – high frequency data where possible inductance effects were seen and low frequency data where leakage causes high dissipation values (D>1; though D values as high 10 are typically acceptable[62,110]) – were neglected. A continuous flow liquid nitrogen cryostat, controlled by a Lakeshore 331 temperature controller, was used to vary the sample temperature between 100 and 400 K. Two platinum resistance temperature detectors (RTDs) contained within the cryostat head and one platinum RTD mounted on the sample surface were used to accurately track the cell temperature. The right hand panel of Figure 31 shows an OPV devices mounted for test. The sample sits directly atop the copper cryostat head. Cryogenic rated grease, which solidifies at low temperatures, was used to improve thermal conductivity between the head and sample substrate. The surface mounted RTD is clearly seen on the right. A simple wire probe, which is mimicked by the RTD to ensure an accurate temperature measurement, is connected to the aluminum cathode. The probe wires are wrapped around the side of the cryo-head and varnished in place to ensure they cooled to the setpoint temperature. A silver, clamp-like probe makes connection to the ITO anode and, again, the connecting wires are wrapped and varnished to the cryo-head.

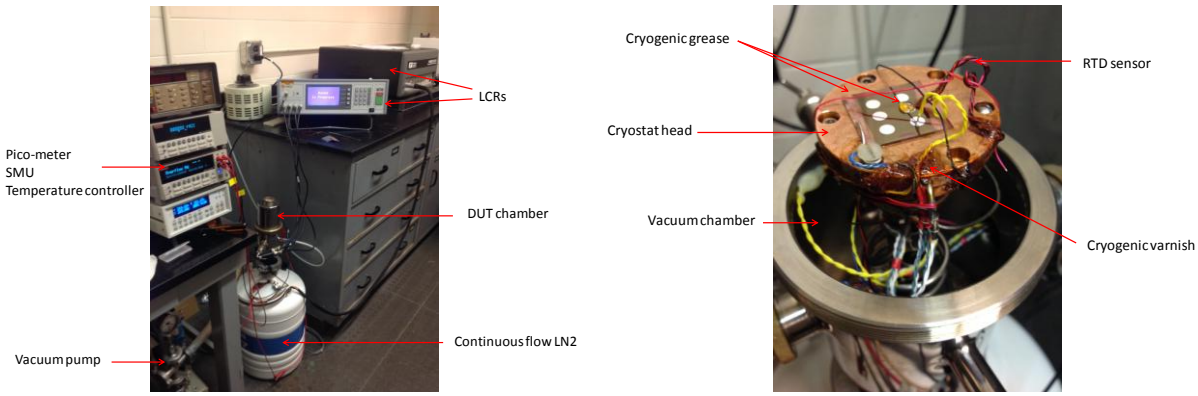

Figure 31: experiment setup for temperature dependent capacitance-frequency measurements.

The TCF system was benchmarked with hydrogenated amorphous silicon (a-Si:H) solar cells, which are well known to have an attempt-to-escape frequency in the range of $1x10^{11}$-$1x10^{13}$ Hz.[113,144-146] Sample calibration data from the system is shown in **Figure 32**. The average measured attempt-to-escape frequency was found to be $1.6x10^{12}$ Hz – well within the expected range. This shows the validity of the experimental setup and the results presented herein.

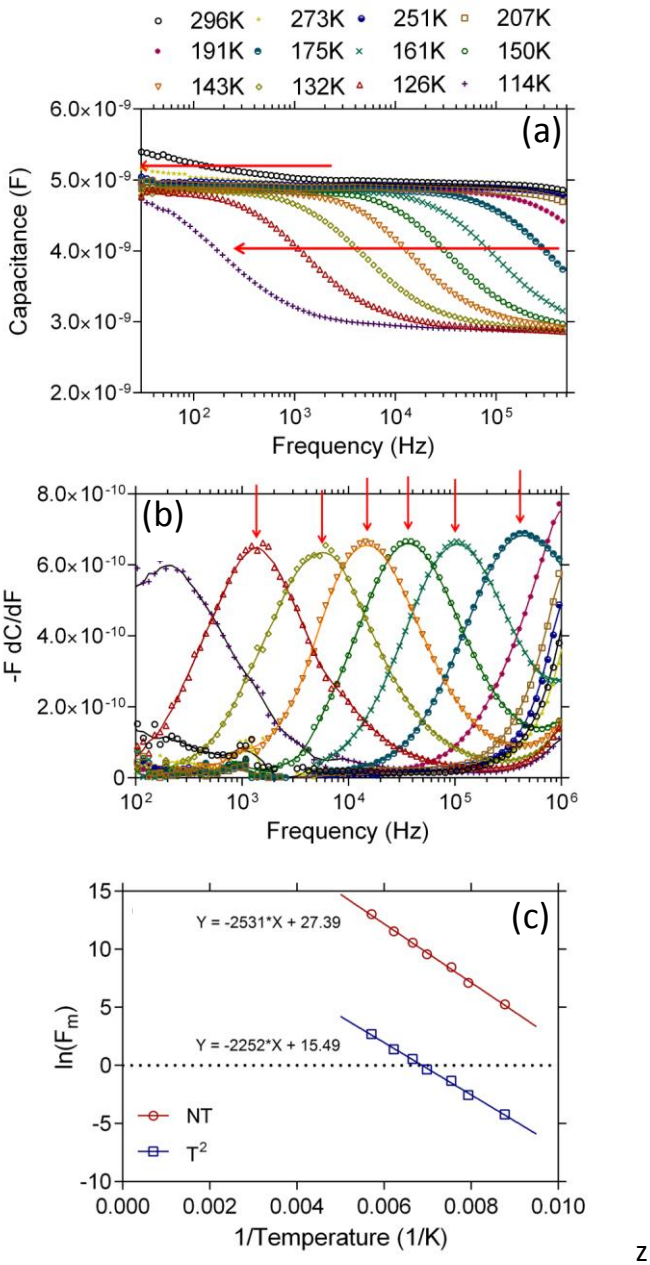

Figure 32: (a) capacitance versus frequency as a function of temperature for a sample a-Si:H solar device. The red arrows indicate the Arrhenius shift of the trap states with lowering temperatures. (b) –F dC/dF differential. Arrows indicate emission peaks. (c) Arrhenius plot of the –F dC/dF peak frequencies versus 1/T.

Three different polymer based systems were tested: (i) P3HT, (ii) PTB7 and (iii) PCDTBT. The P3HT based cells were fabricated as discussed in section 4.1.3. Photovoltaic activity (illuminated J-V) was tested at a simulated AM1.5 using an ELH quartzline lamp. The system was calibrated using a crystalline silicon photodiode coupled with a KG-5 filter. **Table 10** summarizes the photovoltaic performance plotted in **Figure 33** (both before and after the cryogenic experiment is shown). As will be discussed in the subsequent section, it was necessary to *stabilize* the P3HT based cells to the vacuum environment. This was done by either a short (<10 min) 375 K anneal or a long (>20 Hr) 325 K anneal. JV data for both stabilization methods is shown in Figure 33. It should be noted that *after* means not only after the thermal stabilization but also after the cryogenic experiment. Interestingly, the longer, 325 K anneals produced better photovoltaic performance. The reason for this is not yet known, but I suspect it may be related to high diffusion of the aluminum at the higher temperature anneal. Studies are currently underway to explain this difference.

	V_{oc} (V)	J_{sc} (mA/cm^2)	FF (%)	PCE (%)
Before (325K)	0.55	10.1	44.0	2.40
After (325K)	0.60	11.5	46.0	3.20
Before (375K)	0.55	10.1	45.0	2.50
After (375K	0.59	10.2	48.5	2.90

Table 10: summary of photovoltaic performance parameters for a sample P3HT:PCBM device.

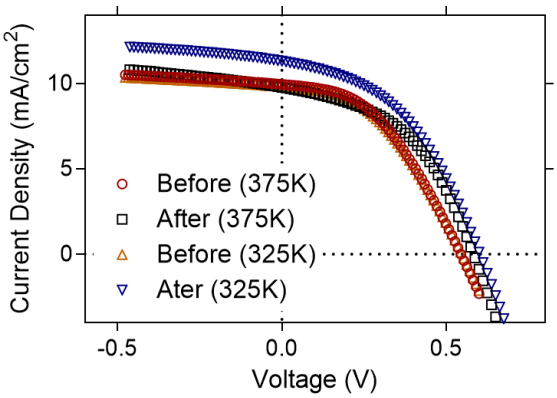

Figure 33: illuminated JV characteristics for P3HT:$PC_{60}BM$ based solar cell both before and after the TCF experiment.

PTB7 devices were fabricated as follows. Bulk heterojunction mixtures of 1:1.5 by weight (1 0mg/ml) PTB7 (1-material) to $PC_{70}BM$ (NANO C, Inc.) were mixed with ortho-Dichlorobenze (97%):1,8-Diiodooctane (3%) and stirred at 45ºC for at least 12 hours. Indium tin oxide (ITO; Delta Technologies) substrates were treated by consecutive sonications in: (i) isopropyl/acetone (50:50 v/v), (ii) detergent/deionized water, (iii) ethanol/methanol (50:50 v/v), and (iv) deionized water. The substrates were then blown dry and treated with air plasma. A ca. 40nm poly(ethylenedioxythiophene): poly(styrenesulfonic acid) (HC Stark) film was spin-coated onto the treated substrates and the casted films were annealed at 150 ºC for 30 min. The blend solutions were then filtered via a non-lubricated plastic syringe and a 0.22 µm PTFE filter. The active layer was then spun at 1,000 rpm for 60 s onto the PEDOT covered substrates and slow-dried in a Petri dish. Lastly, a *ca.* 20 nm/100 nm thick Ca/Al cathode was thermally evaporated at a rate < 10 Å/s under a 10^{-6} mBar vacuum. The photovoltaic performance is shown in **Figure 34** and summarized by **Table 11**. These devices did not need to be stabilized to

the vacuum environment; hence only one set of data before and after the cryogenic experiment is shown.

	V_{oc} (V)	J_{sc} (mA/cm^2)	FF (%)	PCE (%)
Before	0.77	18.1	66.0	9.10%
After	0.77	18.0	66.2	9.20%

Table 11: summary of photovoltaic performance parameters for a sample PTB7:$PC_{70}BM$ device.

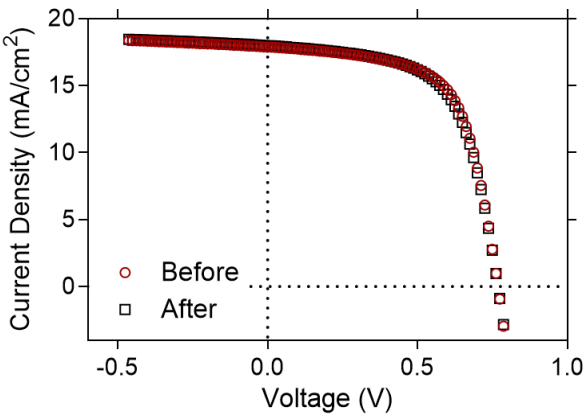

Figure 34: illuminated JV characteristics for PTB7:$PC_{70}BM$ based solar cells both before and after the TCF experiment.

PCDTBT devices were fabricated as follows. Bulk heterojunction mixtures of 1:4 by weight (7 mg/ml) PCDTBT (1-material) to $PC_{70}BM$ (NANO C, Inc.) were mixed with ortho-Dichlorobenze and stirred at 45 ºC for at least 12 hours. Indium tin oxide (ITO; Delta Technologies) substrates were treated by consecutive sonications in: (i) isopropyl/acetone (50:50 v/v), (ii) detergent/deionized water, (iii) ethanol/methanol (50:50 v/v), and (iv) deionized water. The

substrates were then blown dry and treated with air plasma. A ca. 40nm poly(ethylenedioxythiophene): poly(styrenesulfonic acid) (HC Stark) film was spin-coated onto the treated substrates and the casted films were annealed at 150 ºC for 30 min. The blend solutions were then filtered via a non-lubricated plastic syringe (as to not introduction silicone contamination)[13] and a 0.22 µm PTFE filter. The active layer was then spun at 1,000 rpm for 60 s onto the PEDOT covered substrates and slow-dried in a Petri dish. Lastly, a *ca.* 20 nm/100 nm thick Ca/Al cathode was thermally evaporated at a rate < 10 Å/s under a 10^{-6} mBar vacuum. The photovoltaic performance is shown in **Figure 35** and summarized by **Table 12**. These devices did not need to be stabilized to the vacuum environment; hence only one set of data is shown.

	V_{oc} (V)	J_{sc} (mA/cm^2)	FF (%)	PCE (%)
Before	0.84	10.0	36.1	3.00
After	0.83	9.70	37.4	3.10

Table 12: summary of photovoltaic performance parameters for a sample PCDTBT:$PC_{70}BM$ device

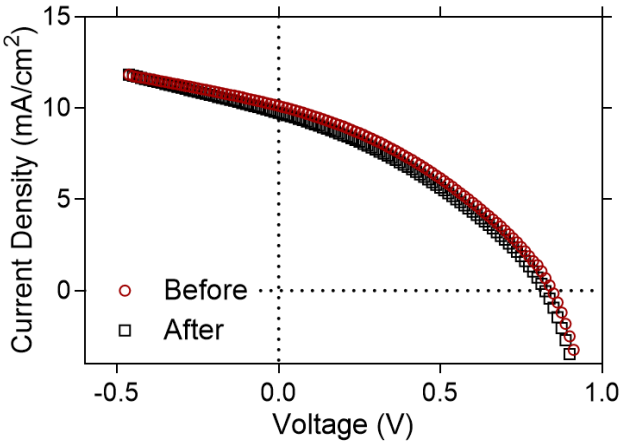

Figure 35: illuminated JV characteristics for PCDTBT:$PC_{70}BM$ based solar cells both before and after the TCF experiment.

5.1.4 The prefactor of trap emission in OPV devices

To begin, let us look at the results for P3HT:PCBM based OPV devices. As mentioned above, these devices needed to be 'stabilized' to the vacuum environment of the cryostat. The need for this stabilization was found empirically over the course of the long (4-6 hours) TCF measurements. Data taken at 300 K before the cold temperature experiments would not line up to 300 K data taken after. This change was at first attributed to a long photocapacitance decay, an environmental change throughout the course of the experiment or a physical, permanent change in the device at cold temperatures. To sort out this stabilization issue, the capacitance of the OPV devices contained within cryostat vacuum was monitored as a function of time.

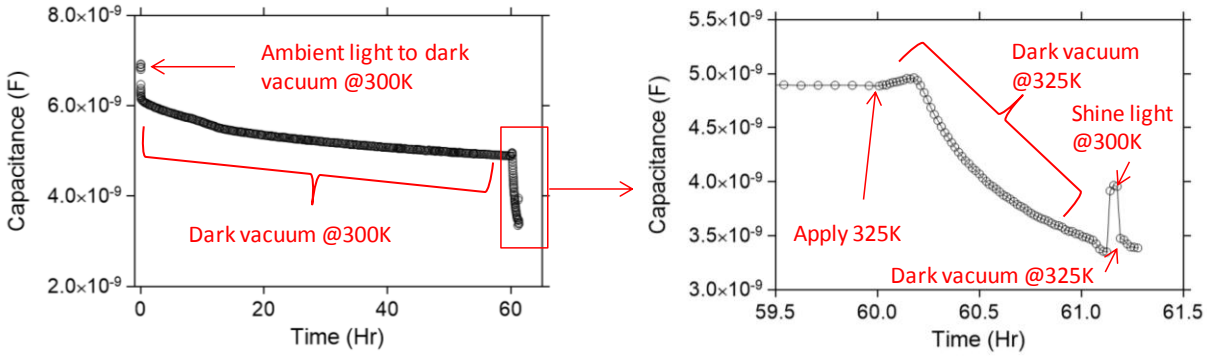

Figure 36: effects of the vacuum environment on the capacitance of a P3HT:$PC_{60}BM$ OPV. Device is in the dark at 300 K and data was taken at 10 kHz.

Figure 36 shows one such example at 300 K/10 kHz for 50+ hours. As shown, a large drop in the capacitance is seen over the course of the experiment. Clearly, this change will cause issues with the validity of successive CF measurements and makes the accurate characterization of the attempt-to-escape frequency extremely difficult, if not impossible. At 300K, the capacitance was not stable even after 50 hours. As such, 325 K was then applied to the device. An initial increase is first seen – corresponding to an increase in the response of trap states at the measurement frequency – followed by a rapid decrease in the capacitance. To determine if the decrease was caused by the release of deeply stored photocharge, light was then shined at 300 K and the sample subsequently returned to the a dark vacuum at 325 K. As expected, a jump in the capacitance was noted, followed by a quick decrease. However, this increase in the capacitance did not reach the same value as the light application at 0 hrs – indicating there is another mechanism which caused the dramatic decay of the capacitance over the 61 hour experiment. Of course, the sample encountered no low temperatures during this measurement, leaving only the possibility of environmental change.

It is known that P3HT films de-dope when contained within a vacuum[43] (likely, any oxygen deficient environment). This de-doping phenomenon is attributed to the desorption of oxygen and is expected to occur in the timeframe of *weeks* at 300 K to just a matter of minutes at higher temperatures (e.g. 370 K).[43] To test this likely explanation of the capacitance-time data, the capacitance of a P3HT device through the application of 375 K within the cryo vaccum was then monitored and CV doping data – remembering that oxygen induces a *p*-type doping on these devices – was taken before and after (**Figure 37**).

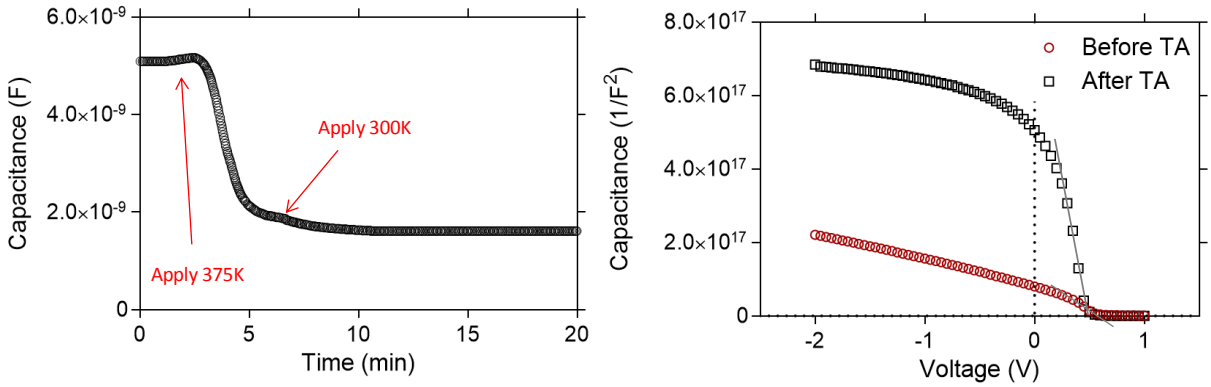

Figure 37: (left hand) effects of 375 K *stabilization* on the capacitance of a P3HT:$PC_{60}BM$ OPV in the cryo vacuum. Data taken at 10 kHz. (right hand) Mott-Schottky representation of CV data taken before and after the thermal annealing (TA) treatment. Data taken at 200 kHz.

As can be seen, the 375 K treatment brought about a rapid decrease in the device capacitance in just a matter of minutes – the drop larger than both the 300 K and 325 K treatments. After returning to 300 K, the capacitance became very stable and remained so for

the course of the TCF experiment. CV data taken before and after the vacuum heat treatment is shown in the right hand panel of Figure 37. A large decrease in the measured free charge carriers was found, from $3.0x10^{16}$ cm^{-3} before to $7.0x10^{15}$ cm^{-3} after the thermal treatment. This readily supports the notion of oxygen desorption and, thereby, the removal of the related defects. As such, all P3HT based devices were stabilized at either 375 K (10 min) or 325 K (20 hrs) before the TCF experiment.

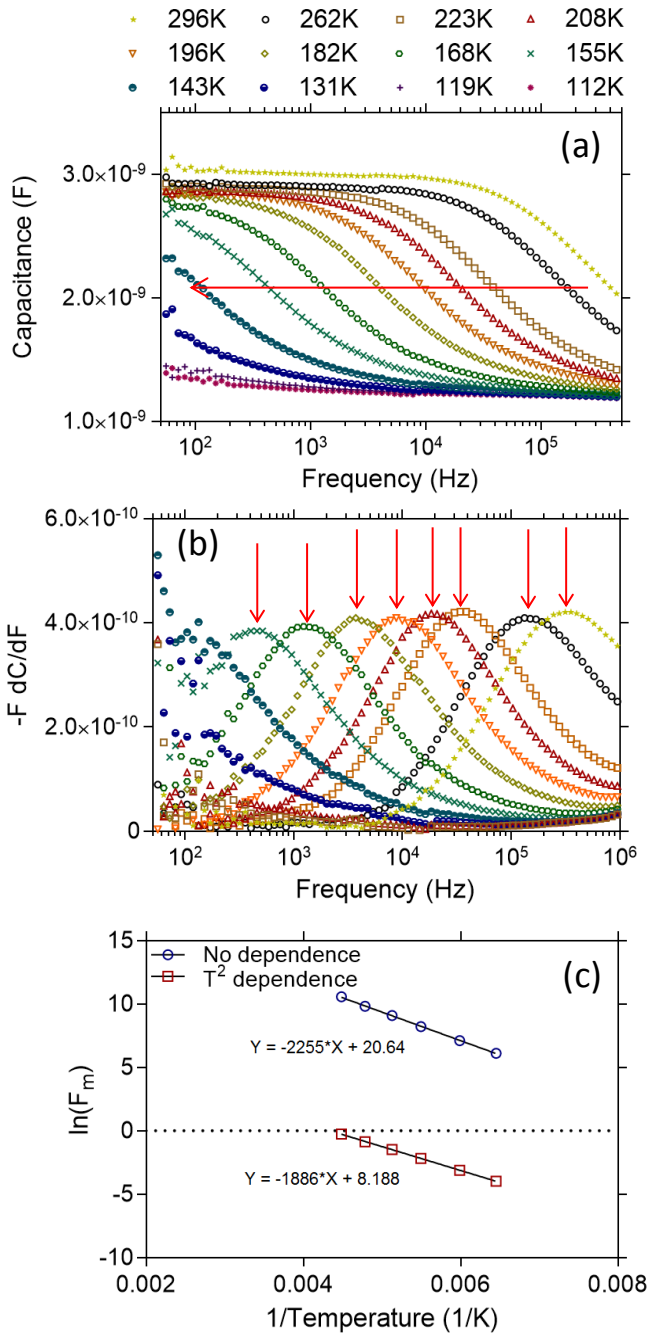

Figure 38: (a) capacitance versus frequency as a function of temperature for a sample P3HT:$PC_{60}BM$ solar device. The red arrow indicates the Arrhenius shift of the trap states with lowering temperatures. (b) –F dC/dF differential. Arrows indicate emission peaks. (c) Arrhenius plot of the –F dC/dF peak frequencies versus 1/T.

Figure 38a shows sample TCF for P3HT:$PC_{60}BM$ based OPVs. A clear shift in the capacitance is seen with decreasing temperatures. At low enough temperatures (<200 K), the geometric capacitance appears as the freezeout condition is reached in the higher frequencies. Extending from this geometric capacitance, a sharp step in the capacitance from *ca.* 1.75 nF to *ca.* 2.7 5nF can be seen. As such, a peak in the –FdC/dF differential is found in **Figure 38b** and shifts to lower frequencies with lower temperatures. The frequencies at which these peaks occur are plotted versus 1/T in **Figure 38c**. A straight line is revealed by the Arrhenius plot, yielding an attempt-to-escape frequency of $1.0x10^9$ Hz and an activation energy of 210 meV.

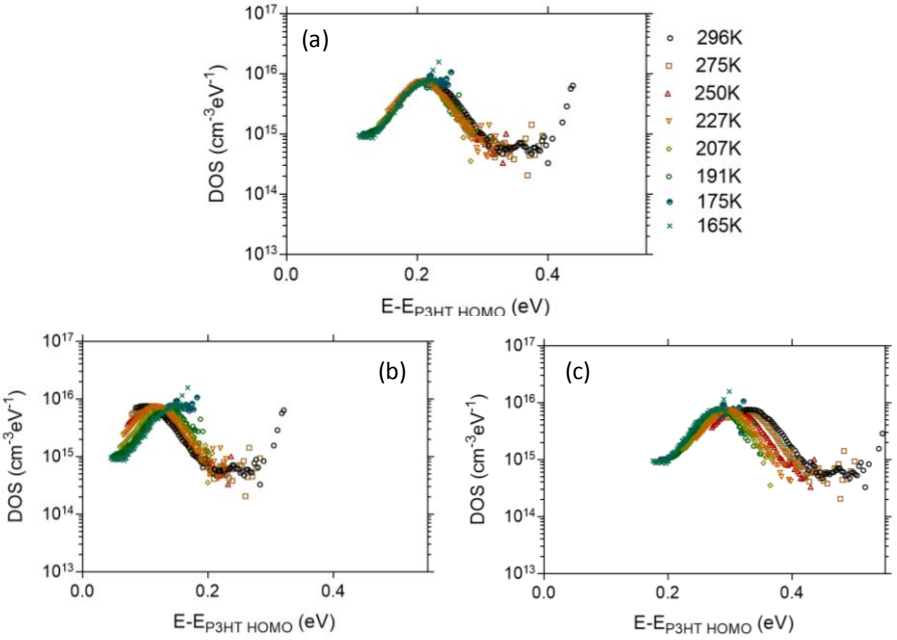

Figure 39: tDOS profile per temperature for a sample P3HT:$PC_{60}BM$ OPV as calculated by the Walter *et. al.* model. (a) Attempt-to-escape frequency of $1.0x10^9$ Hz. (b) Attempt-to-escape frequency of $1.0x10^7$ Hz. (c) Attempt-to-escape frequency of $1.0x10^{11}$ Hz.

Figure 39 shows the corresponding tDOS profile as calculated by the Walter *et al.* formalism for different sample temperatures. The profile is in agreement with the data detailed in Chapter IV – with the energy shift corresponding to the newly measured attempt-to-escape frequency. Clearly, the new attempt-to-escape frequency gives good overlap in the tDOS profile of individual temperatures (**Figure 39a**), while a prefactor two orders of magnitude lower (**Figure 39b**) or higher (**Figure 39c**) skews the temperature results. A dominant band at 200 meV (as predicted by the Arrehenius plot) can be seen. In the previous chapter, this first step was referred to as a deep defect band, however, this temperature data indicates this band is better described as the free carrier response band – a step in capacitance from $C_d = \varepsilon_s\varepsilon_o A/t$ to $C_d = \varepsilon_s\varepsilon_o A/W$.[62] This response band is expected to have a thermal activation energy which corresponds to the Fermi-level. The TCF measured 210 meV corresponds well to the Fermi-level (220 meV) calculated from the CV measured doping ($2.0\text{x}10^{15}$ cm^{-3}; assuming $N_v=1.0\text{x}10^{19}$ cm^{-3}). Moving higher in energy, deeper states are revealed and the beginnings of the second Gaussian can be seen. Careful analysis of the temperature data between 0.25 eV and 0.35 eV shows a lower attempt-to-escape frequency – around $1.0\text{x}10^{8}$ Hz. This indicates that the carrier response band and deeper defects do not share the same prefactor. **Table 13** summarizes the experimental data. One notes the reduction of measured traps in this device compared to that of the previous chapter. This is likely the result of the thermal stabilization, which will remove both oxygen and structural based defects.

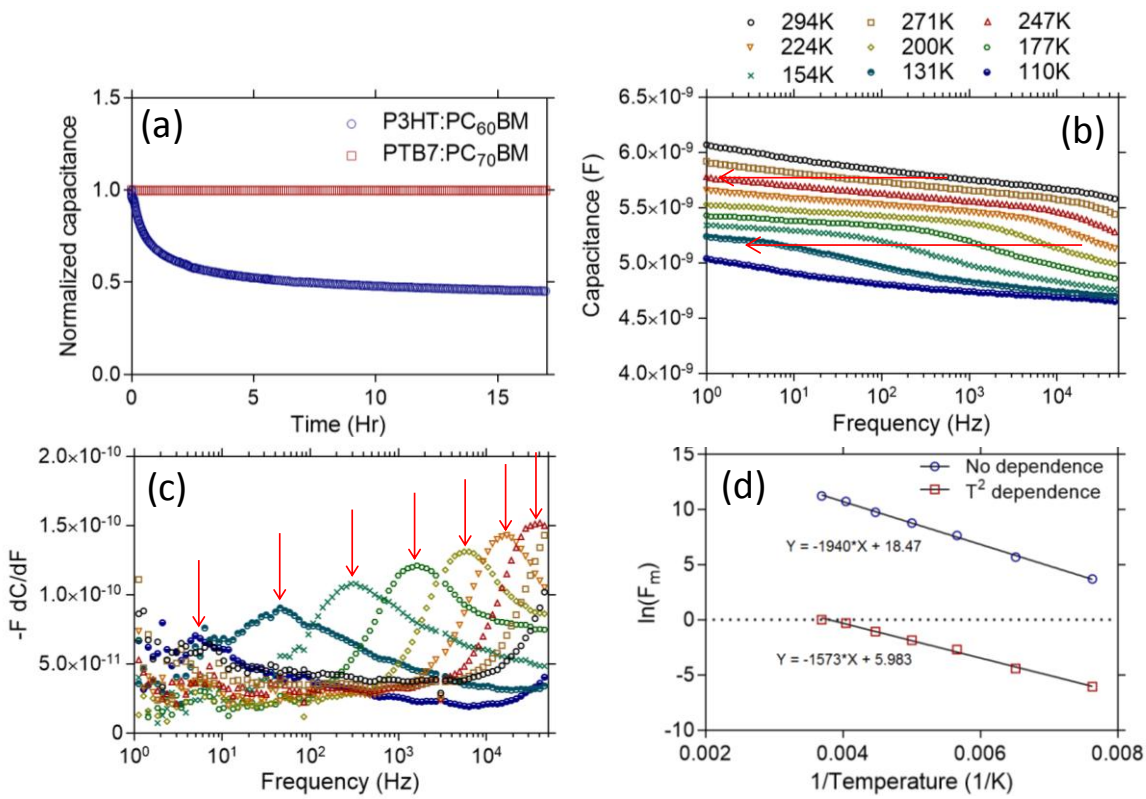

Figure 40: (a) capacitance (normalized) versus time for P3HT and PTB7 based devices within the cryo vacuum at 325 K. (b) Capacitance versus frequency as a function of temperature for a sample PTB7:$PC_{70}BM$ solar device. The red arrows indicate the Arrhenius shift of the trap states with lowering temperatures. (c) –F dC/dF differential. Arrows indicate emission peaks. (d) Arrhenius plot of the –F dC/dF peak frequencies versus 1/T.

Figure 40 shows similar data for PTB7:$PC_{70}BM$ based devices. Interestingly, these devices did not need to be stabilized to the vacuum environment. **Figure 40a** shows a comparison of the capacitance versus time (devices within the vacuum environment at 325K) for P3HT and PTB7 OPVs. No decrease in the PTB7 capacitance or change in the free carrier density was noted. **Figure 40b** shows sample TCF data for these devices; a clear shift in the

capacitance with decreasing temperature is seen. Again, a somewhat sharp step followed by a slower increase in the capacitance is displayed. **Figure 40c** shows the corresponding –FdC/dF differential and **Figure 40d** the Arrhenius plot of these peaks. An attempt-to-escape frequency of $2.0x10^{8}$ Hz with an activation energy of 170 meV was found. Because this capacitance step starts at the geometric value, it again likely corresponds to the carrier response band. The TCF measured activation energy (170 meV) closely matches the Fermi-level (160 meV) calculated from the CV measured doping ($2.0x10^{16}$ cm^{-3}). **Figure 41** shows the corresponding tDOS. A clear Gaussian at about 170 meV leads into deeper states which appear to be increasing slightly with increasing energy. Careful analysis of the temperature data between 0.15 eV and 0.25 eV shows a slightly lower prefactor for the deeper states; about $5.0x10^{7}$ Hz. Table 13 summarizes the experimental data.

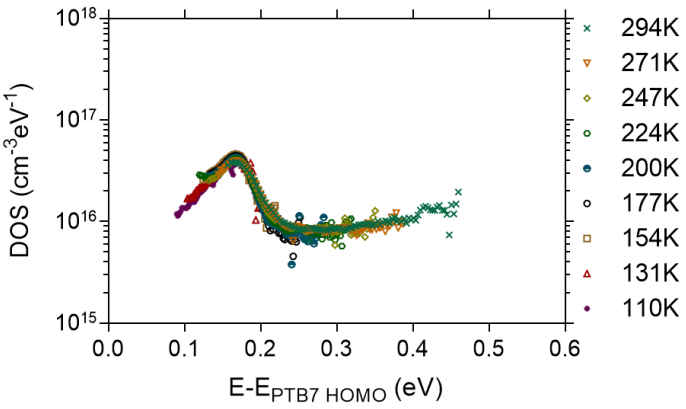

Figure 41: tDOS profile per temperature for a sample PTB7:PC_{70}BM OPV as calculated by the Walter *et. al.* model.

Figure 42 shows the experimental data for PCDTBT:$PC_{70}BM$ based devices. Again, the devices did not need to be stabilized to the vacuum environment. **Figure 42a** shows a comparison of the capacitance versus time (devices with the vacuum environment at 300K) for P3HT, PTB7 and PCDTBT OPVs. No decrease in the PCDTBT (as well as the PTB7) device capacitance was seen over the 17+ hour experiment. **Figure 42b** shows the TCF data for a sample PCDTBT based device. A shift in the capacitance with temperature is seen. The capacitance increase is mainly broad; however, a subtle step can be seen near 5.8 to 5.9 nF (highlighted by the red arrow). As such, a weak peak in the –FdC/dF differential can be seen (**Figure 42c**). The peak frequencies are plotted versus 1/T in **Figure 42d**, revealing an attempt-to-escape frequency of 6.0×10^9 Hz and an activation of 358 meV. Clearly, this capacitance step does not originate at the geometric capacitance, indicating this is a deep defect band – shifting the capacitance to $C_d = \varepsilon_s \varepsilon_o A / \langle x \rangle$.[62]

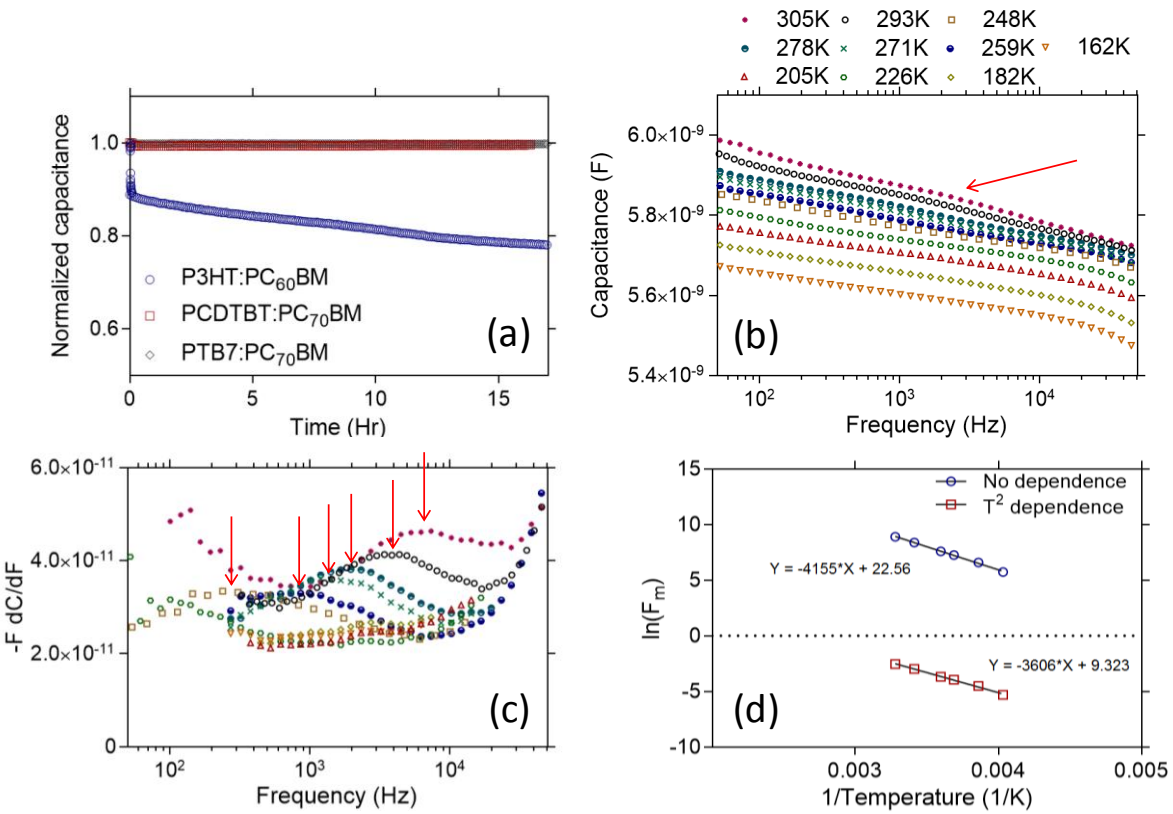

Figure 42: (a) capacitance (normalized) versus time for P3HT, PTB7 and PCDTBT based devices within the cryo vacuum at 300 K. (b) Capacitance versus frequency as a function of temperature for a sample PCDTBT:$PC_{70}BM$ solar device. The red arrow indicates the Arrhenius shift of a trap band with lowering temperatures. (c) –F dC/dF differential. Arrows indicate emission peaks. (d) Arrhenius plot of the –F dC/dF peak frequencies versus 1/T.

Figure 43 shows the corresponding tDOS. The deep Gaussian defect is revealed around 360 meV while what may be the carrier response band begins to appear at lower energies. Doping in the range of $1.0x10^{16}$ cm^{-3} was found *via* CV measurements, putting the Fermi-level at *ca.* 180 meV. Table 13 summarizes the experimental data.

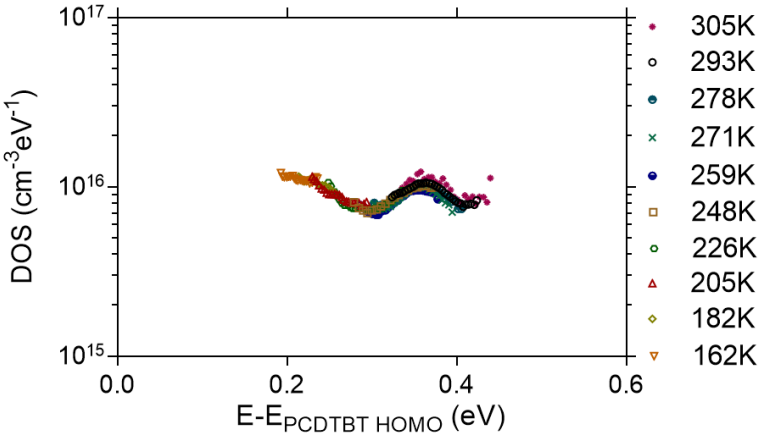

Figure 43: tDOS profile per temperature for a sample PCDTBT:$PC_{70}BM$ OPV as calculated by the Walter *et. al.* model.

	ν_0 (Hz)	Υ (Hz/K^2)	Ea (meV)	σ (cm^2)*
P3HT:$PC_{60}BM$	1.20×10^{9}	5.30×10^{3}	210	1.20×10^{-17}
PTB7:$PC_{70}BM$	2.30×10^{8}	7.20×10^{2}	190	2.30×10^{-18}
PCDTBT:$PC_{70}BM$	4.50×10^{9}	7.90×10^{3}	358	4.50×10^{-17}

Table 13: summary of TCF measured data. *$\langle V_{th} \rangle = 10^7$ cm/sec and $N_V = 10^{19}$ cm^{-3} was assumed for these calculations.

5.1.5 Project conclusion

Herein the pre-exponential factor of trap emission in organic photovoltaic devices was investigated. This prefactor – often referred to as the attempt-to-escape frequency – is essential if one is to accurately describe detrapping dynamics, making it an important parameter in a wide range of measurements and models. This characteristic parameter is

readily obtained through temperature dependent capacitance-frequency measurements. Three different polymer systems were studied: namely, (i) P3HT:$PC_{60}BM$, (ii) PTB7:$PC_{70}BM$ and (iii) PCDTBT:$PC_{70}BM$ based OPVs. Each was found to have an attempt-to-escape frequency in the range of 10^{8} to 10^{10} Hz, yielding a capture cross section in the range of 10^{-16} cm^2 to 10^{-18} cm^2. Further, using the Walter *et al.* interpretation of the TCF data, the deep trap profiles of these polymer devices have been presented. Each polymer showed carrier response band at lower temperatures, leading into deep defects at higher energies. In P3HT a brief area of constant DOS trailing to a sharp Gaussian was seen. PTB7 showed a nearly constant tDOS, with only a slight rise towards the deeper energies. PCDTBT showed a clear, complete Gaussian. The measured prefactors correlate well with that measured for PPV based devices.[61,80] This similarity in the measured attempt-to-escape frequencies and, thereby, the capture cross sections indicates that the trapping mechanisms in these polymers are likely similar.

6 CHAPTER VI: CONCLUSION

6.1 Synopsis

In any microelectronic device, fundamental physical parameters must be well understood for successful electronic optimization. One such prominent parameter is energetic trap states, which are well-known to plague amorphous or otherwise impure semiconducting materials. Organic semiconductors are no strangers to such states and their electronic properties are evidently tied to these defects. This report discussed the identification and characterization of bandgap residing trap levels in organic photovoltaic devices. A compilation of select studies to date was given and an overview of the author's work has been detailed.

Within the community, several techniques have been leveraged to study these mid-gap states. Atop this list are optical (PSD, UV-Vis.), capacitance (CV, CF, DLTS) and current (TSC, SCL modeling, Poole-Frenkel modeling) measurements and each has provided important pieces to the overall picture. Organic photovoltaic materials have been depicted as disordered semiconductors with a seemingly continuous distribution of both energetically shallow and deep trap bands. Upon blending these pure materials to create the modern day bulk heterojunction, energetic disorder increases and new trap bands appear. These states have been shown to stem from both intrinsic (e.g. structural disorder) and extrinsic (e.g. oxygen, synthesis contaminates) sources and it is quite clear that such states can have profound effects on, if not completely control, the electronic properties and long term stability of OPV devices. Several works highlighting the drastic effects trap states can have on OPV performance have evidently shown this – citing enhanced trap-assisted recombination, Fermi-level pinning, space-

charge effects and the like. Though these mid-gap traps have a large negative impact, it should also be remembered that they can give an advantageous inherent doping, improving conductivity and interfacial electric fields. Evidently, continued progress in understanding the nature, sources, affects and mitigation of the defects in both current and future materials will be crucial to the optimization of this promising technology.

The primary work of this dissertation has been to further the current body of knowledge on the identification and characterization of defect states in OPV devices. Capacitance techniques were heavily employed herein. As such, the accurate capacitance characterization of OPV devices was first visited. It was found that, owing to thinner films and larger series resistance, the series parameters could not be neglected in the typical frequency range of interest or significant errors and misinterpretations were introduced. Deeper, unknown defects were then identified using low frequency capacitance measurements coupled with a point by point differential of high frequency CV data. The defects remain important as it is those states closer to the midgap which more efficiently contribute to recombination and can be detrimental to device performance. More generally, the presented technique gives a generic overview of the capacitance response of OPV devices – enabling others to better study defects in future, higher efficiency devices. Lastly, the pre-exponential factor of trap emission was studied. This parameter is essential if detrapping dynamics are to be properly described – important, among other things, for the CF theory applied herein. This similarity in the measured attempt-to-escape frequencies and, thereby, the capture cross sections indicates that the trapping mechanisms in these polymers are likely similar.

6.2 Outlook towards future work

This section looks to give some guidance as to how to build upon the work presented herein. Of course, the primary goal of the identification and characterization of energetic defect bands in organic photovoltaic devices is their potential mitigation and/or enhancement. It is predicted that one avenue towards higher efficiency devices is the removal of defect states which hinder electronic properties (e.g. deep recombination centers) and the enhancement of those states which improve them (e.g. advantageous doping states). Thus, the mitigation of electronic defects with be heavily explored here. Two subsections are presented: the first summarizes defect mitigation work to date and the second gives an outlook for moving forward.

6.2.1 Defect mitigation

With some understanding as to the presence and characteristics of trap sites in OPV devices, I now look at some recent efforts to mitigate. The goal here is to give the reader an introduction and general overview of the current works centered on defect mitigation. I begin with a discussion on structural ordering.

Much work has gone into studying the crystallization kinetics of organic materials and blends thereof. Several techniques, including thermal annealing, solvent annealing and solvent additives, have been adopted or developed to promote self-organization in OPV devices.[60] When employing these techniques, most groups cite a higher degree of crystallinity coupled

with enhancements in physical parameters (e.g. mobility) as well as photovoltaic performance. Though most of these reports do not show any direct measurements of trap states, this strongly indicates that structural defects are being reduced. In the case of deeper levels, this idea is fully supported by Nalwa *et al.*'s and Sharma *et al.*'s growth rate works, as discussed above.[21,89] Further, when comparing the apparent hole concentrations and processing conditions of Dennler *et al.'s* and Li *et al.'s* works, some evidence was presented that the case is similar for shallower levels and doping.[14,59] This readily points out the obvious – one avenue towards trap reduction in OPV devices is promoting more order in the film structure. Though this assertion is seemingly unexciting, it represents a vast and important area of research. Numerous reports on the self-assembly topic can be found in the literature,[147] and their continued application and development will be important to trap mitigation in both current and future OPV materials.

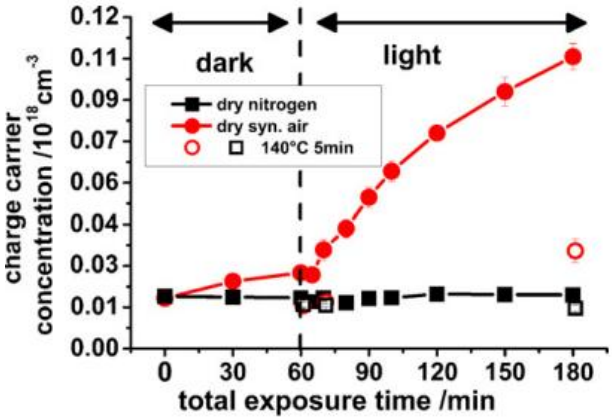

Figure 44: charge carrier concentrations calculated from the data of FIg. 5 [of original article] by using Eq. (2) [of original article]. Reprinted from publication [46], Copyright [2011], with permission from Elsevier.

In addition to crystallinity affects, thermal treatments have also been shown to promote the desorption of oxygen, reversing its effects on the ionized acceptor impurity concentrations.[16,41,43,45,46,77,148] One such example is shown by Seemann *et al.* in **Figure 44**.[46] Clearly, the extrinsic impurities induced by synthetic air are readily reduced through thermal treatment. Glatthaar *et al.* found a similar reduction in doping and noted an improved rectification for P3HT:PCBM BHJ cells after post-production thermal annealing under forward biasing.[77] This is further supported by Nam *et al.*'s aforementioned modeling work.[76] The authors found that a post-production treatment of their air-processed devices significantly reduced oxygen content in the active layer blend. The group proposed this lead to a reduction in the oxygen-related impurities, and thereby, an enhancement to the short circuit current.[76] Hintz *et al.* offer further details as to this desorption through photoelectron experiments.[41] After monitoring binding energies and oxygen content through a series of exposure/annealing cycles, the group identified two oxygen species: one reversible and one irreversible. The former correlates to noted changes in the material doping and was found to be only a small fraction of the total oxygen content.[41] This is attributed to physisorbed oxygen which forms a CTC as previously discussed. The latter existed in higher numbers and was attributed to oxygen contained within photooxidation products.[41] They believe this bound species is contained to electrically isolated molecular sites, and thereby, the electronic structure of the π-system is not largely alterd.[41] Seemann *et al.* noted a similar irreversible aspect in their oxygen degradation studies, attributed to photochemical oxidation.[46] They believe this irreversible portion may induce a slight increase in the mobile hole concentration (Figure 44), and thereby, decrease

carrier mobility.[46] It is worth noting that although moderate temperatures (>100 ℃) may be needed for the rapid removal of oxygen,[148] desorption is still expected to occur even at room temperature, albeit on a much longer timeframe.[43] Of course, this point is supported by the data presented in 5.1.4.

Along with structural and oxygen induced defects, impurities from material synthesis must also be carefully mitigated. Not only would this relieve the performance degradations discussed in chapter II, but also may be advantageous for better device reproducibility. It is thought that batch-to-batch variations in the residual synthesis impurities are a significant factor affecting the poor batch-to-batch reproducibility of OPV optoelectronic properties,[72,73] making the mitigation of such impurities a promising avenue towards more consistent processing. Unfortunately, the detection of trace (e.g. <1% by weight) synthesis impurities, and thereby the estimation of material purity, has proven challenging with traditional methods.[17,72,73,149] Though, Nikiforov *et al.'s* recent work shows synchrotron X-ray fluorescence as a promising measurement for identifying trace residuals and quantifying their concentrations.[73] Making matters worse, purification – especially noted for the case of palladium – is notoriously difficult as decomposition of this transition metal catalyst forms nanoparticles which can tightly bind to the backbone of conjugated polymers.[72] [73,149] Fortunately, the works of Krebs *et al.* have begun to tackle this issue.[71,149,150] In the initial PPV based work, the authors undertook multiple micro-filtrations in order to remove the palladium contaminant.[71] A two fold increase in film resistance (30 to 60 Ω) was achieved as the shunt paths induced by the palladium nanoparticles were removed. With a subsequent boiling of the

polymer in a ODCB:triphenylphosphine mixture and a precipitation with methanol, the resistance was further increased to 100 Ω – though, still short of the 150 Ω found for the more palladium free case.[71] This work was then built upon by treating palladium contaminated PPV (as well as two other polymers) with a azothioformamide derivative to dissolve the residual.[149] The authors found an impressive drop in palladium content (17,860 to <0.10 ppm) coupled with a 300x improvement of film resistance.[149] A year later, the group then pushed this idea further to demonstrate the ability of azothioformamide derivatives to remove other transition metals (i.e. palladium, platinum, copper and nickel) from contaminated organic products.[150] More information on synthesis, purification and the associated challenges can be found throughout the literature.[151,152]

Wang *et al.* have tackled defect mitigation from a different point of view.[22] Taking cues from trap-rich amorphous silicon, which is typically hydrogenated to reduce the concentration of defects, Wang treats P3HT with a cation donor, dimethyl sulfate.[22] The polymer solution was reacted with the donor in hopes that cations would be donated to the polymer backbone and annihilate negatively charged defects. As a byproduct, the authors asserted an unbound sulfate counterion would be formed, though, it is expected that this 'defect' would have less influence on electrical properties.[22] As such, one would expect improvements in the abovementioned deficiencies created by charged defects (charge mobility, exciton diffusion length, etc.). The authors showed just that through time-of-flight (mobility) and fluorescence (exciton diffusion length) measurements.[22] One might be inclined to argue that the chemical treatment could act much the same as a solvent additive – affecting crystallization kinetics and film morphology,

which could bring about the same type of improvements.[60] However, optical absorption and x-ray diffraction measurements revealed no substantial changes to structure and morphology.[22] Though photovoltaic improvement was meager, photostability was dramatically improved with this treatment.

This work was extended by Liang *et al.* in 2009.[23] Here, the authors furthered the study on dimethyl sulfate and expanded to include a second regent, lithium aluminum hydride (LAH). To be thorough, the study also mentioned treatments with sodium borohydride, sodium methoxide and methyl iodide, as well as treatments on PPV, which all gave consistent results.[23] Similar to the previous work, mobility and exciton diffusion length enhancements were noted, with LAH producing the largest increases – 17 fold for mobility and two fold for exciton diffusion.[23] Photostability was also again improved. Interestingly, the zero-field dark conductivity increased by a factor of five for dimethyl sulfate, but increased only slightly in the case of LAH treatement. Thereby, the mobile hole density doubled for dimethyl sulfate treatments, but decreased by a factor of 13 for LAH. The estimated total defect density dropped by an order of magnitude in the case of dimethyl sulfate ($1x10^{19}$ cm^{-3} to $1x10^{18}$ cm^{-3}) and by nearly three orders of magnitude for LAH (to $3x10^{16}$ cm^{-3}),[23] directly highlighting the effectiveness of the mitigation technique.

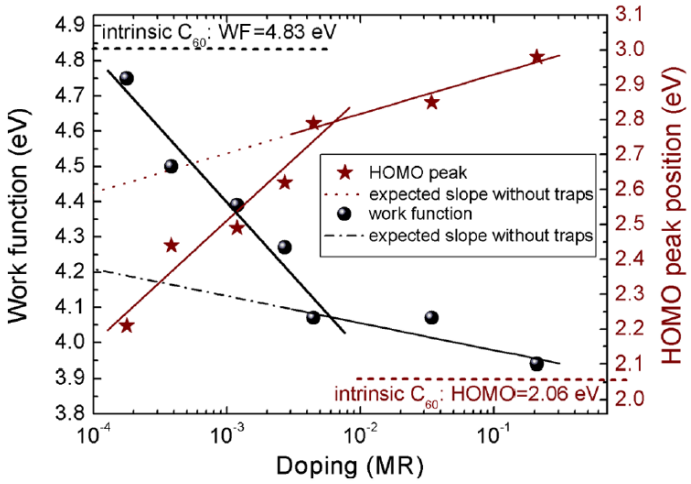

Figure 45: change in work function and HOMO peak position with respect to the Fermi-level upon doping. Deduced from the UPS spectra given in Fig. S2 [of the original article] in the SM [31; of the original article]. Because of the broadening of the HOMO feature at high doping, the HOMO position is given by the peak value. The corresponding values for the intrinsic C_{60} film are given by the top and bottom dashed horizontal line, respectively. Reprinted with permission from [153]. Copyright [2012] by the American Physical Society.

A similar concept has also been applied to mitigate electron traps in PPV and, more recently, C_{60}.[153,154] In the latter, the ruthenium(pentamethylcyclopentadienyl)(1,3,5-trimethylbenze) dimer $[RuCp^*(mes)]_2$ was added to the trap-rich fullerene *via* co-evaporation.[153] Thereby, an extra, molecular *n*-type doping was introduced into the system, traps were filled and passivation was achieved. Direct evidence of this is presented in **Figure 45**, where the peak HOMO position and work function are plotted versus the doping molar ratio (MR).[153] Clearly, a trend in the energetic positions is seen with increasing dimer doping. The authors assert such a trend is consistent with the Fermi-level moving through a distribution of

trap states towards the LUMO manifold.[153] Around a MR of *ca.* 6.0E-3, the trend merges with the expected trap-free slope, giving some quantification as to the minimum doping density needed for controlled passivation. Through this process, both conductivity and mobility were vastly improved – indicating potential improvements for OPV performance. Similar data has been shown for other dopant materials in C_{60} systems.[155,156] Further, when recalling the work of Garcia-Belmonte *et al.* (Figure 13) it is remembered that a decrease of electronic states in the acceptor material alleviates Fermi-level pinning and enhances the achievable V_{oc}.[34] This enhancement should also remain true for trap passivation as detailed here. In fact, such a case with donor materials was hinted at by Boix *et al.*, who incidentally found that inverted cells had four times the *p*-type doping and an increased V_{oc} when compared to a regular structure.[157] As a result of the excess holes, E_{Fp} was expected to shift towards the HOMO, thereby increasing the achievable open-circuit voltage.

6.2.2 Outlook

Having been submerged in this work in this work for several years, I can give some guidance as to how to continue for the betterment of OPV devices. Of course, it will be of upmost importance to extend the methods and works discussed above to probe and better understand the complete trap profiles of the new, most promising OPV systems. Trap-related conclusions made for one organic material set may not be directly applicable to the next – especially considering the potential for vast differences in the synthesis impurity concentration, inherent structural disorder, sensitivity to oxygen/moisture, etc. – truly highlighting that trap effects cannot be overlooked. It is plain to see that the characteristic parameters of the defect

distribution(s) as well as their origin(s) must be understood such that these future, high efficiency materials can be further optimized through a reduction of these electronic states. As a general approach, I align with and build upon the idea of Gregg.[26] OPV materials should first be pushed towards a more ideal, intrinsic state through structural ordering, the removal of oxygen states, material purification, etc. Subsequently, remaining traps might then be further reduced through chemical passivation and the electronic properties rebuilt through a controlled, extrinsic doping. Though it may be impossible to completely rid these systems of electronic traps, their reduction by even a couple orders of magnitude will likely prove fruitful.

To accomplish this goal, measurement as well as mitigation techniques must be continually developed. For example, though defects are widely studied using various techniques, no groups are currently building complete trap profiles using a combination of the methods discussed above. For instance, thermally stimulated current and sub-gap absorption measurements can be used to elucidate the shallower states, which can then be coupled with detailed capacitance measurements to probe the deeper states. The completed trap profile can be used in current and photovoltaic modeling to confirm and show the defect profiles' affect on electronic properties. This would give an all inclusive defect picture on the single OPV device (instead of piecing together several works to build the profile) which can then be systematically altered to determine the effects of mitigation techniques. Thereby, comprehensive reports highlighting a change in trap concentrations at specific energies coupled with a change in photovoltaic parameters would greatly contribute to the science of OPVs. The combination of mitigation techniques (e.g. thermal treatments with chemical passivation) as well as the application of a

mitigating electrical field and the development of different growth/crystallization methods are interesting avenues to consider.

7 RESEARCH PATH AND PUBLICATIONS

7.1 Research path

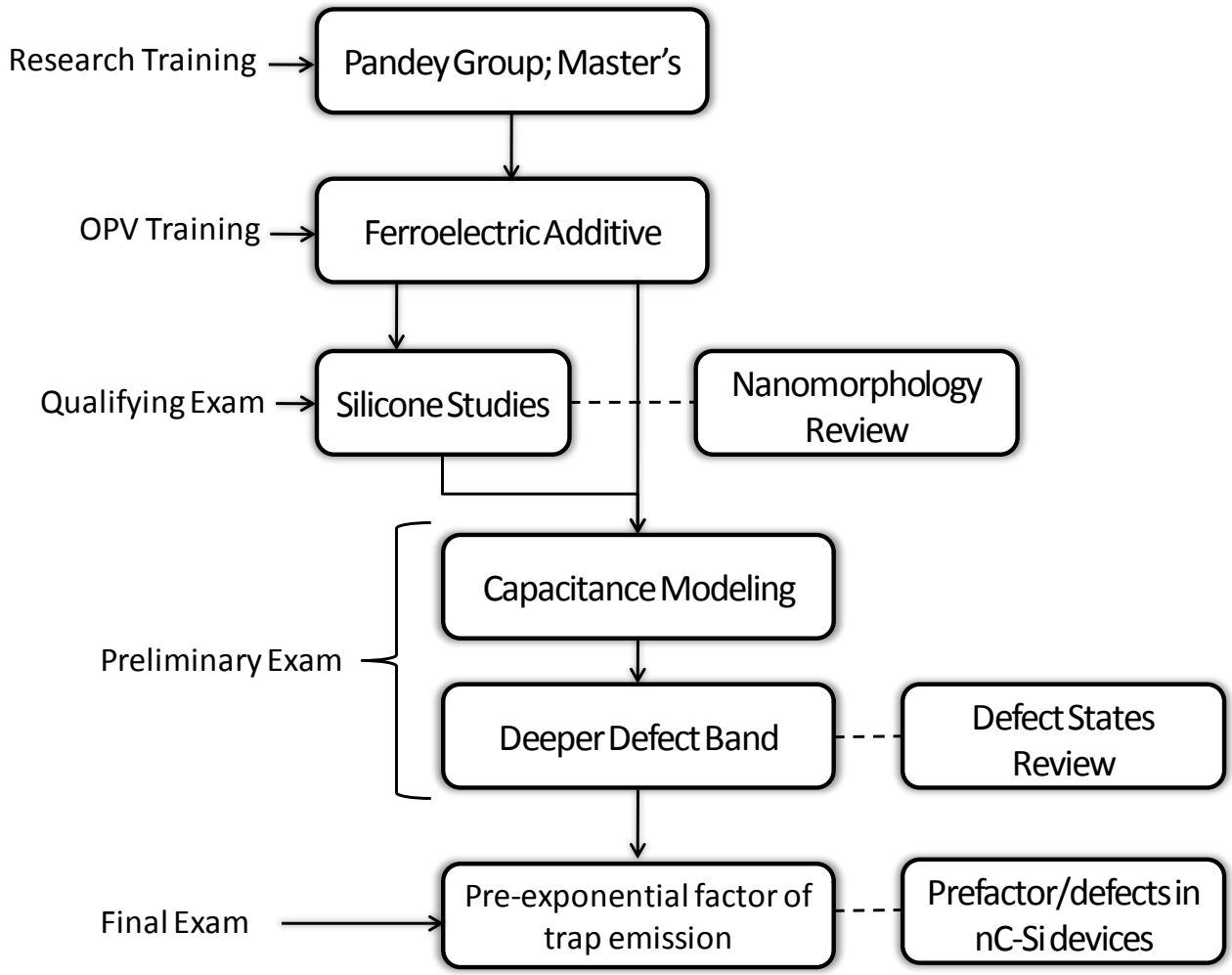

Figure 46: block diagram summarizing the progression of the author's OPV based projects and academic path.

7.2 Peer reviewed journal articles

8. **Carr, J. A.** amd Chaudhary, S., 2013. The identification, characterization and mitigation of defect states in organic photovoltaic devices: a review and outlook. **Energy & Environmental Science.** 6 (12), 3414-3438 [Invited review article]

7. **Carr J. A.** and Chaudhary, S., 2013. On the identification of deeper defect levels in organic photovoltaic devices. **Journal of Applied Physics**, 114, 064509

6. Mahadevapuram, R. C., **Carr, J. A.**, Chen, Y., Bose, S., Nalwa, K. S., Petrich, J. W., Chaudhary, S., 2013. Low-boiling-point solvent additives can also enable morphological control in polymer solar cells. **Synthetic Metals**. 185, 115-119.

5. Meyer, M. W., Larson, K. L., Mahadevapuram, R. C., Lesoine, M. D., **Carr, J. A.**, Chaudhary, S., Smith, E. A., 2013. Scanning angle-Raman spectroscopy of poly (3-hexylthiophene)-based films on indium tin oxide, gold and sapphire surfaces. **Applied Materials & Interfaces.** 5(17), 8686

4. **Carr, J.A** and Chaudhary, S., 2012. On accurate capacitance characterization of organic photovoltaic cells. **Applied Physics Letters**. 100, 213902

3. **Carr, J.A**, Nalwa, K.S., Mahadevapuram, R., Chen, Y., and Chaudhary, S., 2012. Plastic-syringe induced silicone contamination in organic photovoltaic fabrication: implications for small-volume additives. **Applied Materials and Interfaces**. 4, 2831

2. Nalwa, K.S., **Carr, J.A.**, Mahadevapuram, R., Kodali, H.K., Chen, Y., Petrich, J., Ganapathysubramanian, B., and Chaudhary, S., 2012. Enhanced charge separation in organic photovoltaic films doped with ferroelectric dipoles. **Energy & Environmental Science** 5(5), 7042

1. **Carr, J.A**, Chen, Y., Ismail, M., and Chaudhary, S., 2011. Controlling nanomorphology in plastic solar cells. **Nanomaterials and Energy** 1(1), 18 [Invited review article]

7.3 Conference presentations and abstracts

7. **Carr, J.A.** and Chaudhary, S., 2014. Deep defect levels and the prefactor of trap emission in organic photovoltaic devices. **MRS** S14 H2.03, San Francisco, CA.

6. **Carr, J.A.** and Chaudhary, S., 2012. Improved capacitance modeling and its application to the identification of deeper defects in polymer photovoltaics. **MRS** F12 E19.74, Boston MA.

5. Nalwa, K.S., **Carr J.A.**, Mahadevapuram, R.C., Kodali, H.K., Ganapathysubramanian, B., Chaudhary, S.. 2012. More efficient polymer solar cells by doping with ferroelectric dipoles, **TMS** S12, Orlando FL [Invited presentation, given by John A. Carr]

4. **Carr, J.A**, Nalwa, K.S., Mahadevapuram, R., Chen, Y., and Chaudhary, S., 2011. Plastic-syringe induced silicone contamination in organic photovoltaic fabrication: a second look at its implications on device performance. **MRS** F11 H13.49, Boston MA.

3. Nalwa, K.S., **Carr, J.A.**, Mahadevapuram, R., Kodali, H.K., Chen, Y., Petrich, J., Ganapathysubramanian, B., and Chaudhary, S., 2011. Enhanced Exciton Dissociation in Organic Photovoltaic Layers Doped with Ferroelectric Dipoles. **MRS** F11 I6.9, Boston MA.

2. Mahadevapuram, R., Chen, Y., **Carr, J.A.**, Nalwa, K.S., and Chaudhary, S., 2011. Uncovering some more realities of solvent-additives in organic solar cells. **MRS** F11 H13.24, Boston MA.

1. Thoeming, A., **Carr, J.A.**, Mahadevapuram, R., and Chaudhary, S., 2011. Further investigation into the paintbrush deposition technique for P3HT:PCBM based organic solar cells. **MRS** F11 H13.88, Boston MA.

8 REFERENCES CITED

1 Yue, D., Khatav, P., You, F. & Darling, S. B. Deciphering the uncertainties in life cycle energy and environmental analysis of organic photovoltaics. *Energy & Environmental Science* **5**, 9163-9172 (2012).

2 Gregg, B. A., Chen, S. G. & Cormier, R. A. Coulomb forces and doping in organic semiconductors. *Chemistry of Materials* **16**, 4586-4599 (2004).

3 Tang, C. W. Two layer organic photovoltaic cell. *Applied Physics Letters* **48**, 183-185 (1986).

4 Yu, G., Gao, J., Hummelen, J. C., Wudl, F. & Heeger, A. J. Polymer Photovoltaic Cells - Enhanced Efficiencies Via a Network of Internal Donor-Acceptor Heterojunctions. *Science* **270**, 1789-1791 (1995).

5 Halls, J. J. M. *et al.* Efficient Photodiodes from Interpenetrating Polymer Networks. *Nature* **376**, 498-500 (1995).

6 He, Z. *et al.* Enhanced power-conversion efficiency in polymer solar cells using an inverted device structure. *Nature Photonics* **6**, 593-597 (2012).

7 Kirchartz, T., Taretto, K. & Rau, U. Efficiency limits of organic bulk heterojunction solar cells. *The Journal of Physical Chemistry C* **113**, 17958-17966 (2009).

8 Carr, J. A. & Chaudhary, S. The identification, characterization and mitigation of defect states in organic photovoltaic devices: a review and outlook. *Energy & Environmental Science* (2013).

9 Kaake, L., Barbara, P. & Zhu, X. Y. Intrinsic Charge Trapping in Organic and Polymeric Semiconductors: A Physical Chemistry Perspective. *The Journal of Physical Chemistry Letters* **1**, 628-635 (2010).

10 Abdou, M. S. A., Orfino, F. P., Son, Y. & Holdcroft, S. Interaction of oxygen with conjugated polymers: charge transfer complex formation with poly (3-alkylthiophenes). *Journal of the American Chemical Society* **119**, 4518-4524 (1997).

11 Hoshino, S. *et al.* Influence of moisture on device characteristics of polythiophene-based field-effect transistors. *Journal of applied physics* **95**, 5088 (2004).

12 Erwin, M. M., McBride, J., Kadavanich, A. V. & Rosenthal, S. J. Effects of impurities on the optical properties of poly-3-hexylthiophene thin films. *Thin Solid Films* **409**, 198-205 (2002).

13 Carr, J. A. *et al.* Plastic-Syringe Induced Silicone Contamination in Organic Photovoltaic Fabrication: Implications for Small-Volume Additives. *ACS Applied Materials & Interfaces* **4**, 2831-2835 (2012).

14 Dennler, G. *et al.* Unusual electromechanical effects in organic semiconductor Schottky contacts: Between piezoelectricity and electrostriction. *Applied Physics Letters* **87**, 163501 (2005).

15 Salzman, R. F. *et al.* The effects of copper phthalocyanine purity on organic solar cell performance. *Organic Electronics* **6**, 242-246 (2005).

16 Matsushima, T., Yahiro, M. & Adachi, C. Estimation of electron traps in carbon-60 field-effect transistors by a thermally stimulated current technique. *Applied Physics Letters* **91**, 103505-103505-103503 (2007).

17 Leong, W. L. *et al.* Role of trace impurities in the photovoltaic performance of solution processed small-molecule bulk heterojunction solar cells. *Chemical Science* (2012).

18 Lang, D., Chi, X., Siegrist, T., Sergent, A. & Ramirez, A. Bias-dependent generation and quenching of defects in pentacene. *Physical Review Letters* **93**, 76601 (2004).

19 Knipp, D. & Northrup, J. E. Electric-Field-Induced Gap States in Pentacene. *Advanced Materials* **21**, 2511-2515 (2009).

20 Gregg, B. A. Transport in Charged Defect-Rich π-Conjugated Polymers. *The Journal of Physical Chemistry C* **113**, 5899-5901 (2009).

21 Nalwa, K. S., Mahadevapuram, R. C. & Chaudhary, S. Growth rate dependent trap density in polythiophene-fullerene solar cells and its implications. *Applied Physics Letters* **98**, 093306 (2011).

22 Wang, D., Kopidakis, N., Reese, M. O. & Gregg, B. A. Treating poly (3-hexylthiophene) with dimethylsulfate improves its photoelectrical properties. *Chemistry of Materials* **20**, 6307-6309 (2008).

23 Liang, Z., Nardes, A., Wang, D., Berry, J. J. & Gregg, B. A. Defect Engineering in π-Conjugated Polymers. *Chemistry of Materials* **21**, 4914-4919 (2009).

24 Hepp, A., Von Malm, N., Schmechel, R. & Von Seggern, H. Effects of process parameters on trap distributions in organic semiconductors. *Synthetic metals* **138**, 201-207 (2003).

25 Wang, D., Reese, M., Kopidakis, N. & Gregg, B. A. in *Photovoltaic Specialists Conference, 2008. PVSC'08. 33rd IEEE.* 1-3 (IEEE).

26 Gregg, B. A. Charged defects in soft semiconductors and their influence on organic photovoltaics. *Soft Matter* **5**, 2985-2989 (2009).

27 Landsberg, P. T. *Recombination in semiconductors*. (Cambridge University Press, 2003).

28 Poortmans, J. & Arkhipov, V. *Thin film solar cells: fabrication, characterization and applications*. Vol. 18 (Wiley, 2006).

29 Smith, R. A. *Semiconductors*. Vol. 173 (Cambridge University Press Cambridge, UK, 1978).

30 Mandoc, M., Kooistra, F., Hummelen, J., de Boer, B. & Blom, P. Effect of traps on the performance of bulk heterojunction organic solar cells. *Applied Physics Letters* **91**, 263505 (2007).

31 Street, R. A. & Schoendorf, M. Interface state recombination in organic solar cells. *Physical Review B* **81**, 205307 (2010).

32 Cowan, S. R., Leong, W. L., Banerji, N., Dennler, G. & Heeger, A. J. Identifying a Threshold Impurity Level for Organic Solar Cells: Enhanced First-Order Recombination Via Well-Defined PC84BM Traps in Organic Bulk Heterojunction Solar Cells. *Advanced Functional Materials* **21**, 3083-3092 (2011).

33 McNeill, C. R., Hwang, I. & Greenham, N. C. Photocurrent transients in all-polymer solar cells: Trapping and detrapping effects. *Journal of applied physics* **106**, 024508 (2009).

34 Garcia-Belmonte, G. *et al.* Influence of the intermediate density-of-states occupancy on open-circuit voltage of bulk heterojunction solar cells with different fullerene acceptors. *Solar Cells* **11**, 14 (2010).

35 Bhattacharya, J., Mayer, R., Samiee, M. & Dalal, V. Photo-induced changes in fundamental properties of organic solar cells. *Applied Physics Letters* **100**, 193503 (2012).

36 Schafferhans, J., Baumann, A., Wagenpfahl, A., Deibel, C. & Dyakonov, V. Oxygen doping of P3HT: PCBM blends: Influence on trap states, charge carrier mobility and solar cell performance. *Organic Electronics* **11**, 1693-1700 (2010).

37 Dicker, G., de Haas, M. P., Warman, J. M., de Leeuw, D. M. & Siebbeles, L. D. A. The disperse charge-carrier kinetics in regioregular poly (3-hexylthiophene). *The Journal of Physical Chemistry B* **108**, 17818-17824 (2004).

38 Boix, P. P. *et al.* Determination of gap defect states in organic bulk heterojunction solar cells from capacitance measurements. *Applied Physics Letters* **95**, 233302-233303 (2009).

39 Gregg, B. A., Gledhill, S. E. & Scott, B. Can true space-charge-limited currents be observed in π-conjugated polymers? *Journal of applied physics* **99**, 116104-116104-116103 (2006).

40 Jain, S. *et al.* Injection-and space charge limited-currents in doped conducting organic materials. *Journal of applied physics* **89**, 3804-3810 (2001).

41 Hintz, H., Peisert, H., Egelhaaf, H. J. & Chassé, T. Reversible and Irreversible Light-Induced p-Doping of P3HT by Oxygen Studied by Photoelectron Spectroscopy (XPS/UPS). *The Journal of Physical Chemistry C* **115**, 13373-13376 (2011).

42 Meijer, E. *et al.* Photoimpedance spectroscopy of poly (3-hexyl thiophene) metal–insulator–semiconductor diodes. *Synthetic metals* **142**, 53-56 (2004).

43 Liao, H. H. *et al.* Dynamics and reversibility of oxygen doping and de-doping for conjugated polymer. *Journal of applied physics* **103**, 104506-104508 (2008).

44 Lu, C. K. & Meng, H. F. Hole doping by molecular oxygen in organic semiconductors: Band-structure calculations. *Physical Review B* **75**, 235206 (2007).

45 Lüer, L., Egelhaaf, H. J. & Oelkrug, D. (Photo) conductivity of conjugated oligomer films: mobile charge carrier formation by oxygen. *Optical Materials* **9**, 454-460 (1998).

46 Seemann, A. *et al.* Reversible and irreversible degradation of organic solar cell performance by oxygen. *Solar Energy* **85**, 1238-1249 (2011).

47 Aguirre, A., Meskers, S., Janssen, R. & Egelhaaf, H. J. Formation of metastable charges as a first step in photoinduced degradation in π-conjugated polymer: fullerene blends for photovoltaic applications. *Organic Electronics* **12**, 1657-1662 (2011).

48 Chikamatsu, M., Taima, T., Yoshida, Y., Saito, K. & Yase, K. Mg-doped C thin film as improved n-type organic semiconductor for a solar cell. *Applied Physics Letters* **84**, 127 (2004).

49 Arkhipov, V., Heremans, P., Emelianova, E. & Baessler, H. Effect of doping on the density-of-states distribution and carrier hopping in disordered organic semiconductors. *Physical Review B* **71**, 045214 (2005).

50 Liu, A. *et al.* Control of Electric Field Strength and Orientation at the Donor–Acceptor Interface in Organic Solar Cells. *Advanced Materials* **20**, 1065-1070 (2008).

51 Pierret, R. F. & Neudeck, G. W. *Advanced semiconductor fundamentals*. Vol. 6 (Addison-Wesley Reading, MA, 1987).

52 Goris, L. *et al.* Observation of the subgap optical absorption in polymer-fullerene blend solar cells. *Applied Physics Letters* **88**, 052113-052113 (2006).

53 Gotoh, T., Nonomura, S., Hirata, S. & Nitta, S. Photothermal bending spectroscopy and photothermal deflection spectroscopy of C_{60} thin films. *Applied surface science* **113**, 278-281 (1997).

54 Habuchi, H., Nitta, S., Han, D. & Nonomura, S. Localized electronic states related to O_2 intercalation and photoirradiation on C_{60} films and C_{70} films. *Journal of applied physics* **87**, 8580-8588 (2000).

55 Nikitenko, V., Heil, H. & Von Seggern, H. Space-charge limited current in regioregular poly-3-hexyl-thiophene. *Journal of applied physics* **94**, 2480 (2003).

56 Schafferhans, J., Baumann, A., Deibel, C. & Dyakonov, V. Trap distribution and the impact of oxygen-induced traps on the charge transport in poly (3-hexylthiophene). *Applied Physics Letters* **93**, 093303 (2008).

57 Neugebauer, S., Rauh, J., Deibel, C. & Dyakonov, V. Investigation of electronic trap states in organic photovoltaic materials by current-based deep level transient spectroscopy. *Applied Physics Letters* **100**, 263304-263304-263304 (2012).

58 Streetman, B. G. & Banerjee, S. *Solid state electronic devices*. Vol. 2 (Prentice-Hall, 1995).

59 Li, J. V. *et al.* Simultaneous measurement of carrier density and mobility of organic semiconductors using capacitance techniques. *Organic Electronics* **12**, 1879-1885 (2011).

60 Carr, J. A., Chen, Y., Elshobaki, M., Mahadevapuram, R. C. & Chaudhary, S. Controlling nanomorphology in plastic solar cells. *Nanomaterials and Energy* **1**, 8 (2012).

61 Campbell, A., Bradley, D., Werner, E. & Brütting, W. Deep level transient spectroscopy (DLTS) of a poly (*p*-phenylene vinylene) Schottky diode. *Synthetic metals* **111**, 273-276 (2000).

62 Heath, J. & Zabierowski, P. Capacitance Spectroscopy of Thin-Film Solar Cells. *Advanced Characterization Techniques for Thin Film Solar Cells*, 81-105 (2011).

63 Kimerling, L. Influence of deep traps on the measurement of free-carrier distributions in semiconductors by junction capacitance techniques. *Journal of applied physics* **45**, 1839-1845 (1974).

64 Feng, D. Q., Caruso, A., Losovyj, Y. B., Shulz, D. & Dowben, P. Identification of the possible defect states in poly (3-hexylthiophene) thin films. *Polymer Engineering & Science* **47**, 1359-1364 (2007).

65 Nicolai, H. *et al.* Unification of trap-limited electron transport in semiconducting polymers. *Nature Materials* **11**, 882-887 (2012).

66 Lenes, M. *et al.* Electron Trapping in Higher Adduct Fullerene-Based Solar Cells. *Advanced Functional Materials* **19**, 3002-3007 (2009).

67 Schafferhans, J., Deibel, C. & Dyakonov, V. Electronic Trap States in Methanofullerenes. *Advanced Energy Materials* **1**, 655-660 (2011).

68 Guerrero, A. *et al.* Oxygen doping-induced photogeneration loss in P3HT: PCBM solar cells. *Solar energy materials and solar cells* (2012).

69 Könenkamp, R., Priebe, G. & Pietzak, B. Carrier mobilities and influence of oxygen in C_{60} films. *Physical Review B* **60**, 11804 (1999).

70 Tapponnier, A., Biaggio, I. & Gunter, P. Ultrapure C_{60} field-effect transistors and the effects of oxygen exposure. *Applied Physics Letters* **86**, 112113 (2005).

71 Krebs, F. C., Nyberg, R. B. & Jørgensen, M. Influence of residual catalyst on the properties of conjugated polyphenylenevinylene materials: Palladium nanoparticles and poor electrical performance. *Chemistry of Materials* **16**, 1313-1318 (2004).

72 Troshin, P. A. *et al.* Impedance measurements as a simple tool to control the quality of conjugated polymers designed for photovoltaic applications. *Advanced Functional Materials* **20**, 4351-4357 (2010).

73 Nikiforov, M. P. *et al.* Detection and role of trace impurities in high-performance organic solar cells. *Energy Environ. Sci.* **6**, 1513-1520 (2013).

74 Saeki, A., Tsuji, M. & Seki, S. Direct evaluation of intrinsic optoelectronic performance of organic photovoltaic cells with minimizing impurity and degradation effects. *Advanced Energy Materials* **1**, 661-669 (2011).

75 Yu, P. *et al.* Study of traps in P3HT: PCBM based organic solar cells using fractional thermally stimulated current (FTSC) technique. *Journal of Non-Crystalline Solids* (2012).

76 Nam, C.-Y., Su, D. & Black, C. T. High-Performance Air-Processed Polymer-Fullerene Bulk Heterojunction Solar Cells. *Advanced Functional Materials* **19**, 3552-3559, doi:10.1002/adfm.200900311 (2009).

77 Glatthaar, M. *et al.* Impedance spectroscopy on organic bulk-heterojunction solar cells. *physica status solidi (a)* **202**, R125-R127 (2005).

78 Garcia-Belmonte, G. *et al.* Charge carrier mobility and lifetime of organic bulk heterojunctions analyzed by impedance spectroscopy. *Organic Electronics* **9**, 847-851 (2008).

79 Boix, P. P., Ajuria, J., Etxebarria, I., Pacios, R. & Garcia-Belmonte, G. Kinetics of occupancy of defect states in poly (3-hexylthiophene): fullerene solar cells. *Thin Solid Films* (2011).

80 Dyakonov, V. *et al.* Electrical admittance studies of polymer photovoltaic cells. *Synthetic metals* **124**, 103-105 (2001).

81 Dyakonov, V. *et al.* in *MATERIALS RESEARCH SOCIETY SYMPOSIUM PROCEEDINGS.* 235-246 (Cambridge Univ Press).

82 Deibel, C. & Wagenpfahl, A. Comment on "Interface state recombination in organic solar cells". *Physical Review B* **82**, 207301 (2010).

83 Street, R. Reply to "Comment on 'Interface state recombination in organic solar cells'". *Physical Review B* **82**, 207302 (2010).

84 Mandoc, M. M., Veurman, W., Koster, L. J. A., de Boer, B. & Blom, P. W. Origin of the reduced fill factor and photocurrent in MDMO-PPV: PCNEPV all-polymer solar cells. *Advanced Functional Materials* **17**, 2167-2173 (2007).

85 McNeill, C. R. & Greenham, N. C. Charge transport dynamics of polymer solar cells under operating conditions: Influence of trap filling. *Applied Physics Letters* **93**, 203310 (2008).

86 Ecker, B. *et al.* Degradation effects related to the hole transport layer in organic solar cells. *Advanced Functional Materials* **21**, 2705-2711 (2011).

87 Bisquert, J. *et al.* Band unpinning and photovoltaic model for P3HT: PCBM organic bulk heterojunctions under illumination. *Chemical physics letters* **465**, 57-62 (2008).

88 Gupta, S. K. *et al.* Degradation of organic photovoltaic devices: a review. (2012).

89 Sharma, A., Kumar, P., Singh, B., Chaudhuri, S. R. & Ghosh, S. Capacitance-voltage characteristics of organic Schottky diode with and without deep traps. *Applied Physics Letters* **99**, 023301 (2011).

90 Nolasco, J. *et al.* Relation between the barrier interface and the built-in potential in pentacene/C solar cell. *Applied Physics Letters* **97**, 013305 (2010).

91 Yang, B. *et al.* Solution-Processed Fullerene-Based Organic Schottky Junction Devices for Large-Open-Circuit-Voltage Organic Solar Cells. *Advanced Materials* (2012).

92 Walter, T., Herberholz, R., Muller, C. & Schock, H. Determination of defect distributions from admittance measurements and application to Cu (In, Ga) Se2 based heterojunctions. *Journal of applied physics* **80**, 4411-4420 (1996).

93 Cohen, J. D. & Lang, D. V. Calculation of the dynamic response of Schottky barriers with a continuous distribution of gap states. *Physical Review B* **25**, 5321 (1982).

94 Reis, F. *et al.* Application of abrupt cut-off models in the analysis of the capacitance spectra of conjugated polymer devices. *Applied Physics A: Materials Science & Processing* **96**, 909-914 (2009).

95 Ray, D. & Narasimhan, K. Measurement of deep states in hole doped organic semiconductors. *Journal of applied physics* **103**, 093711-093711-093716 (2008).

96 Mencaraglia, D., Ould Saad, S. & Djebbour, Z. Admittance spectroscopy for non-crystalline thin film devices characterization: comparison of Cu (In, Ga) Se2 and a-Si: H cases. *Thin Solid Films* **431**, 135-142 (2003).

97 Mingebach, M., Deibel, C. & Dyakonov, V. Built-in potential and validity of the Mott-Schottky analysis in organic bulk heterojunction solar cells. *Physical Review B* **84**, 153201 (2011).

98 Kirchartz, T. *et al.* Sensitivity of the Mott–Schottky Analysis in Organic Solar Cells. *Journal of Physical Chemistry C* **116**, 7672 (2012).

99 Garcia-Belmonte, G., Boix, P. P., Bisquert, J., Sessolo, M. & Bolink, H. J. Simultaneous determination of carrier lifetime and electron density-of-states in P3HT: PCBM organic solar cells under illumination by impedance spectroscopy. *Solar energy materials and solar cells* **94**, 366-375 (2010).

100 Kadashchuk, A., Schmechel, R., Von Seggern, H., Scherf, U. & Vakhnin, A. Charge-carrier trapping in polyfluorene-type conjugated polymers. *Journal of applied physics* **98**, 024101-024109 (2005).

101 Graupner, W., Leditzky, G., Leising, G. & Scherf, U. Shallow and deep traps in conjugated polymers of high intrachain order. *Physical Review B* **54**, 7610 (1996).

102 Fang, Z., Shan, L., Schlesinger, T. & Milnes, A. Study of defects in LEC-grown undoped SI-GaAs by thermally stimulated current spectroscopy. *Materials Science and Engineering: B* **5**, 397-408 (1990).

103 Steiger, J., Schmechel, R. & Von Seggern, H. Energetic trap distributions in organic semiconductors. *Synthetic metals* **129**, 1-7 (2002).

104 Von Malm, N., Schmechel, R. & Von Seggern, H. Distribution of occupied states in doped organic hole transport materials. *Synthetic metals* **126**, 87-95 (2002).

105 Arkhipov, V., Heremans, P., Emelianova, E. & Adriaenssens, G. Space-charge-limited currents in materials with Gaussian energy distributions of localized states. *Applied Physics Letters* **79**, 4154-4156 (2001).

106 Hwang, W. & Kao, K. A unified approach to the theory of current injection in solids with traps uniformly and non-uniformly distributed in space and in energy, and size effects in anthracene films. *Solid-State Electronics* **15**, 523-529 (1972).

107 Mark, P. & Helfrich, W. Space-Charge-Limited Currents in Organic Crystals. *Journal of applied physics* **33**, 205-215 (1962).

108 Hwang, W. Studies of the theory of single and double injections in solids with a Gaussian trap distribution. *Solid State Electronics* **19**, 1045-1047 (1976).

109 Nicolai, H., Mandoc, M. & Blom, P. Electron traps in semiconducting polymers: Exponential versus Gaussian trap distribution. *Physical Review B* **83**, 195204 (2011).

110 Hegedus, S. S. & Shafarman, W. N. Thin-film solar cells: device measurements and analysis. *Progress in Photovoltaics: Research and Applications* **12**, 155-176 (2004).

111 Hegedus, S. S. & Fagen, E. Midgap states in a-Si:H and a-SiGe:H pin solar cells and Schottky junctions by capacitance techniques. *Journal of applied physics* **71**, 5941-5951 (1992).

112 Lang, D. Deep-level transient spectroscopy: A new method to characterize traps in semiconductors. *Journal of applied physics* **45**, 3023-3032 (1974).

113 Lang, D. V., Cohen, J. D. & Harbison, J. P. Measurement of the density of gap states in hydrogenated amorphous silicon by space charge spectroscopy. *Physical Review B* **25**, 5285 (1982).

114 Carr, J. A. & Chaudhary, S. On accurate capacitance characterization of organic photovoltaic cells. *Applied Physics Letters* **100**, 213902-213904 (2012).

115 Guvenc, A. B., Yengel, E., Wang, G., Ozkan, C. S. & Ozkan, M. Effect of incident light power on Schottky barriers and IV characteristics of organic bulk heterojunction photodiodes. *Applied Physics Letters* **96**, 143301-143301-143303 (2010).

116 Lungenschmied, C. *et al.* Real-time in-situ observation of morphological changes in organic bulk-heterojunction solar cells by means of capacitance measurements. *Journal of applied physics* **109**, 044503-044503-044505 (2011).

117 Yang, K. J. & Hu, C. MOS capacitance measurements for high-leakage thin dielectrics. *Electron Devices, IEEE Transactions on* **46**, 1500-1501 (1999).

118 Deen, M. J. *et al.* Electrical characterization of polymer-based FETs fabricated by spin-coating poly (3-alkylthiophene) s. *Electron Devices, IEEE Transactions on* **51**, 1892-1901 (2004).

119 Technologies, A. *Agilent Impedance Measurement Handbook*.

120 Hegedus, S. S. & Shafarman, W. N. Thin-film solar cells: device measurements and analysis. *Progress in Photovoltaics: Research and Applications* **12**, 155-176 (2004).

121 Jarosz, G. On doubts about Mott-Schottky plot of organic planar heterojunction in photovoltaic cell. *Journal of Non-Crystalline Solids* **354**, 4338-4340 (2008).

122 Carr, J. A. & Chaudhary, S. On the identification of deeper defect levels in organic photovoltaic devices. *Journal of applied physics* **114**, 064509-064509-064507 (2013).

123 Glatthaar, M. *et al.* Impedance spectroscopy on organic bulk-heterojunction solar cells. *physica status solidi (a)* **202**, R125-R127 (2005).

124 Würfel, P. & Würfel, U. *Physics of solar cells*. (Wiley Online Library, 2005).

125 Campoy-Quiles, M. *et al.* Morphology evolution via self-organization and lateral and vertical diffusion in polymer:fullerene solar cell blends. *Nat Mater* **7**, 158-164 (2008).

126 MacKenzie, R. C. I., Shuttle, C. G., Chabinyc, M. L. & Nelson, J. Extracting Microscopic Device Parameters from Transient Photocurrent Measurements of P3HT: PCBM Solar Cells. *Advanced Energy Materials* (2012).

127 Tanase, C., Meijer, E., Blom, P. & De Leeuw, D. Unification of the hole transport in polymeric field-effect transistors and light-emitting diodes. *Physical Review Letters* **91**, 216601 (2003).

128 Nolasco, J. *et al.* Extraction of poly (3-hexylthiophene)(P3HT) properties from dark current voltage characteristics in a P3HT/n-crystalline-silicon solar cell. *Journal of applied physics* **107**, 044505-044505-044504 (2010).

129 Harada, K. *et al.* Organic homojunction diodes with a high built-in potential: Interpretation of the current-voltage characteristics by a generalized einstein relation. *Physical Review Letters* **94**, 36601 (2005).

130 Nguyen, T. P. Defects in organic electronic devices. *physica status solidi (a)* **205**, 162-166, doi:10.1002/pssa.200776805 (2008).

131 Kumar, V., Jain, S., Kapoor, A., Poortmans, J. & Mertens, R. Trap density in conducting organic semiconductors determined from temperature dependence of J− V characteristics. *Journal of applied physics* **94**, 1283 (2003).

132 Kao, K. C. *Dielectric phenomena in solids*. (Academic Press, 2004).

133 Holmes, R. J., Brütting, W. & Adachi, C. *Physics of Organic Semiconductors*. (Wiley-VCH, 2012).

134 Torricelli, F., Kovács-Vajna, Z. M. & Colalongo, L. The role of the density of states on the hole mobility of disordered organic semiconductors. *Organic Electronics* **10**, 1037-1040 (2009).

135 Godet, C. Physics of bandtail hopping in disordered carbons. *Diamond and related materials* **12**, 159-165 (2003).

136 Martens, H., Blom, P. & Schoo, H. Comparative study of hole transport in poly (p-phenylene vinylene) derivatives. *Physical Review B* **61**, 7489 (2000).

137 Schmechel, R. Hopping transport in doped organic semiconductors: A theoretical approach and its application to p-doped zinc-phthalocyanine. *Journal of applied physics* **93**, 4653-4660 (2003).

138 Braun, C. L. Electric field assisted dissociation of charge transfer states as a mechanism of photocarrier production. *The Journal of chemical physics* **80**, 4157-4161 (1984).

139 Wojcik, M. & Tachiya, M. Accuracies of the empirical theories of the escape probability based on Eigen model and Braun model compared with the exact extension of Onsager theory. *The Journal of chemical physics* **130**, 104107 (2009).

140 Craciun, N., Wildeman, J. & Blom, P. Universal Arrhenius temperature activated charge transport in diodes from disordered organic semiconductors. *Physical Review Letters* **100**, 56601 (2008).

141 Okachi, T., Nagase, T., Kobayashi, T. & Naito, H. Determination of localized-state distributions in organic light-emitting diodes by impedance spectroscopy. *Applied Physics Letters* **94**, 043301-043301-043303 (2009).

142 Nadazdy, V. *et al.* Experimental observation of oxygen-related defect state in pentacene thin films. *Applied Physics Letters* **90**, 092112-092112-092113 (2007).

143 Gomes, H. *et al.* Bias-induced threshold voltages shifts in thin-film organic transistors. *Applied Physics Letters* **84**, 3184-3186 (2004).

144 Gu, Q., Wang, Q., Schiff, E. A., Li, Y. M. & Malone, C. T. Hole drift mobility measurements in amorphous silicon-carbon alloys. *Journal of applied physics* **76**, 2310-2315 (1994).

145 Tiedje, T., Cebulka, J., Morel, D. & Abeles, B. Evidence for exponential band tails in amorphous silicon hydride. *Physical Review Letters* **46**, 1425-1428 (1981).

146 Schiff, E. Trap-controlled dispersive transport and exponential band tails in amorphous silicon. *Physical Review B* **24**, 6189-6192 (1981).

147 Yassar, A., Miozzo, L., Gironda, R. & Horowitz, G. Rod-coil and All-Conjugated Block Copolymers for photovoltaic applications. *Progress in Polymer Science* (2012).

148 Mattis, B. A., Chang, P. C. & Subramanian, V. Performance recovery and optimization of poly (3-hexylthiophene) transistors by thermal cycling. *Synthetic metals* **156**, 1241-1248 (2006).

149 Nielsen, K. T., Bechgaard, K. & Krebs, F. C. Removal of palladium nanoparticles from polymer materials. *Macromolecules* **38**, 658-659 (2005).

150 Nielsen, K. T., Bechgaard, K. & Krebs, F. C. Effective removal and quantitative analysis of Pd, Cu, Ni, and Pt catalysts from small-molecule products. *Synthesis* **2006**, 1639-1644 (2006).

151 Anthony, J. E., Heeney, M. & Ong, B. S. Synthetic Aspects. *MRS bulletin* **33** (2008).

152 Carsten, B., He, F., Son, H. J., Xu, T. & Yu, L. Stille polycondensation for synthesis of functional materials. *Chemical Reviews* **111**, 1493-1528 (2011).

153 Olthof, S. *et al.* Ultralow Doping in Organic Semiconductors: Evidence of Trap Filling. *Physical Review Letters* **109**, 176601 (2012).

154 Zhang, Y., de Boer, B. & Blom, P. W. M. Trap-free electron transport in poly (p-phenylene vinylene) by deactivation of traps with n-type doping. *Physical Review B* **81**, 085201 (2010).

155 Menke, T., Ray, D., Meiss, J., Leo, K. & Riede, M. In-situ conductivity and Seebeck measurements of highly efficient n-dopants in fullerene C60. *Applied Physics Letters* **100**, 093304-093304-093304 (2012).

156 Li, F. *et al.* Acridine orange base as a dopant for thin films. *Journal of applied physics* **100**, 023716-023716-023719 (2006).

157 Boix, P. P. *et al.* Role of ZnO Electron-Selective Layers in Regular and Inverted Bulk Heterojunction Solar Cells. *J. Phys. Chem. Lett* **2**, 407-411 (2011).